IMPACTS OF URBAN LAND USE AND TOPOGRAPHY ON LAND SURFACE TEMPERATURE AND PUBLIC HEALTH IN OUAGADOUGOU AND BOBO-DIOULASSO, BURKINA FASO

BY

OUEDRAOGO, Valentin
PhD/SPS/FT/2019/11123

WEST AFRICAN SCIENCE SERVICE CENTRE ON CLIMATE CHANGE AND ADAPTED LAND USE (WASCAL)
FEDERAL UNIVERSITY OF TECHNOLOGY, MINNA

MARCH, 2024

IMPACTS OF URBAN LAND USE AND TOPOGRAPHY ON LAND SURFACE TEMPERATURE AND PUBLIC HEALTH IN OUAGADOUGOU AND BOBO-DIOULASSO, BURKINA FASO

BY

OUEDRAOGO, Valentin
PhD/SPS/FT/2019/11123

A THESIS SUBMITTED TO THE POSTGRADUATE SCHOOL FEDERAL UNIVERSITY OF TECHNOLOGY, MINNA, NIGERIA IN PARTIAL FULFILMENT OF THE REQUIREMENTS FOR THE AWARD OF THE DEGREE OF DOCTOR OF PHILOSOPHY (PHD) IN CLIMATE CHANGE AND HUMAN HABITAT

MARCH, 2024

DECLARATION

I hereby declare that this thesis titled: "***Impacts of Urban Land Use and Topography on Land Surface Temperature and Public Health in Ouagadougou and Bobo-Dioulasso, Burkina Faso***" is a collection of my original research work and has not been presented for any other qualification anywhere. Information from other sources (published or unpublished) have been duly acknowledged.

\-----------------------------------
OUEDRAOGO, Valentin   Signature/Date
Registration number: PhD/SPS/FT/2019/11123
Federal University of Technology
Minna, Niger State

CERTIFICATION

The thesis titled: “**Impacts of Urban Land Use and Topography on Land Surface Temperature and Public Health in Ouagadougou and Bobo-Dioulasso, Burkina Faso**” by: OUEDRAOGO, Valentin (Registration number: PhD/SPS/FT/2019/11123) meets the regulations governing the award of the degree of PhD of the Federal University of Technology, Minna and it is approved for its contribution to scientific knowledge and library presentation.

Prof. J. J. Dukiya ------------------------------
Major Supervisor Signature & Date

Dr. K. O. Hackman ------------------------------
Co-Supervisor Signature & Date

Michael Thiel
Dr. M. Thiel ------------------------------
Co-Supervisor Signature & Date

Prof. A. A. Okhimamhe ------------------------------
Director of WASCAL, Doctoral Research Signature & Date
Programme in Climate Change and Human Habitat

Engr. Prof. O. K. Abubakre ------------------------------
Dean of Postgraduate School Signature & Date

DEDICATION

This thesis is dedicated to:

My wife.

My parents.

ACKNOWLEDGMENTS

First of all, I would like to give thanks to God for His protection, mercies and the graces of thoughts and perseverance throughout the duration of the programme.

My sincere thanks to the West African Science Service Centre on Climate Change and Adapted Land Use (WASCAL) for offering me a scholarship to pursue my PhD dream through the Doctoral Research Programme on Climate Change and Human Habitat, funded by the German Federal Ministry of Education and Research (BMBF) and hosted by the Federal University of Technology, Minna (FUTMINNA), Niger State, Nigeria.

I am extremely grateful to my academic supervisors, Prof. J. J. Dukiya, Dr. K. O. Hackman, and Dr. M. Thiel whose guidance, suggestions, and comments significantly helped to complete this PhD thesis. My special thanks to Dr. M. THIEL and all his colleagues at the Department of Remote Sensing, University of Würzburg whose warm reception, collaboration and support made my scientific visit in Germany fruitful. I am highly appreciative to Dr. K. O. Hackman who supported and guided me during the data collection and processing, through the initiation in the use of Google earth Engine. I am grateful to Dr. D. Anaafo at WASCAL Competence Centre for proofreading my thesis.

The acknowledgement would be incomplete without the special mention of Prof. A. A. Okhimamhe, the current and founding Director of the WASCAL graduate school programme in Minna for her relentless effort to ensure that I complete my research on time. My gratitude to all the staff, the advisory board members, and the lecturers for all kinds of support and encouragement that were extended to me during my studies.

My thanks to Prof. K. Ogunjobi, Director of Research at WASCAL Competence Centre, Ouagadougou, and all the staff for their support during my data collection and thesis write-up period.

Finally, I am grateful to my family and especially to my wife, for supporting me in prayers, and words encouragement, whenever I found the going tough.

ABSTRACT

Land Use/Land Cover (LULC) changes induced by urbanisation constitute a key driver in surface thermal properties modification, which intensifies Land Surface Temperature (LST) in rapidly urbanising areas. The aim of this research was to analyse the patterns of urban LULC changes induced LST and its public health implications in Ouagadougou and Bobo-Dioulasso, Burkina Faso. For this purpose, Landsat images were used to map LULC for four selected years including 2003, 2009, 2015 and 2021, using Random Forest, Support Vector Machine and Gradient Tree Boost algorithms in the Google Earth Engine (GEE) environment. MODIS/Aqua LST and ERA5-Land average air temperature datasets with Mann Kendall trend test were used to assess the LST and air temperature trends respectively. Aggregation was used in combination with correlation to establish the link between LULC and LST at the pixel level. Also, correlation analysis was employed to determine the relationship between LST and air temperature, and between LST and selected public diseases. Markov chain and Multiple linear regression models were employed to predict future LULC and LST. The study revealed that Ouagadougou experienced more rapid changes in LULC than Bobo-Dioulasso, with a maximum annual change intensity of 3.61 percent recorded between 2015 and 2021 as against 2.22 per cent in Bobo-Dioulasso for the period 2009 – 2015. The transition of changes was towards built-up areas, which gains targeted bare land and agricultural lands in both cities. This situation has led to the increase of built-up surface in Ouagadougou by 78.12 per cent, while 42.24 per cent of the agricultural land area was lost. However, in Bobo-Dioulasso, the built-up area has increased far more by 140.67 percent and the agricultural land areas experienced a gain of 1.38 per cent compared with the 2003 baseline. Both cities experienced an increasing trend in LST and air temperature (z value >0) with a greater increase in Ouagadougou than Bobo-Dioulasso, due to urbanisation. The global yearly trend was supported by the March-April-May (MAM) season, which shows a statistically significant trend in Ouagadougou (p-value=0.009). The LST and air temperature exhibited a stronger correlation in Bobo-Dioulasso (R=0.83) than in Ouagadougou (R=0.76). In the study area, at the pixel level, the built-up proportion showed a moderate positive correlation with the LST (0.44≤R≤0.64 in Ouagadougou, 0.49≤R≤0.61 in Bobo-Dioulasso), while the non-built-up proportion was negatively correlated with LST (-0.41≤R≤-0.6 in Ouagadougou, -0.49≤R≤-0.59 in Bobo-Dioulasso). The difference in LST between a fully built-up pixel and a fully non-built-up pixel decreased from 2003 to 2021 in both cities indicating that the LST increased in all LULC types throughout the study period. The contribution of the non-built-up class to urban cooling was lower in Bobo-Dioulasso (between 0.29°C and 1.39°C) than in Ouagadougou (between 0.74°C and 1.94°C). The research also found that malaria and dengue fever had a weak correlation with LST (R<0.4), while meningitis presented a moderate correlation in the districts of Dafra (R=0.56) and Konsa (R=0.49) in Bobo-Dioulasso) and Sig-Noghin (R=0.66) in Ouagadougou. Only the district of Do in Bobo-Dioulasso showed a strong correlation (R=0.86) with the LST. With projected increases in LST under the Business-as-usual scenario, the prevalence of temperature-related diseases may increase. In summary, the study area experienced an increase in human footprint, which contributed to the intensification of the LST which is an environmental threat to urban dwellers. These findings constitute a useful decision support for sustainable urban planning. It is therefore recommended that afforestation should be vigorously pursued at all governmental levels to step down the LST in the two cities. While sponsored research should be carried out to deepen the knowledge on LST and epidemic in the nation.

TABLE OF CONTENTS

LIST OF TABLES

LIST OF FIGURES

ABBREVIATIONS

ACF	Auto-Correlation Function
AGW	Anthropogenic Global Warming
ANAM	Agence National de la Météorologie
ASTER	Advanced Spaceborne Thermal Emission and Reflection Radiometer
BNDT	Base Nationale de Données Topographiques
CA	Cellular Automata
CBD	Central Business District
CC&HH	Climate Change and Human Habitat
CLUE	Conversion of Land Use and its Effect
DBI	Dry Built-up Index
DBSI	Dry Bare-soil Index
DRP	Doctoral Research Programme
ECMWF	European Centre for Medium-Range Weather Forecasts
ECV	Essential Climate Variable
EPA	United State Environmental Protection Agency
ERA5	European Centre for Medium-Range Weather Forecasts Reanalysis version 5
ETM+	Enhanced Thematic Mapper Plus
FAO	Food and Agricultural Organization
GDEM	Global Digital Elevation Model
GEE	Google Earth Engine
GHG	Greenhouse Gas
GIS	Geographical Information System
GMTED	Global Multi-resolution Terrain Elevation Data
GTB	Gradient Tree Boost

INSD	Institut National de la Statistique et de la Démographie
IPCC	Inter-Governmental Panel on Climate Change
ITCZ	Inter-Tropical Convergence Zone
LaSRC	Landsat Surface Reflectance Code
LCM	Land Change Modeler
LEDAPS	Landsat Ecosystem Disturbance Adaptative Processing System
LST	Land Surface Temperature
LULC	Land Use/Land Cover
MC	Markov Chain
MLP	Multi-Layer-Perceptron
MLR	Multiple Linear Regression
MODIS	Moderate Resolution Imaging Spectroradiometer
NDBI	Normalized Difference Built-up Index
NDVI	Normalized Difference Vegetation Index
NDWI	Normalized Difference Water Index
NIR	Near-Infrared
NN	Neural Network
NOAA	National Oceanic and Atmospheric Administration
OLI	Operational Land Imager
PCA	Principal Component Analysis
PNDES	Plan National de Développement Economique et Social
QA	Quality Assessment
SAVI	Soil Adjusted Vegetation Index
SDG	Sustainable Development Goal
SLC	Scan Line Corrector

SRTM	Shuttle Radar Topographic Mission Digital Elevation Model
SVM	Support Vector Machine
SWIR	Short Wave-Infra-Red
TIRS	Thermal Infra-Red Sensor
TM	Thematic Mapper
TOA	Top of Atmosphere
UHI	Urban Heat Island
UNEP	United Nation Environmental Programme
USGS	United States Geological Survey
VHR	Very High Resolution
VNIR	Visible Near Infrared
WASCAL	West African Science Service Centre on Climate Change and Adapted Land Use
WMO	World Meteorological Organization
WRS	Worldwide Reference System

CHAPTER ONE

1.0. INTRODUCTION

1.1. Background to the Study

Urbanisation is often characterized by changes in lifestyle, increased consumption, and fossil fuel usage, which contribute to alter the environment, increase global warming, and cause climate change (Yuen and Kumssa, 2011; Sannigrahi *et al.,* 2017). The exponential growth of urbanisation, in the context of climate change, presents significant problems to city authorities and urban managers in the planning of sustainable and prosperous cities (Fonseka *et al.,* 2019), because the demand for land is increasing together with unplanned development. Rapid urbanisation is expected to result in 6.68 billion urban dwellers by the year 2050 (Bocquier, 2005) and cities will be exposed to climate change effects, including Greenhouse Gas (GHG)-induced radiative forcing and localised effects from urbanisation such as the Urban Heat Island (McCarthy *et al.,* 2010).

The global temperature of the earth is rising due to the GHG radiative forcing and the effects of urbanisation (McCarthy *et al.,* 2010). Principally, the Land Surface Temperature (LST), defined as the temperature near or at the land surface (Ndossi and Avdan, 2016), in densely urbanised areas is generally higher. This situation is due to the absorption of incoming solar radiation which keeps the surface warmer during night-time in comparison to the surrounding areas which cool quickly after the sun sets. These areas are hotter because of materials like concrete that soak up and retain heat unlike trees, soil and other permeable surfaces. This phenomenon is known as the Surface Urban Heat Island (SUHI) effect (Estoque and Murayama, 2017). LST and its associated UHI effect are increasingly gaining scientists' attention in recent years. This is because, as an important indicator for monitoring vegetation, urban climate and changes in built-up areas

(Kayet *et al.,* 2016), these variables are closely related to the widely studied urbanisation phenomenon. Given the differences in Land Use/Land Cover (LULC) units across the urban setting and their varied thermal characteristics, LST is higher in densely built-up areas (Sannigrahi *et al.,* 2017), and lower in areas covered with vegetation and water (Fonseka *et al.,* 2019). Accordingly, since the rate of urbanisation in Africa is arguably the highest (Schug *et al.,* 2018) in the world and is projected to reach 55% of the total population by 2050 (Güneralp *et al.,* 2017), a proportional increase in surface temperature is anticipated in most African urban areas. This is especially true for cities in low-income countries such as Burkina Faso where the most rapid urbanisation is expected between now and 2050 (United Nations, 2019).

Besides the anthropogenic LULC activities, another determinant of LST change is topography. For example, terrain conditions including elevation, aspect, and slope can affect the surface temperature (Peng *et al.,* 2020). While the influence of topography on the LST varies according to the amount of downward solar radiation reaching the surface (Peng *et al.,* 2020), it can help explain the spatial variations of LST when combined with LULC (Estoque and Murayama, 2017).

Changes in LST in urban areas as determined by anthropogenic LULC changes and topographical variations are often associated with different public health issues. The urban population's exposure to the risk of temperature-related diseases is often intensified (Zhang *et al.,* 2020), due to the UHI phenomenon and climate change (Estoque *et al.,* 2020). As a result, spatial modelling and thermal remote sensing data and methods are becoming popular in environmental epidemiology and public health studies (White-newsome *et al.,* 2013). For example, geospatial technologies provide valuable resources for emergency response to planners and public health practitioners in identifying areas that are most at risk of temperature-related diseases. In this era of climate change associated with global health pandemics, there is a growing interest in the impacts of environmental conditions on public health.

Globally, the impacts of environmental conditions on LST have received varied scientific inquisition in different contexts. For instance, a study in Italy established that topographic elements and solar radiation have influence on the surface temperature of an area (Stroppiana *et al.,* 2014). In China, Jiang and Tian (2010) showed that LULC changes play a determinant role in LST trends in urban areas. In the African region, few studies on that subject have been conducted. Indeed, a research on the link between LST, UHI and temperature-related risks in Ghana showed that the risk is significantly elevated in areas where the LST is high (Stemn and Kumi-Boateng, 2020). In Burkina Faso, a study on the role of green infrastructure in LST mitigation in Bobo-Dioulasso found that vegetation has a cooling effect on the LST (Di Leo *et al.,* 2016). These studies demonstrated that LST strongly depends on the human footprint in the landscape in such a way that where the natural areas remain dominant, LST is found to be low.

Although LULC activities interact in complex ways with topography to modify the LST in urban centres (Peng *et al.,* 2020), their parallel and coupled impacts have not been much explored in Burkina Faso. Secondly, not much is known about the impacts of LST on public health in the country. Thus, this study has a dual purpose; first, to unveil the extent to which LST values observed in Ouagadougou and Bobo-Dioulasso are influenced by LULC changes and topography, and second, to ascertain the public health implications of LST in the two cities.

1.2. Statement of the Research Problem

Land Use/Land Cover (LULC) change is one of the causes of global climatic and environmental change (Faichia *et al.,* 2020), which lead to landscape degradation and affects urban land surface (Hamad *et al.,* 2018). As urban areas develop, there are changes in landscape such as replacement of open spaces and vegetation by houses, roads, and other urban infrastructure, which transform the permeable and moist surfaces into impermeable and dry ones (Kundu and Kumar, 2016). The establishment of these impervious surfaces causes the land surface temperature to rise due to their high thermal storage capacity (Mccartney and Mehta, 2020). Indeed, the impervious surfaces are water-resistant, impede evapotranspiration (Alavipanah *et al.,* 2015) and do not allow natural cooling of the environment (Liu and Zhang, 2011; Asgarian *et al.,* 2015), because these features absorb and store more of the incoming short wave radiation and later emit them leading to increasing temperature (Patra *et al.,* 2018).

The world's total urban population will reach 6.7 billion, and correspondingly about 0.6 to 1.3 million square kilometres of land will be converted into urban areas (Huang *et al.,* 2019b)**.** Although urbanisation phenomenon is a global phenomenon, the most dramatic increases in the share of urban population are in Africa and other developing countries in the global south (Cohen, 2006; Schug *et al.,* 2018; Hackman *et al.,* 2020; Stemn and Kumi-Boateng, 2020) . However, SUHI intensity (and its related extreme heat events that can be dangerous to health, even fatal), which is believed to be increasing in fast-growing cities, has received less attention.

The thermal properties of the urban surface are modified due to the LULC changes and the immediate consequence is the increase in the intensity of UHI (Sannigrahi *et al.,* 2017) because the urban canopy has become more complex with a diversity of composition, and arrangement of canopy elements including buildings and other impervious elements.

Indeed, the urban canopy energy budget is such a way that the Latent Heat Fluxes (LHF) and the albedo of the surface are reduced, while the Sensible Heat Fluxes (SHF) rise and contribute to increase the urban environment LST (Xia *et al.,* 2017).

The increase of LST, associated with the air temperature rise is the source of risk of temperature-related morbidity and mortality in the urban area, affecting mainly the children, the old people and those with existing health conditions (Mccartney and Mehta, 2020). The UHI intensifies during periods of heatwaves (Alavipanah *et al.,* 2015) and contributes to increased electricity demand for cooling and consequently increased air pollution by the emission of GHG through the fossil fuel-based electricity production (Tariq and Shu, 2020) and affect human health. The thermal comfort of individuals living in the urban zone is disturbed and they are exposed to heat-related diseases and morbidity due to the combined effects of UHI and heat waves (Alavipanah *et al.,* 2015).

In Burkina Faso, the combined effects of natural growth of population and positive net migration (INSD, 2022a) have placed the main cities of Ouagadougou and Bobo-Dioulasso in continuous urban expansion (Sory, 2013). On the demographic level, the total population has evolved, and the densities have exponentially increased in the two cities. For instance, Ouagadougou recorded the highest population density with an increase of 1.54 inhabitants per square kilometre between 2006 (2,847.9 inhabitants per square kilometre) and 2019 (4,385.5 inhabitants per square kilometre) (INSD, 2022c). In Bobo-Dioulasso, although lesser than Ouagadougou, the population density doubled between 2006 (271 inhabitants per square kilometre) and 2019 (553,5 inhabitants per square kilometre) (INSD, 2022b). This situation, in addition to the unprecedented land speculation occurring in the two cities, leads to a spatial expansion characterized by the development of informal housing and consequently the multiplication of impervious surfaces (built-up, roads, pavement) to the detriment of natural vegetation and water bodies. In Ouagadougou for instance, because of the increasing trend of informal housing in the urban fringe, rapid sprawl and leap development is taking place, resulting in significant urban restructuration processes (Hauer *et al.,* 2018). Indeed, due to the rapid evolution of anthropogenic activities, the natural areas of the cities have experienced significant degradation due to ongoing conversion for the construction of buildings, and farming activities. Within Ouagadougou for instance, only the "Bangr-Weogo" park, a few green spaces, and a small portion of the urban green belt remain vegetated areas (Soma, 2015).

This situation added to the effects of climate change considerably reduces the cooling effects of vegetation on the urban environment and consequently increases atmospheric temperature, which is dangerous to the human health (Jaiye, 2020; Zhang *et al.,* 2020). Consequently, the increasing environmental temperatures is responsible for heat cramps and exhaustion (Jaiye, 2020). The high near-surface air temperatures, which result from high LST are associated with increased mortality (particularly in children) in Burkina Faso (IPCC, 2014). Consequently, it has become important to understand how past and current urban expansion affect LST and how LST influences the geographic distribution of temperature-related diseases.

In the past decade, using optical and thermal remote sensing datasets, many studies have investigated LULC change and the relationship between the LST and the surface biophysical indices in different areas of Asia and Europe (Liu and Zhang, 2011; Kumar *et al.,* 2012; Alavipanah *et al.,* 2015; Boori *et al.,* 2015; Jain *et al.,* 2019; Ramaiah *et al.,* 2020). In Africa, particularly West Africa, only a few have used thermal remote sensing techniques to assess LST in urban areas (Ogunjobi *et al.,* 2018; Eresanya *et al.,* 2019; Stemn and Kumi-Boateng, 2020). To compute the LST, these studies focused on diachronic analyses between two, three or four periods without a clear comparative analysis between several months of the year to set the suitable period for LST assessment, as it should be done under tropical conditions. Also, even at the global level, the implication of surface temperature on public health is not well known (White-newsome *et al.,* 2013), despite the plethora of literature on LULC and LST. Thus, in Burkina Faso, very little work has been done on LULC change impacts on surface temperature (Di Leo *et al.,* 2016). However, not much work has been conducted on how the LST pattern over the study area impacts public health. Specifically, this research used time-series satellite imagery together with ancillary data and socio-economic data to determine the patterns of LULC changes induced LST in the cities of Ouagadougou and Bobo-Dioulasso, Burkina Faso and assess its impacts on public health.

1.3. Research Questions

The research attempts to answer the following questions:

i. What are the major Land Use/Land Cover changes in Ouagadougou and Bobo-Dioulasso from 2003 to 2021?

ii. What is the trend of the meteorological and satellite-based thermal emission data between 2003 and 2021 in the two cities?

iii. What is the correlation between land surface temperature and the urban Land Use/Land Cover dynamics in the two cities?

iv. To what extent is the Land surface temperature related to the distribution of temperature-related diseases in the two cities?

v. What will be the future trend of Land Use/Land Cover changes and land surface temperature in the two cities?

1.4. Aim and Objectives of the Study

This study was aimed at analysing the influence of Land Use/Land Cover changes and topography on land surface temperature and its implications on public health in the cities of Ouagadougou and Bobo-Dioulasso, Burkina Faso. This aim is in line with the Sustainable Development Goal (SDG) number 11: "Sustainable cities and communities". This is to be achieved through the following objectives:

i. assess the major Land Use/Land Cover changes in Ouagadougou and Bobo-Dioulasso between 2003 and 2021;

ii. carry out comparative trend analysis of the meteorological and satellite-based thermal emission data from 2003 to 2021 between the two cities;

iii. determine the correlation between land surface temperature and urban Land Use/Land Cover changes in the two cities;

iv. assess the relationship between temperature-related diseases and land surface temperature in the two cities; and

v. carry out future projection of Land Use/Land Cover and land surface temperature in the two cities.

1.5. Justification for the Study

Previous studies have used data from series of satellites platforms such as Landsat, Moderate Resolution Imaging Spectroradiometer (MODIS) and Advanced Spaceborne Thermal Emission and Reflection Radiometer (ASTER) coupled with observation or gridded (ground observation data combined with satellite data) air temperature datasets to derive land surface temperature. This research uses satellite data and reanalysis (ground observation data combined with model data) air temperature datasets to assess the trend in LST and its patterns regarding different LULC dynamics.

This research provides information on the trend in LULC units within the urban environment in Burkina Faso, their influence on the LST and the consequences on urban cooling. This could generate much needed data to support municipal authorities in planning for better mitigation and adaptation measures that can improve the well-being of the urban population. Burkina Faso is a Sahelian country with high urban temperatures. Thus, this study will support urban planners and decision makers by providing information on the types of LULC that increase the heat capacity of the urban surface, for a better sustainable land use policy development.

This research contributes, in the country level, to the achievement of the United Nations Sustainable Development Goals (SDG) 11 on “Sustainable cities and communities”; 13 on “Climate action”; and 15 on “Life on land”. Indeed, the implementation of sustainable land use policy including building codes policy, green spaces development, open spaces development, blue infrastructures development can play a key role in climate change adaptation and mitigation in urban areas. This could then contribute to improve the thermal comfort for a better urban liveability.

This research builds on the existing approaches to perform a time series analysis of the LST and LULC using a cloud computing platform, Google Earth Engine (GEE). The findings could be a valuable addition to the literature on applied climatology and particularly the use of GEE in LULC analysis and climatic data extraction. It could also strenghten the knowledge in terms of LULC changes impact on LST patterns in the African region. The use of a long-term dataset with a time step of one year in this study could show the annual dynamic of urban land surface temperature as well as air temperature. This could bring out a clear understanding of the spatio-temporal patterns and linkages of the two variables for further research on urban climate modelling.

1.6. Study Area Description

1.6.1. Geographical location of the study areas

The research was conducted in Ouagadougou and Bobo-Dioulasso, the first two largest cities of Burkina Faso. Ouagadougou is the political and administrative capital and is within the province of Kadiogo in the Centre Region. Bobo-Dioulasso, the economic capital of Burkina Faso, belongs to the province of Houet in the Hauts-Bassins Region. They are located between Longitude 1°41’31’’W and 1°21’05’’W and between Latitude 12°12’42’’N and 12°30’14’’N; between Longitude 4°23’40’’W and 4°12’19’’W and between Latitude 11°06’26’’N and 11°17’27’’N, respectively. Ouagadougou covers an area of 970 square kilometres while Bobo-Dioulasso’s land mass in 1,779 square kilometres.

In term of topography, Ouagadougou lies in the so-called central peneplain (lowland area) of Burkina Faso, with altitudes fluctuating between 272 and 368 metres above sea level. In Bobo-Dioulasso however, the altitudes range between 287 and 558 metres above sea level, indicating a relatively high land area compared to Ouagadougou. Figure 1.1 presents the geographical location of the study sites: (a) shows West Africa inset Burkina Faso; (b) presents Burkina Faso showing administrative boundaries of districts inset Ouagadougou and Bobo-Dioulasso in red boxes; (c) is a Zoom of Ouagadougou showing elevation, roads, rivers and localities; (d) is a Zoom of Bobo-Dioulasso showing elevation, roads, rivers and localities.

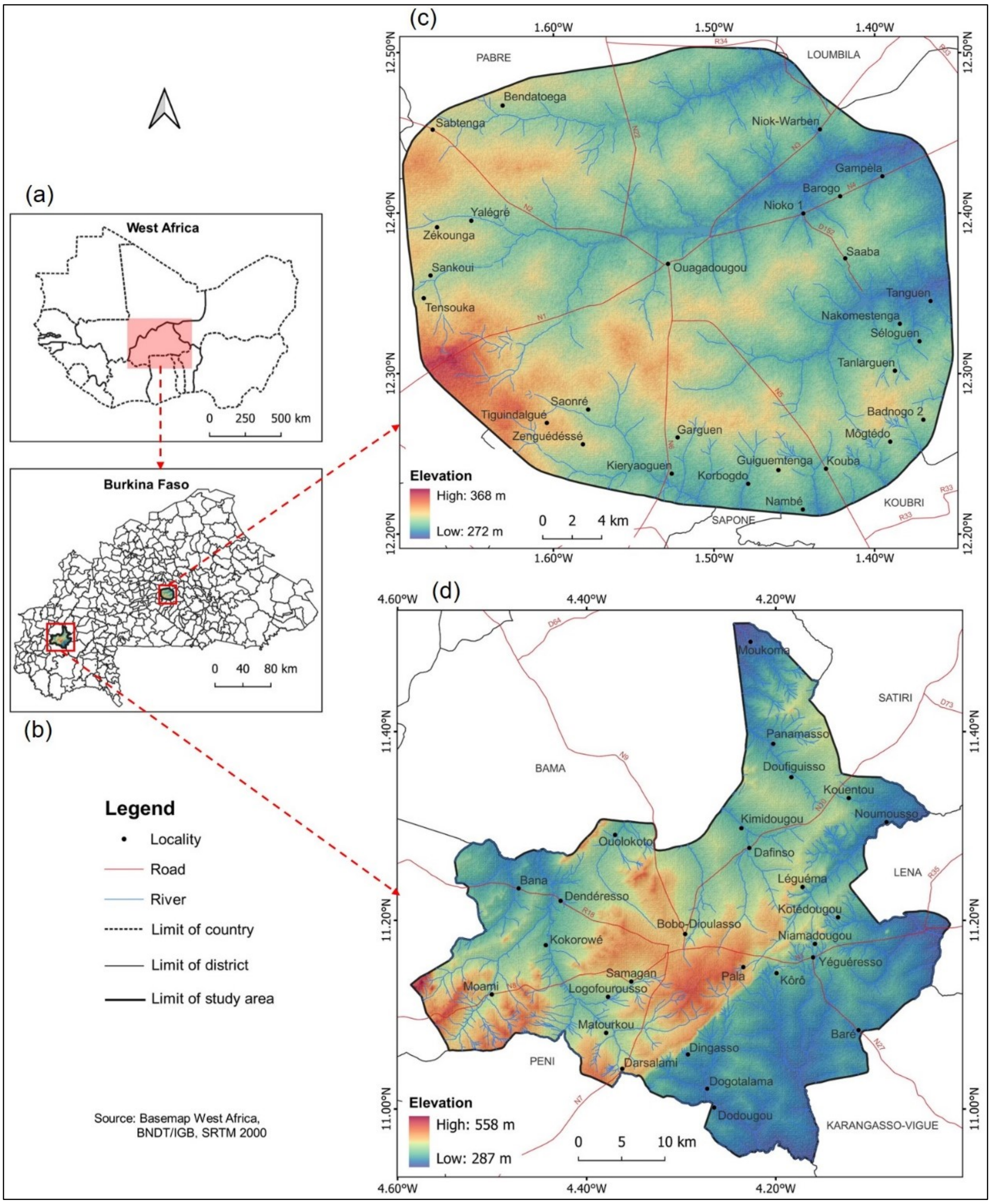

Figure 1.1: Location of the Study Area.

Source: Ouedraogo *et al.* (2023)

1.6.2. Climate

The two cities are all situated in the Sudanian climatic zone (North Sudano-Sahelian for Ouagadougou and South Sudanian for Bobo-Dioulasso). As in the whole of West Africa, the climate over the study area depends on the Inter-Tropical Convergence Zone (ITCZ) fluctuations, from south to north and vice versa (Byrne *et al.,* 2018). The climate in the study sites is characterized by high temperatures and a uni-modal rainfall pattern with a peak in August. The rain falls usually between May and October (Figure 1.2), while the dry season, relatively long, ranges from November to April. Station data received from the National Meteorological Agency (ANAM) of Burkina Faso, showed that the average annual rainfall from 1980 to 2020 was 757.94 mm and 1,027.2 mm at the station of Ouagadougou and Bobo-Dioulasso, respectively. During the same period, the total amount of yearly rainfall varied from 571.4 to 1003 mm/year in Ouagadougou, whereas, in Bobo-Dioulasso, it ranged from 681.7 to 1,370.2 mm/year. These features show that Bobo-Dioulasso received more rainfall than Ouagadougou and consequently the amount of sensible heat radiated from the surface may be relatively low.

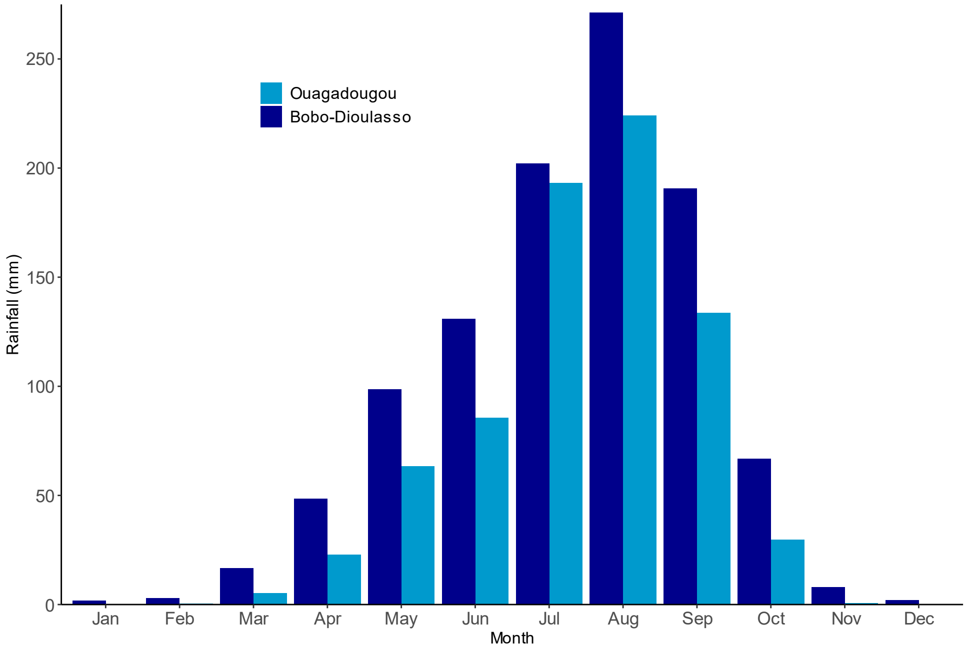

Figure 1.2: **Monthly Rainfall in Ouagadougou and Bobo-Dioulasso from 1980 to 2020**

Source: ANAM (2021)

The temperatures fluctuated during the period and varied from one site to another. The monthly average temperature varied from 25.21°C to 33.26°C in Ouagadougou and from 25.54°C to 31.05°C in Bobo-Dioulasso (Figure 1.3). In the two sites, high day time temperatures were observed in March, April and May, while low daytime temperatures were recorded in July, August and September. The night-time low temperatures were recorded between December and February due to the Harmattan winds.

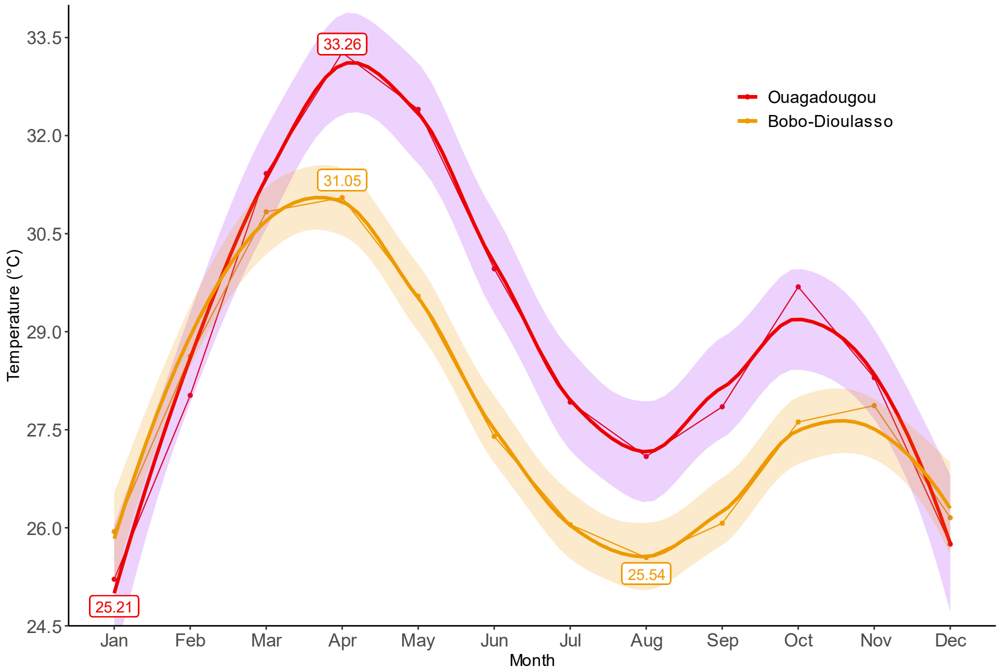

Figure 1.3: **Monthly Air Temperature in Ouagadougou and Bobo-Dioulasso, from 1980 to 2020**

Source: ANAM (2021)

1.6.3. Vegetation, drainage and soils

Ouagadougou falls in the North-Sudanian phytogeographical domain and is experiencing a significant degradation of vegetation cover due to the occupation of the space for housing purpose, farming, and the utilisation of biomass as a source of domestic energy. Only the protected forests of *Bangr-Weogo*, of the National Scientific and Technologic Research Centre, and a few green spaces scattered along the roads and houses form the vegetation of the city. The tree species common to the study area include *Vitellaria* *paradoxa*, *Lannea microcarpa, Mangifera indica, Khaya senegalensis*, *Acacia nilotica*, *Parkia biglobosa, Adansonia digitata, Faidherbia albida, Carapa procera.*

In terms of drainage, the settlement of Ouagadougou is set up in the *Massili* catchment. Given such geographic location, the city is drained by four main tributaries of the river *Massili* that flows from south to north. They are the central watercourse, the watercourse of *Zogona*, the watercourse of *Mogho Naaba* and the watercourse of *Wemtenga*. In the framework of urban development, these watercourses have been planned to facilitate the evacuation of runoff water during rainy season and improve the management of water for urban activities. In addition, there are three main urban dams, with a total capacity of 5,235,500 cube metres (INSD, 2022c), which allow the storage of rain water in the city. Ouagadougou lies on less deep and nutrients deficient soils. There are two types of soils namely hydromorphic soils which evolve under the influence of the water from dams, and the less evolved soils, characterized by weak storage of runoff water (Soma, 2015).

Unlike Ouagadougou, Bobo-Dioulasso belongs to the south-Sudanian phytogeographical vegetation domain. The vegetation is dominated by open forests and wooded savannahs. There are some protected forests such as *Dienderesso* forest, Kua forest, Kou forest and *Kuinima* forest (INSD, 2022b). The common trees species in the area are *Antiaris Africana, Berlinia grandiflora, Carapa procera, Vitellaria paradoxa, Voacanga Africana*, *Lannea microcarpa, Khaya senegalensis*, *Acacia nilotica*, *Parkia biglobosa*, *Mangifera indica, Adansonia digitata.*

In terms of climate change, the forests are key ecosystems in Bobo-Dioulasso as they serve as a sink for the urban carbon capture and storage and contribute to cool the environment. The predominance of vegetation may lead to high evapotranspiration and then a relatively low surface temperature in the city compared to Ouagadougou. The settlement is crossed from South to North by the River *Kou*, a tributary of the *Mouhoun* River. A number of water sources are encountered in the city, with the Guinguette being the most important (INSD, 2022b). Bobo-Dioulasso comprises four types of soils: hydromorphic soils, tropical ferruginous soils (with little leaching and on sandy materials), sandy-clay soils and sandy soils.

1.6.4. Population and economic characteristics of the study area

The population of Ouagadougou city has evolved from 60,000 inhabitants in 1960 to 172.661 inhabitants in 1975, 441,514 inhabitants in 1985, 709,736 inhabitants in 1996, 1,475,223 inhabitants in 2006 (INSD, 2006) and achieved 2,415,266 inhabitants (45.1% of the urbanisation rate) in 2019 (INSD, 2022a). Figure 1.4 shows a rapid growth of the population which increased by 39.25 times in 2019 compared to 1960. The main ethnical groups living in the area are the *Mossi*, *Dioula*, *Bissa* and *Gurunsi*. The economic activities are dominated by industry, commerce, services, agriculture and livestock in the fringe areas of the city.

As for Bobo-Dioulasso, its population has evolved from 50,000 inhabitants in 1960 to 115,063 inhabitants in 1975, 228,668 inhabitants in 1985, 309,771 inhabitants in 1996, 489,967 inhabitants in 2006 (INSD, 2006) to reach 984,603 inhabitants, corresponding to 16.9% of the urbanisation rate in 2019 (INSD, 2022a). Like Ouagadougou, the population figures exhibited an increasing trend in Bobo-Dioulasso. Indeed, the total population of the city increased by 18.69 times in 2019 compared to 1960, showing a lower growth than Ouagadougou (Figure 1.4). The main economic activities in Bobo-Dioulasso are services, commerce, agriculture, livestock, industry, hunting, fishing and handicraft.

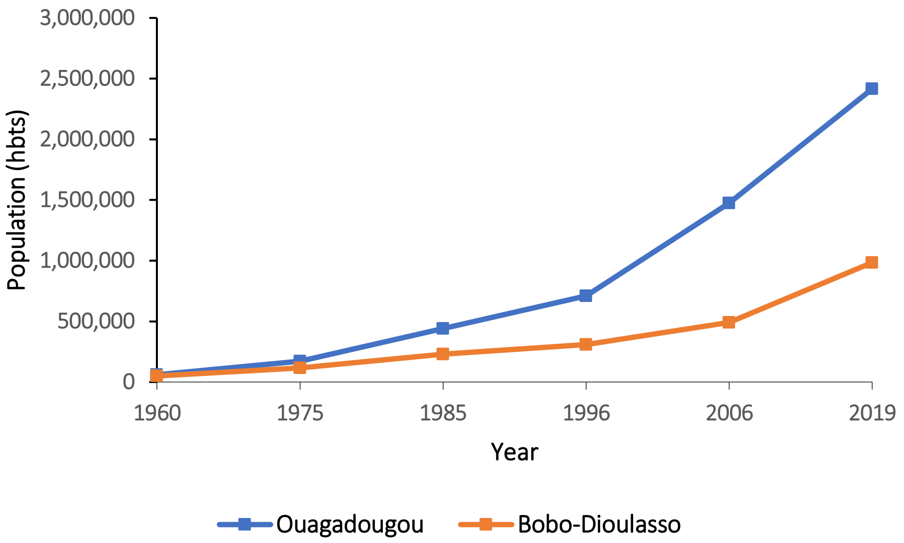

Figure 1.4: **Trend in Growth of the Urban Population in the Two Cities**

Source: INSD (2022b), INSD (2022c)

1.6.5. Urban development in the two cities

The settlement of Ouagadougou has been established as the capital of the Mossi kingdom in 1441 and as the permanent residence of the *Mogho Naba*, the king of the *Mossi*, in 1691. The settlement first developed around the royal palace, with the regrouping of certain villages that gave their names to certain current districts of the city, such as "*Gounghin*", "*Laarlé*", "*Ouidi*" (Soma, 2015). The administrative structuration of Ouagadougou has changed many times over the past few decades. In 1984, Ouagadougou was divided into five districts to facilitate the management and to improve access to public services by the citizens.

Bobo-Dioulasso city is Burkina Faso's second most populous settlement (Di Leo *et al.,* 2016) created around 1050. The area has been an administrative and military post for France and was the capital of Burkina Faso (former Upper Volta) until 1947. Bobo-Dioulasso originated from a small village called *Sya,* which was conquered by France in 1897. After the France occupation, Sya was changed into Bobo-Dioulasso, which means the house of the *Bobo* and *Dioula*. The French colonial government constructed, between

1926 and 1929, the city layout using a grid pattern structured in avenues and streets, squares and urban lots (Fourchard, 2003). This has laid the frame of the modern city centre and its LULC policies. New industries arrived in the city during 1980 and 1990s and contributed to shaping the economic sector.

Up to 2009, Ouagadougou's city comprised five districts, 30 sectors and 17 associated villages, whereas Bobo-Dioulasso had three districts and 25 sectors. In December 2009, the National Assembly adopted a new law which culminated in the division of Ouagadougou into twelve districts and 55 sectors (INSD, 2022c); and Bobo-Dioulasso into seven districts, 33 sectors with 36 affiliated villages (INSD, 2022b).

While the urban areas were spatially being restructured for close governance purposes, the authorities undertook several planning initiatives and interventions to develop formal housing for the citizens. From the colonial period to the independence and the revolution era, many formal housing units have been provided by the successive governments, but in insufficient number. For example, for a demand of 38.000 parcels in Ouagadougou, the governments provided only 10.800 parcels between 1960 and 1980. In addition to the usual housing development programmes, there were urban renewal projects such as the "project ZACA" area (an administrative and trade zone), the development of new modern housing areas such as "Ouaga 2000" (Southern part of Ouagadougou), "Bobo 2010" (Northern part of Bobo-Dioulasso), "Bassinko" (Northern part of Ouagadougou) and other private estates development in the two cities. Since 2009, housing development in the country is led by private real estates/land development companies, whose number has reached 275 in 2019 (Sory, 2019). The growth in housing development has caused the spatial expansion of the cities' areas as showed by Figure 1.5. The spatial growth of the urban area was relatively slower in Bobo-Dioulasso than in Ouagadougou.

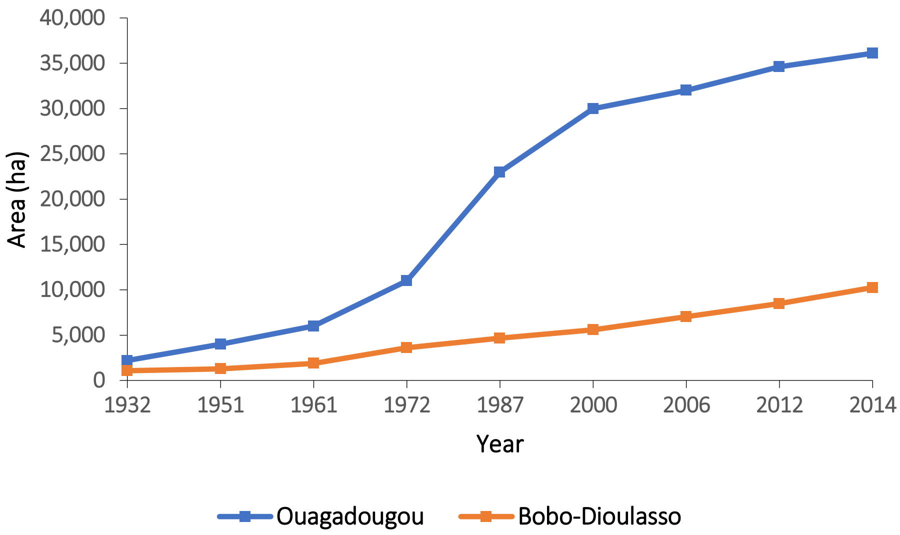

Figure 1.5: **Spatial Expansion of the Urban Area Size in the Two Cities**

Source: Soma (2015)

1.7. Scope and Limitations of the Study

1.7.1. Scope of the study

The research has a temporal scope of 19 years (2003 - 2021). This interval is selected not only because the study intends to carry out a time series analysis of LULC change and LST, but also to fit with MODIS LST data availability over the area. Although MODIS Aqua LST products were available by mid-2002, 2003 was considered as the start year to have full year data (from January to December).

The spatial scope of the study covers the metropolises of Ouagadougou and Bobo-Dioulasso. Being the main urban centres of Burkina Faso, the two cities experience rapid urbanisation, in terms of spatial expansion and population growth, which causes the development of impervious lands to the detriment of natural vegetated and water body areas. The study concerns the urban and suburban areas of the two cities for the purposes of comparison between the two zones in regard to LST trends. Moreover, the two cities are located in the same climatic zones with slightly different meteorological and environmental conditions and are therefore well suited for comparative study.

In terms of content, the study focuses on LULC changes assessment, air temperature trend assessment, LST trend assessment and LST related diseases investigation. This research wholly depends on the existing datasets captured by ground observation stations or satellites platforms such as Landsat, MODIS Aqua and also on reanalysis datasets to map the LULC changes in the two cities and determine the LST and air temperature trends and relationship during the study's chosen time span. Furthermore, it assesses the relationship between the LST and LULC changes on one hand, and between the air temperature in the other. It also investigates the link between selected temperature-related diseases and LST.

1.7.2. Limitations of the study

The limitations of this research include the non-availability of in situ measurements of LST datasets when the satellite passes to serve as control data for the accuracy assessment of the LST retrieved from MODIS Aqua satellite data. In addition, the coarse spatial resolution and the presence of missing data in MODIS daily LST, due to cloud cover, might introduce some uncertainties in the seasonal and yearly aggregated data. To mitigate these limitations, MODIS LST was considered as a proxy of the surface skin temperature over the study area, and a gap-filling method was used to compute the missing daily LST values.

More so, the data on temperature-related diseases do not cover the whole temporal and spatial span of the research. While, the datasets have been aggregated at district level, rather than patient location based. Essentially, five years (2017 - 2021) monthly reported cases covering the Central Business District (CBD) areas of the different cities were used for the analyses. The study assumed that all patients recorded in a given district live within the geographical area of that district to proceed.

CHAPTER TWO

2.0. LITERATURE REVIEW

2.1. Conceptual Framework

This sub-section describes the conceptual framework of the study. It analyses the concepts of urbanisation, temperature inversion, Land Use/Land Cover and Land Use/Land Cover change, Land Surface Temperature and Urban Heat Island.

2.1.1. Concept of urbanisation

Urbanisation is a complex socio-economic phenomenon that results in a shift of population's concentration from rural to urban settings and the consequent spatial and demographic changes occurring in the destination areas (Kuddus *et al.,* 2020). In 2018, the United Nations estimated that about 4.2 billion people were living in urban areas, and this figure will reach 6.7 billion by 2050 (United Nations, 2018). In a similar way, the global urban settings area is expected to increase by about 0.6 to 1.3 million square kilometres between 2015 and 2050 (Huang *et al.,* 2019a). The future global urban development is expected to slow down compared to that of the period 1950 – 2018. It is estimated that the urban annual growth rates will range between 1.7% and 1.3%, from 2018 to 2030 and 2030 to 2050 respectively, against 2.2% during the period 1990 - 2018 (United Nations, 2018).

In Africa, the rate of urbanisation is arguably the highest in the world (Schug *et al.,* 2018) and is projected to reach 55% of the total population by 2050 (Güneralp *et al.,* 2017). The rapid trend of urbanisation in Africa has been confirmed by several authors (Güneralp *et al.,* 2017; Schug *et al.,* 2018; Hackman *et al.,* 2020; Stemn and Kumi-Boateng, 2020) and is characterized by the increasing number of its megacities, cities and towns (Güneralp *et* *al.,* 2017). The main drivers of urban growth in Africa, in particular and the developing world in general, are the population growth (natural growth, and positive net migration), advances in medical sciences, global technological transformation and political change (Cohen, 2006), the combined effect of which is causing a spatial expansion of urban settlements towards the surrounding rural areas. The urbanisation patterns in most of the developing countries, like Burkina Faso, is inconsistent with the local plans and policies, resulting in the formation of slums where socio-economic facilities such as transportation, water and sanitation, health, and education are lacking (Rimal *et al.,* 2018).

2.1.2. Concept of temperature inversion

In the Troposphere, temperature decreases with height under normal conditions; the higher we go, the lower the temperature and the lapse rate equals to 6.5°C/km. Temperature inversion or thermal inversion, is therefore the reversal of temperature's normal behaviour in the troposphere where temperature increases with height *(*Nejad *et al.,* 2023). Under inversion condition, a layer of cool air at the surface is overlain by a layer of warm air.

It occurs in areas with clear skies, light wind, and in low places such as valleys. Inversions play a key role in cloud formation, precipitation and visibility level. An inversion acts as a blanket on the up-warding air from the layers below, and as a result, the convection produced by the heating of the air from below and diffusion of pollutants as well are limited to levels under the inversion. So, in areas with persistent low-level inversion occurs, convective clouds can not grow and visibility may be reduced due to the accumulation of dust and smoke particles. Inversion also affects daytime air temperature variations. Since daytime warming of air is mainly caused by land surface emission, if an inversion occurs in-low level, only a shallow layer of air will be heated and thus the environmental temperature will rise astronomically. A schematic representation of an inversion is shown in Figure 2.1. T_{base}: Temperature at the basis of inversion, T_{top}: Temperature at the top of the inversion, Z_{base}: Height of the base of the inversion, Z_{top}: Height of the top of the inversion, DZ_{inv}: Temperature difference across the inversion, DT_{inv}: Depth of the inversion and the temperature lapse rate within the inversion.

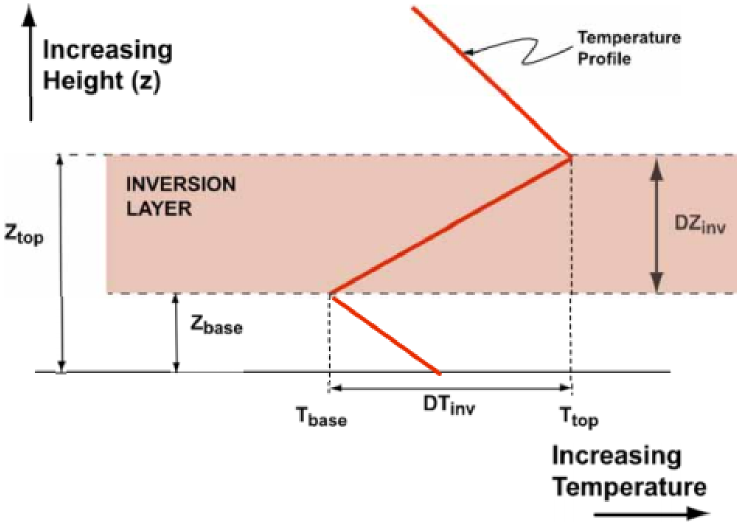

Figure 2.1: Temperature Inversion Scheme

Source : (Iacobellis *et al*., 2009)

2.1.3. Concepts of land cover, land use and land use/land cover change

Land cover is defined as the observed natural and man-made features coverings of the earth's surface (Giri, 2012). The major land cover types are forests, grassland, barren land, pavement, asphalt, water body including groundwater (Giri, 2012).

Land use, in contrast, is defined as the way the biophysical attributes of the land are manipulated and the purpose for which the land is used (Giri, 2012). In other words, it refers to how the land is used by humans. According to this author, a land covered by vegetation can be a forest as seen from the ground or through remote sensing platforms, while the same area of forest can be used for production, recreation, conservation or for religious purposes. The land cover is also defined as the type of feature present on the earth surface, while land use is related to anthropogenic activity or economic function associated with a piece of land (Congalton, 2015). Land cover data can be directly extracted from remote sensing images, whilst ancillary data is often needed to retrieve accurate land use information. According to the National Oceanic and Atmospheric Administration (NOAA), land cover data documents how much of a region is covered by forests, wetlands, impervious surfaces, agriculture, and other land and water types. Land use shows how people use the landscape whether for development, conservation, or mixed uses. The different types of land cover can then be managed and used differently.

Land Use/Land Cover (LULC) change comprises two major types: LULC modification and LULC conversion. Indeed, a conversion is a change from one LULC category to another, while a modification denotes a change in condition within the same LULC category (Giri, 2012). An example of land-cover modification is forest degradation that may be due to change in phenology, biomass, forest density or flooding. With remote sensing data, it is easier to measure and monitor conversion than modification. Modification is usually a long-term process and may require multi-year and multi-seasonal data for accuracy assessment. Land use may change without land-cover conversion or modification. However, once land use activities are practised in a particular area, land cover may change even if the land use remains unchanged; therefore, land-use is likely to cause land cover change.

In Ouagadougou as well as Bobo-Dioulasso land cover is mainly characterized by vegetation, impervious surfaces (for example built-up, roads), water body. The encountered land uses are agricultural use, economic activities use, conservation (for example protected forests, rivers), housing (for example settlement). In sum, deducing from these definitions and examples, land cover can be considered as the physical cover, whereas land use is based on the function or the socio-economic purpose for which the land is used. A piece of land can then have only one land cover (for example water body) but can have more than one land use (for example educational, conservation, tourism).

In this research, the term Land Use/Land Cover is adopted, because it is a collective term meaning that the maps generated include both land use and land cover types (Reese, 2011). Land use, being the expression of underlying anthropogenic driving forces, is the dominant source of land cover change which may have further biophysical impacts on the land surface (Meyer and Turner II, 1996). Therefore, LULC change concept is considered, because the thermal properties of the surface depend on the type of materials covering it. Though the way the population uses the land may influence the surface properties through the resulting waste from the household or the economic activities, the LULC change will result in a blacker or whiter surface which determines its reflectance capacity. The whiter the surface the higher the albedo and the lower the amount of incident radiation absorbed (Beucher, 2010).

2.1.4. Concept of land surface temperature

The Land surface temperature (LST) is a driving force in the exchange of long-wave radiation and turbulent heat flux at the interface between the surface and the atmosphere. It is considered as the radiometric temperature or skin temperature of the ground (Li *et al.,* 2013). Radiometric and thermodynamic temperature are the same for homogeneous and isothermal surfaces (Becker and Zhao-Liang Li, 1995). Since surfaces with homogeneous pixels are rare in the nature, the radiometric temperature depends on the configuration of the surface materials, their emissivity and the electromagnetic spectrum channel used to measure it.

Therefore, the LST depends on the incoming solar radiation, the albedo, the vegetation cover and the soil moisture. In most cases, it is a mixture of vegetation and other land cover types temperatures. In that case, the LST shows quick variability because all types of land cover respond rapidly and differently to incident radiation changes due to cloud cover, aerosol load modifications and daytime illumination variation.

The LST can also be defined as the surface radiometric temperature corresponding to the instantaneous field-of-view of the satellite sensor (Prata *et al.,* 1995) or, particularly as the ensemble directional radiometric surface temperature. So, according to the Indian Institute of Remote Sensing (2016), the LST is the average skin temperature of the ground under the pixel scale mixed with different fractions of surface cover. For instance, for bare soil surface, LST is the soil surface temperature, while for densely vegetated area, LST is considered as the canopy surface temperature of the vegetation.

2.1.5. Concept of urban heat island

Within the urban setting, the LST varies between the core city and the surrounding areas in such a way that the urban core areas experience higher temperatures than the periphery. This persistence of heat within the inner-city compared to the fringe areas represents the Urban heat island (UHI). The changes in thermal properties of urban materials, and their spatial distribution are the key factors of UHI patterns (Mccartney and Mehta, 2020). Urban areas are dominated by low-albedo impervious surfaces such as buildings, roads and pavements, which absorb and store incoming solar radiation during daytime and release the heat at night-time leading to high temperature in the urban core. Thus, there are two types of UHI: the Surface Urban Heat Island (SUHI) and the Atmospheric Urban Heat Island (AUHI) (Kotharkar and Surawar, 2016). The SUHI is the radiative temperature difference between impervious and natural surfaces, measured by LST, based on thermal remote sensing. Its magnitude depends on sun intensity and LULC types and characteristics (Farina, 2012). The AUHI refers to the effects of temperature difference in the canopy layer and the boundary layer. The canopy layer, being the layer of air from the surface to treetops or rooftops; the Canopy Layer Heat Island (CLHI) is measured by in situ sensors mounted on fixed meteorological stations (Badugu *et al.,* 2022). However, the boundary layer extends from treetops or rooftops to where urban landscapes no longer influence the atmosphere. The Boundary Layer Heat Island (BLHI) is measured by tall towers, radiosondes and aircraft (Badugu *et al.,* 2022).

In the present research, the term Urban Heat Islands (UHI) was used to refer to SUHI, based on LST derived from MODIS Aqua satellite products. Thus, due to the urban LULC changes, resulting in the increase of impervious surfaces to the detriment of vegetated and water body areas, the urban runoff is increased and the evapotranspiration is reduced. This situation causes an unbalanced energy budget characterized by a reduction of the Latent Heat Flux (LHF) and albedo against an increase of the Sensible Heat Fluxes (SHF) (Xia *et al.,* 2017). Indeed, the downwelling solar radiation associated with the high heat storage capacity of the urban materials increase the SHF and consequently intensify the LST and UHI. The increases in LST lead to rising air temperature over the urban environment which consequently affects the quality of life of city inhabitants by deteriorating the thermal comfort (Stemn and Kumi-Boateng, 2020) and causing temperature-related diseases.

2.2. Theoretical Framework

2.2.1. Theory of thermal radiation

The earth energy budget is determined by the energy input from solar radiation and the energy loss by terrestrial thermal radiation (Schmittner, 2018). The sun emits radiation over a wide range of wavelengths forming the electromagnetic spectrum, which range from gamma rays with wavelengths of 3.10^{-3} nanometres (shorter wavelength and higher energy) to radio waves with wavelengths of 300 meters (longer wavelength and lower energy). Different portions of the electromagnetic spectrum are of diverse relevance to earth observation.

Human eyes are sensitive to the visible light that occupies a small part of the spectrum; from 390 nanometres to about 750 nanometres (Figure 2.2). Indeed, electromagnetic radiations are electric and magnetic waves that can travel through a vacuum and matter at the speed of light. The interaction between electromagnetic radiation and matter depends on the wavelength of the radiation. The molecules have different discrete energy states and they can transit from one state to another one by absorbing or emitting a photon at a wavelength that corresponds to that energy difference (Schmittner, 2018). Absorption of a photon leads to a transition from a lower to a higher energy state, while emission of a photon indicates a transition from a higher to a lower state.

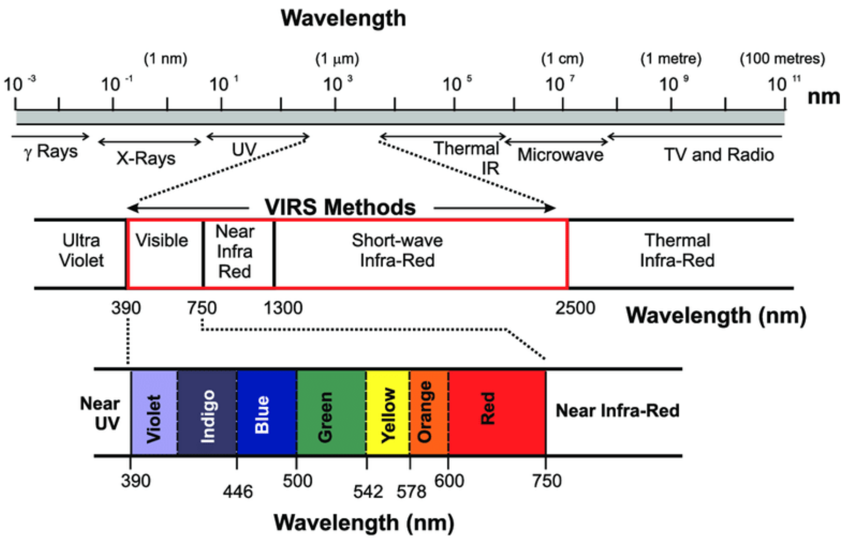

Figure 2.2.: **Electromagnetic Spectrum**

Source: Sparkes *et al.* (2011)

The power of solar radiation reaching the top of the atmosphere is 1,370 w/m^2 and is known as the solar constant, but only 338 W/m^2 (25 per cent) reaches the earth's surface. The sun's radiative flux is maximum at a wavelength of 0.5 µm, at the centre of the visible part of the spectrum (Figure 2.2). Solar radiation, by warming up the earth, is the driver for many chemicals, physical and biological phenomena in the atmosphere, on the ground and in the oceans. The thermal remote sensing is based on the theory that all objects with a temperature above zero kelvin (-273.15°C) emit radiation in all direction as electromagnetic waves and the amount of radiated energy and the wavelengths depend on the emissivity (ε) of the surface and its kinetic temperature (Prakash, 2000). Electromagnetic radiation is governed by the physical laws of radiative transfer, comprising Planck's law, Stephan-Boltzmann law and Wien's displacement law.

2.2.1.1. *Planck's law of radiation*

The Physicist Max Planck determined experimentally the relationship between the radiative energy flux from a black body and its absolute temperature. He derived then Planck's function describing the radiance emitted by a black body as presented in Equation (2.1).

$$B(\lambda, T) = \frac{C_1}{\lambda^5\,[\exp\left(\frac{C_2}{\lambda T}\right) - 1]} \tag{2.1}$$

Where $B(\lambda, T)$ corresponds to the spectral radiance in (W/m^2), T stands for the absolute temperature in Kelvin (K), λ is the wavelength in metres (m), ε is the emissivity, C_1 is the first radiation constant (1.191 × 10-16 W/m^2), and C_2 the second radiation constant (1.439 × 10-2 m K). However, most natural objects are non-black bodies and the spectral emissivity ε is determined by the ratio between the radiance emitted by an object at wavelength λ and that emitted by a black body at the same temperature (Dash *et al.,* 2002). For a non-black body ($0 < \varepsilon < 1$), Planck's function is multiplied by ε, as shown in Equation (2.2).

$$B(\lambda, T) = \frac{\varepsilon C_1}{\lambda^5\,[\exp\left(\frac{C_2}{\lambda T}\right) - 1]} \tag{2.2}$$

Therefore, the amount of radiated energy depends on the wavelength and the temperature. The hotter the object, the shorter the wavelength and vice versa (Figure 2.3).

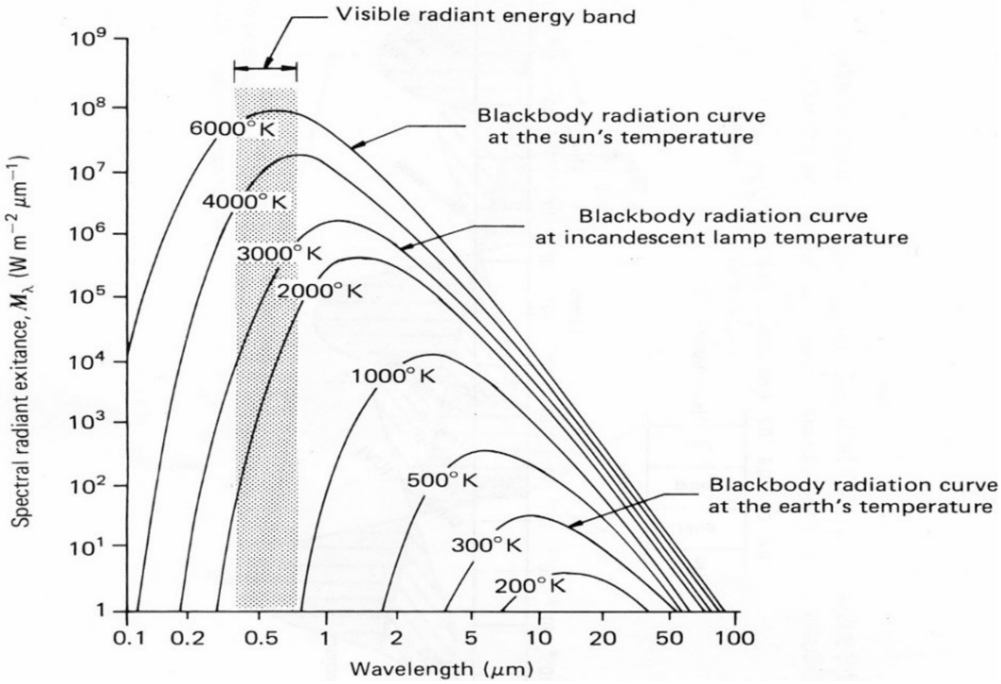

Figure 2.3.: **Distribution of Energy Radiated from Black Bodies at Various Temperatures**

Source: Menzel, 2006

2.2.1.2. *Stephan-Boltzmann law of thermal radiation*

Stephan-Boltzmann's law of thermal radiation is a derivative of Planck's law. This radiation law states that the radiation flux of an object is proportional to the fourth power of its absolute temperature, as presented in Equation (2.3) (Schmittner, 2018).

$$E = \sigma T^4 \tag{2.3}$$

Where E is the radiated energy in W.m^{-2}, σ is the Stephan-Boltzmann constant (5.67x10^{-8} W m^{-2} K^{-4}) and T is the absolute temperature of the object.

For example, if we consider a black body with surface A temperature T_1 which radiates to another black body with surface temperature T_2 that completely surrounds it, this second blackbody will totally absorb the incident energy and emit radiant energy that is proportional to T_2^4 as expressed in Equation (2.4).

$$E = \sigma A(T_1^4 - T_2^4) \tag{2.4}$$

For a non-black body that does not emit all the incident energy, ε is introduced in the equation to take into consideration the real nature of the radiant bodies. Therefore, the amount of heat transfer from a real body at temperature T_1 which is surrounded by a black body at temperature T_2 is given by Equation (2.5).

$$E = \sigma A\varepsilon_1(T_1^4 - T_2^4) \tag{2.5}$$

Thus, all objects emit radiation as a function of their temperature and hotter objects emit more electromagnetic radiation per unit surface area (Figure 2.4).

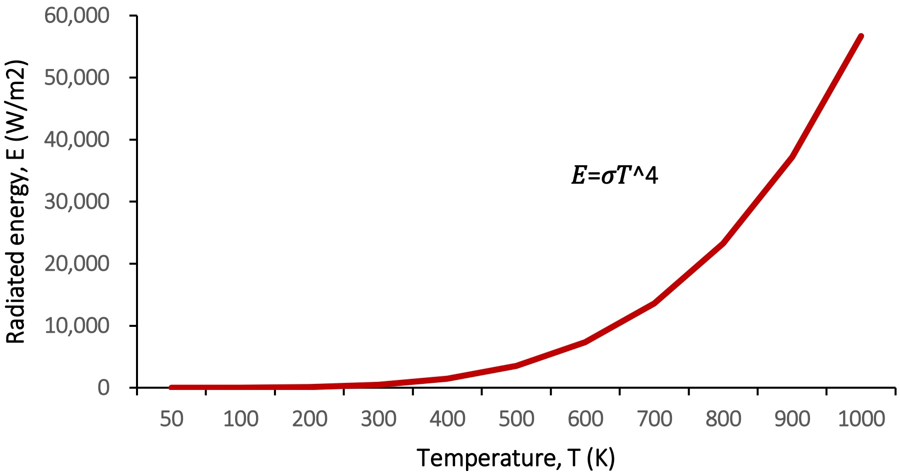

Figure 2.4.: Evolution of Radiation Flux According to Temperature

Source: Data analysis (2023)

2.2.1.3. *Wien's displacement law*

Wien's displacement law is also a derivative of Planck's law. It states that the wavelength of the peak radiation emitted by an object is inversely proportional to its absolute temperature, as shown in Equation (2.6).

$$\lambda_{peak} = \frac{\alpha}{T} \tag{2.6}$$

Where λ_{peak} is the wavelength of the peak intensity of radiation, α is Wien constant (2,898) and T is the absolute temperature of the object.

Wien's law can be used to predict the peak of a black body curve in case the temperature of the emitting object is known. In addition, Wien's law informs that in reflectance remote sensing, short wavelengths in the visible and short-wave infrared domains are used, because the earth's surface is cooler; whereas in thermal remote sensing, longer wavelengths from 2 to 14 micrometres are used because solar radiation is hotter (Tempfli *et al.,* 2009).

2.2.2. Theory of black-bodies and emissivity

A black body is a theoretical object that absorbs and emits all incident energy; it is a perfect absorber and a perfect radiator, according to Planck's law. The emissivity of such an object is by definition equal to 1 and naturally, true black bodies do not exist (Prakash, 2000). Materials that absorb and radiate only a certain fraction, constant for all wavelengths, compared to a black body are called grey bodies. A grey-body curve is identical, in shape, to a black-body one, but the absolute values are lower as it does not radiate as perfectly as a black body (Tempfli *et al.,* 2009). There are also the group of objects called selective radiators which radiate only a certain fraction of absorbed energy. A selective radiator may radiate perfectly in some wavelengths, whilst acting as a very poor radiator in other wavelengths.

The fraction of energy radiated by an object, compared to a real black body, is called emissivity (ε_λ). The emissivity for ice is 0.97, that for water is 0.96, and it varies between 0.8 and 0.9 for snow; then water and ice are almost perfect black-bodies (Schmittner, 2018). Equation (2.7) shows how to derive the emissivity.

$$\varepsilon_\lambda = \frac{B_{\lambda,T}}{B_{\lambda,T}^{bb}} \tag{2.7}$$

Where $B_{\lambda,T}$, is the spectral radiance of a real material at a given temperature, and $B_{\lambda,T}^{bb}$ is the spectral radiance of a black body at the same temperature.

2.2.3. Theory of radiant and kinetic temperature

The thermal infrared sensor records the spectral radiance reaching the sensor for a given wavelength. Given that the amount of energy radiated depends on the temperature and emissivity, a cold object with high emissivity can radiate as much energy as a considerably hotter object with low emissivity. Using Planck's law, the ground temperature can directly be calculated considering the object as a black body that emits a certain amount of radiation in a given wavelength. This calculated temperature is the radiant temperature (T_{rad}) or brightness or Top of Atmosphere (TOA) temperature. In most cases, the radiant temperature is smaller than the true kinetic temperature (T_{kin}) which is measured using a contact thermometer on the ground. To calculate the true kinetic temperature from the radiant one, the emissivity must be determined and afterwards, apply Equation (2.8).

$$T_{rad} = \varepsilon^{1/4} T_{kin} \tag{2.8}$$

For this research, the urban materials were considered as grey bodies which temperature is higher than zero kelvin. The theory of radiation, including Planck's law and Stephan-Boltzmann's law and the theory of emissivity, were employed in the calculation of LST.

2.2.4. Theory of anthropogenic global warming

Anthropogenic Global Warming (AGW) is a catastrophic climate scenario which states that projected and anticipated long-term increases in the temperature of the earth is mainly due to human activities (Stallinga and Khmelinskii, 2016). Since the mid-20th century, many climate scientists have gathered measurements on various weather phenomena (i.e., temperature, precipitation, atmospheric chemical composition) which showed that the earth's climate has changed since the beginning of the geologic time and that the influence of anthropogenic activities since at least the industrial revolution has highly driven that change (Ouellette, 2008; Selin and Mann, 2021).

Following the growing conviction of the scientific community on anthropogenic climate change, the Intergovernmental Panel on Climate Change (IPCC) was established in 1988 by the World Meteorological Organization (WMO) and the United Nations Environmental Programme (UNEP) to provide governments at all levels with regular assessments of the scientific basis of climate change, its impacts and future risks, and options for adaptation and mitigation (IPCC, 2013b). By the early 2000s, the theory of AGW gained a high scientific consensus (Powell, 2017), because pieces of evidence from ground-based studies and satellites measurements of land surface and oceans revealed a temperature increase related to carbon dioxide (CO_2) level rise since the pre-industrial time due to global economic and population growth (energy production, transport, industry, buildings, agriculture-forestry-and other land use) (Johnson *et al.,* 2017). It is estimated that the CO_2 level rose from 278 parts per million (ppm) during the pre-industrial era to 315 ppm in 1957 and over 420 ppm in June 2022_(NOAA, 2022).

Furthermore, the IPCC Fifth Assessment Report revealed that the period from 1880 to 2012 experienced a global average temperature increase of 0.85°C (IPCC, 2013a) and the special report produced in 2018 mentioned that human activities have caused a global warming of about 1.0°C above pre-industrial level, with a likely range of 0.8°C to 1.2°C (IPCC, 2019). The estimated AGW is increasing at 0.2°C per decade and it may reach 1.5°C between 2030 and 2052 if the current trend persists. Based on the available evidence, this study sought to understand the influence of LULC changes, as an anthropogenic factor, on the trends in urban LST.

In this study, since a perfect blackbody does not exist in natural state, the theory of emissivity is considered and the Planck's law for grey body is used in the computation of the LST. Indeed, though the surface materials have different temperatures due mainly to the wavelength of incident radiation and the emissivity, the skin temperature of a surface is determined by integrating the emissivity value with the radiant or TOA temperature. Furthermore, the changing of LULC has implications on the land thermal properties by decreasing the albedo and then increasing the heat storage capacity and consequently extending the time range of longwave radiation emission. Based on the theory of anthropogenic global warming, the infrared outgoing longwave radiation contribute to enhance the atmospheric temperature given the greenhouse effect. In addition, LULC changes and LST are considered as the main variables causing urban ecology and liveability deterioration, and consequently affecting its sustainability (Figure 2.5).

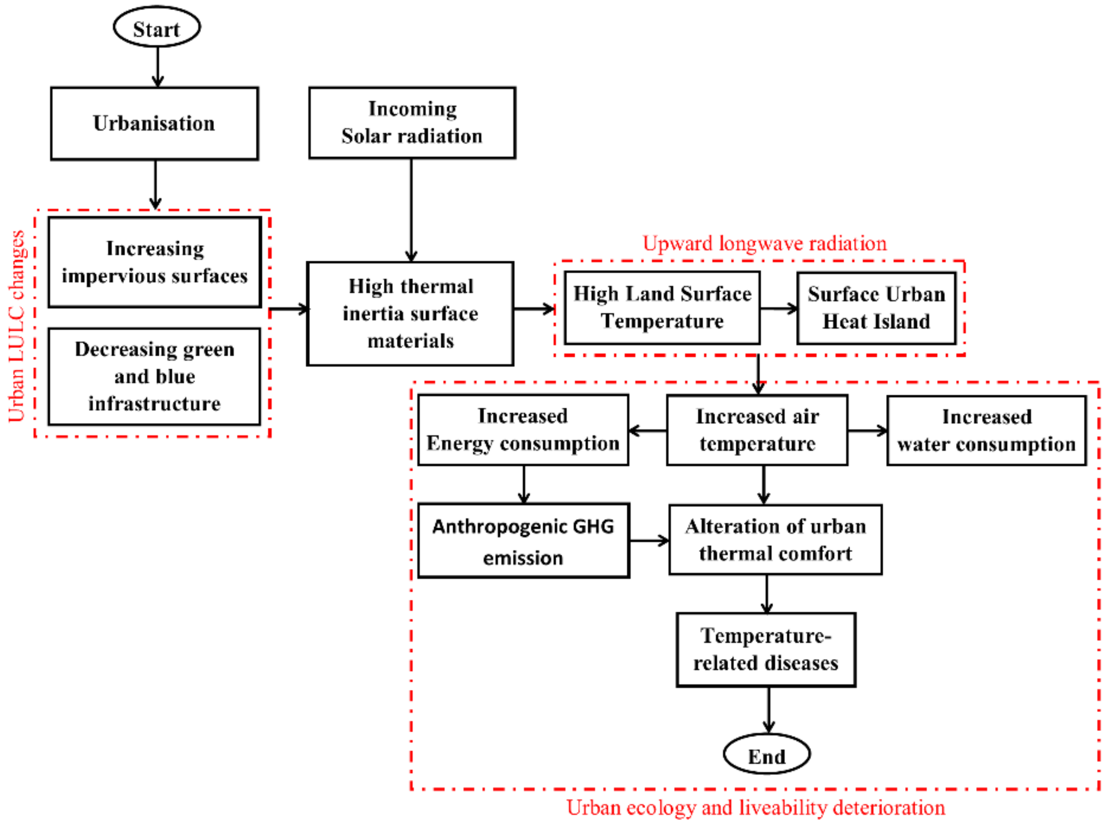

Figure 2.5: Conceptual Framework for the Study

Source: Author's field survey (2021)

2.3. Review of Related Studies

2.3.1. Remote sensing and urban land use/land cover assessment

Urban areas are growing in term of human population and spatial coverage. The assessment of this growth is important for better decisions making and implementation. Due to the low availability of reliable urbanisation data, remote sensing tools are increasingly used to assess the urban LULC changes (Schug *et al.,* 2018). A study on land cover change quantification, within Ouagadougou's metropolitan area, using Landsat imagery with support vector regression method found that the area went through a rapid urban expansion and densification. The methodology used can be replicated to other sites and the results may be strengthened by integration of new datasets including Sentinel images or the use of cloud computing platforms such as Google Earth Engine (GEE).

Relatedly, the temporal dynamics of urban growth was investigated in Kumasi, using 20-years Landsat time series and employing Random Forest (RF) and Support Vector Machine (SVM) algorithms in GEE platform (Hackman *et al.,* 2020). The results showed that the city has extended beyond its administrative boundaries. Fundamentally, the study demonstrated the capability of multi-temporal satellite images and GEE platform for quantifying the spatial and temporal dynamics of cities in developing countries.

Landsat satellite images were also used to examine the changes in urban LULC and its implications for urban climate in India (Patra *et al.,* 2018). The research found that the urban area has evolved in respect of concrete areas; and affected the urban climate by increasing the temperatures and reducing the rainfall. Moreover, urban LULC changes led to the absorption of high amount of heat, low evapotranspiration due to lack of vegetation, and low evaporation due to increased surface runoff (Porson *et al.,* 2010; Fu and Weng, 2016). Despite the existence of numerous studies that used Remote Sensing images to assess quantitatively the LULC changes in urban settings, the utilization of multi-temporal satellite images combined with ground consistent reference samples remain less investigated, especially in Burkina Faso.

2.3.2. Land surface temperature retrieval

The lack of temperature stations to estimate LST over most of the urban areas makes its study challenging. The satellite data offer a proxy of LST through the thermal infrared images (Heat and Protocol, 2015). Satellites record a series of images over different spectral range and some of them focus on the longwave radiations emitted by the earth's surface. So, the thermal sensors capture the radiation emitted from the ground to estimate the surface temperature, the surface emissivity, the soil moisture and the evapotranspiration (Sekertekin and Bonafoni, 2020). Many research works have treated the subject of deriving LST through Satellite thermal images. Liu and Zhang (2011) combined data from Landsat and ASTER to assess the UHI in Hong Kong. The methodology employed used two algorithms including mono-window and split-window to determine the LST and correlate it with biophysical indices in the study area.

The correlation between the LST and the Normalized Difference Vegetation Index (NDVI) and the Normalized Difference Built-up Index (NDBI) indicated that the vegetated lands weaken the UHI effect, while the built-up surfaces contribute to its increase. Stroppiana *et al.* (2014) used Moderate Resolution Imaging Spectroradiometer (MODIS) 8 days LST product at 1 km spatial resolution to establish the correlation between the LST, LULC, topography and solar radiation in Italy. The results showed that the topography and LULC types influence the surface temperature with its variability changing with the season. Satellite based LST was also used reliably to predict the average air temperature within areas with limited coverage in ground observation stations, by the means of mixed model regression technics (Kloog *et al.,* 2014).

Landsat thermal infrared data have been widely used to assess the surface temperature in various region of the world. Pal and Ziaul (2017) used Landsat TM, Landsat OLI and TIRS data to detect LULC and LST in India, while Mustafa *et al.* (2020) used Landsat time-series imagery to study the impact of urban renewal on LST changes, employing single-channel algorithm. Other studies also made a comparative analysis between LST from Advanced Spaceborne Thermal Emission and Reflection Radiometer (ASTER) and that from Landsat. In most cases, the two sensors presented a similar pattern for different classes of surface temperature (Boori *et al.,* 2015). The previous research studies have used various sensors data, such as ASTER, MODIS-Terra, Landsat TM, ETM+ and TIRS to assess the spatio-temporal trend of LST in diverse regions of the world. However, studies related to the assessment of LST in the study area are lacking.

2.3.3. Urban LULC changes and LST

Many research works have been done all over the world on the relationship between LULC and LST (Kayet *et al.,* 2016; Ali *et al.,* 2017; Y. Deng *et al.,* 2018; Fonseka *et al.,* 2019; Shi *et al.,* 2021). For example, it was demonstrated that deriving LST from satellite images is a challenging task because of the atmospheric absorption and the different emissivity levels of earth surface materials (Boori *et al.,* 2015). Most of the studies made a correlation analysis between LST and LULC through spectral indices such as NDVI and NDBI. The findings showed that the NDVI has a negative correlation with the LST, while the NDBI showed a positive correlation (Pal and Ziaul, 2017; Al Kafy *et al.,* 2019; Barbierato *et al.,* 2019; Guha *et al.,* 2020; Ramaiah *et al.,* 2020; Shi *et al.,* 2021). The built-up surfaces affect the LST within vegetated areas, mainly during heatwaves, and then contribute to making the cooling effects of urban vegetation non-linear (Alavipanah *et al.,* 2015). In a similar way, urban areas with high building and population densities combined with rapid landscape changes exhibit high LST values (Qiao *et al.,* 2020).

In West Africa, some authors have also investigated the relationship between the LULC and the LST (Lindén, 2011; Di Leo *et al.*, 2016; Ogunjobi *et al.*, 2018; Dissanayake *et al.*, 2019a; Tafesse and Suryabhagavan, 2019; Stemn and Kumi-Boateng, 2020). For instance, Stemn and Kumi-Boateng (2020) examined the LST changes and its effects on UHI in Ghana, employing Multi-temporal Landsat images to assess the changes in the two variables in the area. The results showed that LST and UHI have increased because of the growth in urban settlements and mining activities. Di Leo *et al.* (2016) also investigated the role of green infrastructure in LST mitigation in Bobo-Dioulasso using Landsat imagery. The results showed a concommitant rising trend of urbanisation and LST in the city. The green infrastructure were proved to lower the LST compared to the surrounding impervious land. Furthermore, the impact of urban surface characteristics and socio-economic variables on LST's spatial variation was investigated in Lagos City, Nigeria (Dissanayake *et al.,* 2019a). The results showed that rapid urbanisation in the area and the economic development have changed the distribution of the LST.

The previous research focused on the correlation between the LST and some spectral indices including NDVI and NDBI. A deeper analysis on the LST patterns regarding the LULC classes proportion and changes at the pixel scale was not performed, especially in the study area.

2.3.4. LST and diseases prevalence

In the context of climate change, the study of the link between climate parameters and the outbreak of some diseases are necessary to develop mitigation/adaptations strategies. Several research studies focused on the impact of climatic parameters and diseases incidence. Some studies have established that air temperature influences the development of the malaria and dengue vectors, the maturation temperatures of which vary between 22°C (*Plasmodium malariae*) to 25°C (*Plasmodium vivax*), 30°C (*plasmodium vivax*) and 35°C (*Aedes. Aegypti, Aedes albopictus* and *Aedes polynesiensis*) (Chastel, 2006). In the past, the prevalence of *Plasmodium falciparum* malaria epidemic occurred in countries such as Zambia, Colombia, Madagascar, Pakistan, were attributed to global warming. In particular, an increase in the temperature extreme values could modify the distribution of malaria and dengue (Githeko *et al.,* 2000).

In Bobo-Dioulasso, Burkina Faso, air temperature was found to be negatively correlated with malaria prevalence (Millogo *et al.,* 2022). Despite the rising trend of air temperature due to climate change, there is not a known direct relationship with the *Plasmodium falciparum* malaria and dengue incidence (Githeko *et al.,* 2000). A global recession of these diseases is often explained by insufficient disease control actions coupled with a rapid urbanisation and economic growth (Gething *et al.,* 2010).

On the contrary, meningitis is found to have a positive correlation with temperature variation, in such a way that when the temperature increases, the risk of meningitis increases (Chen *et al.,* 2022). Meanwhile, there has not been significant research on the relationship between air temperature and diseases. Quite interestingly, literature search yielded no results for the nexus between LST and diseases incidence in the area.

2.3.5. Future LULC and LST prediction

The urbanisation related LULC change is getting increased and to comprehend the trends of different LULC classes ahead of time, prediction operations need to be performed. Most of the models used to predict future LULC were based on the combination of Cellular Automata (CA) and Markov Chain (MC) models (Rimal *et al.,* 2017; Hamad *et al.,* 2018; Faichia *et al.,* 2020; Tariq and Shu, 2020) or MC and Neural Network (NN) models (Lukas *et al.,* 2023). The individual models were not capable of providing the quantity of future changes in LULC and the spatial distribution segment. For instance, the MC is a stochastic model that computes the state of a system with random variables that change through time (Soesbergen, 2016). MC determines the transitions probability and predict quantity of land that would change from the latest date to the predicted date (Dadhich and Hanaoka, 2011). The CA model is a spatial grid-based model where each change state is a function of time according to a defined set of rules that includes the neighbouring cells.

The combined CA-MC model simulation process is such a way that the MC determines the quantity of land that would change from the latest date to the predicted date and the output is a probability matrix file that is used by the CA to evaluate the spatial change

(Rimal *et al.,* 2018). The couple MLP-NN-MC model was widely used for LULC future prediction (Leta *et al.,* 2021; Mungai *et al.,* 2022). The MLP-NN is a robust machine learning algorithm which is capable of modelling spatially many transition potentials at once (Eastman, 2020a). The coupled models performed well in TerrSet environment with k statistics values greater than 80% in all studies, indicating the ability of the model to predict future LULC changes. In Burkina Faso, Yangouliba *et al.* (2022) used MLP-MC model in TerrSet Land Change Modeler (LCM) to predict future LULC in the *Nakambe* River Bassin. The findings revealed an increase in anthropogenic surfaces such as built-up at the expense of natural vegetated areas. Other customized models including SLEUTH model (Sakieh *et al.,* 2015), Conversion of Land use and its Effect (CLUE) model (Moulds *et al.,* 2015) and Patch-generating Land Use Simulation (PLUS) model (Deng and Quan, 2022) were also employed to simulate future LULC changes.

2.4. Examples from Other Regions

The link between urban LULC, topography and LST has been investigated in other regions of the planet. Indeed, in Asia, an investigation on the impacts of LULC changes on LST in Beijing city was conducted by Jiang and Tian (2010). The Temperature-vegetation index (TVX) approach was applied with Landsat images to assess the link between LULC change and LST. The findings revealed that LULC change towards built-up surfaces was a key driver of increasing LST. Similarly, the correlation between the LST and topographic elements was studied in Hangzhou, China by Peng *et al.* (2020). The findings showed that the elevation and slope are negatively correlated with LST, while shaded relief is positively correlated. In addition, Estoque *et al.* (2020) conducted heat-health risk assessment in Philippine cities using MODIS daytime and night-time LST product and socio-ecological indicators. The results indicated that UHI effects are more pronounced in the core area of the cities where built-up and other impervious surfaces occupy a larger area than open spaces and vegetation. Moreover, the heat-health risk occurs during daytime and night-time as well, with a higher impact during the day. The study emphasized the need to consider both daytime and night-time LST in heat health risk assessment research.

In Europe, Alavipanah *et al.* (2015) used LULC and LST data coupled with statistical methods to study the role of vegetation in mitigating LST in Munich, Germany. The findings indicated a high cooling effect of vegetation in the areas with 70-80% of vegetation cover within a grid cell. Moreover, it was demonstrated that the LST within the vegetated areas is influenced by the surrounding built-up features. The study concluded that in terms of mitigating urban LST by means of greening areas, there is not a linear relationship between the lowest/highest LST and the amount of greening to develop. In Italy, MODIS data was used by (Stroppiana *et al.,* 2014) to investigate the variability of LST regarding topography, LULC and solar radiation. The findings showed that topography strongly influenced LST variability and the correlation between LST and solar radiation is strong when coupled with the topography variable. Like findings from other studies, urbanised areas showed an increasing LST trend.

In America, the response of UHI to urban expansion in the United States was assessed by Li *et al.* (2017). The study highlighted that the urban area size variation influences the UHI patterns. Moreover, it was demonstrated that the variation of UHI regarding the increase in size of an urban area is significant when the surrounding landscape has homogenous thermal characteristics. The driving forces of LST anomalous in Northern America were also researched. The findings indicated that the vegetation distribution and atmospheric water vapour influenced the changes in LST (Yan *et al.,* 2020).

In Africa, few studies have investigated the nexus between LULC and LST and the related effects on human health. A study in Ethiopia on the link between LULC changes and LST showed that the development of impervious surfaces at the expense of vegetation areas, leads to an increasing in LST and consequently the UHI intensification (Tafesse and Suryabhagavan, 2019). Employing Gradient analysis and Partial Least Square (PLS) regression analysis technics, Dissanayake *et al.* (2019a) assessed the spatial patterns of LST over Lagos 'city, Nigeria. The results showed that the LST distribution changed over the study period due to the variations in characteristics in the urban environment and the influence of economic activities. In Addis Ababa, Ethiopia, the assessment of the impact of landscape structure on LST variation, through gradient analysis and intensity calculation with Landsat images, showed that the impervious surfaces are the major impacting variable and its fraction declines from the city centre towards the urban fringe (Dissanayake *et al.*, 2019b).

In Burkina Faso, very few studies were conducted on the subject matter. Indeed, Di Leo analysed the role of green infrastructure in LST mitigation in Bobo-Dioulasso, using Landsat thermal images (Di Leo *et al.,* 2016). The findings showed that the green areas displayed lower LST than the other LULC units. In terms of surface energy budget, Ouagadougou city experienced a reduction of albedo against an increasing trend of Sensible heat fluxes toward the downtown, due to the multiplication of concrete surfaces (Offerle *et al.,* 2005). In addition, the evapotranspiration from vegetated areas is seen to be responsible for night cooling while the proximity of open water is a key factor in daytime cooling in hot-dry cities (Lindén, 2011).

2.5. Overview and Key Issues of the Study

The previous studies emphasized the spatiotemporal variation of LST and its relationship with LULC in urban areas. Remotely sensed and ground observations data were used to map LULC, through supervised and unsupervised classification methods, to assess the LST patterns. In the study area, an unsupervised method was done with Landsat data to map the LULC and retrieve the surface temperature in Bobo-Dioulasso (Di Leo *et al.,* 2016). In Ouagadougou, observation data were used to characterize the nocturnal cool island of the city (Lindén, 2011). Overall, these studies focused on one city without any comparison possibility with others. Again, these studies did not undertake time series analysis of LULC change and LST trends for the sites that were investigated. In addition, machine learning algorithms combined with cloud computing platform have not been used to map LULC in the study area. Moreover, the response of LST to rapid urbanisation was not researched in the study area. More importantly, only a few research studies investigated the link between air temperature and diseases such as malaria, dengue, meningitis.

Of significant interest to the present research, however, is that the link between the urban LULC change induced LST and the aforementioned diseases has never been done in the specific study sites chosen for this work. It remains then a relevant research area since many African cities are growing rapidly with significant effects on LST patterns. The present research attempts to fill these gaps by using Landsat time-series surface reflectance imagery, MODIS Aqua LST product with machine learning algorithms to determine the LULC evolution and derive the urban LST. The relationships between the LULC dynamics and LST and that between some diseases (malaria, dengue and meningitis) and LST have been investigated.

CHAPTER THREE

3.0. MATERIALS AND METHODS

3.1. Description of Materials

This subsection presents the different datasets used in the research. It includes remote sensing data, meteorological data, ground reference and socio-economic datasets.

3.1.1. Description of remote sensing data

For this research, the remote sensing data included Landsat images, MODIS LST images and Shuttle Radar Topographic Mission Digital Elevation Model Version 3 (SRTM V3) image. Landsat satellite images ranging from 2003 to 2021, for the sensors Thematic Mapper (TM) carried by Landsat 5, Enhanced Thematic Mapper Plus (ETM+), carried by Landsat 7, and Operational Land Imager (OLI) carried by Landsat 8 were used. Landsat 5 and 7 acquire data in descending (daytime) mode, while Landsat 8 operates both in descending and ascending (occasionally) mode. For this study, the images from the daytime mode were used. In addition, MODIS Land Surface Temperature (LST) from the Aqua satellite was used to compute the LST over the study area.

The present research used MODIS Aqua rather than Terra because it provides both day and night-time LST data, passes over the study area around the peak emission time (1:30 pm). Aqua also has a daily temporal resolution, while other satellites such as Landsat sensing time is around 10:30 am and does not provide night-time LST and has a coarse temporal resolution of 16 days. Despite its coarse spatial resolution, MODIS Aqua is useful for surface temperature study. Furthermore, the 30 metres spatial resolution SRTM image was used to generate the topographic elements (elevation, slope, aspect) of the study area. These topographic elements were considered as predictors in the image classification to help enhance the discrimination level between the different LULC classes. The choice of SRTM was motivated by the fact that it provides higher vertical accuracy (than ASTER for instance) digital elevation model of the earth (Farr *et al.,* 2007; Forkuor and Maathuis, 2012). The voids have also been filled in this version of the dataset using non-commercial data such as ASTER Global Digital Elevation Model (GDEM) version 2 and Global Multi-resolution Terrain Elevation Data 2010 (GMTED2010) (NASA, 2000). Table 3.1 shows the summary of the remote sensing data used.

Table 3.1.: Summary of the Remote Sensing Data Used

Sensor	Resolution	Period	Usage	Source
Landsat TM	30 m	2003-2012	Extraction of surface reflectance information	Google Earth Engine Data Catalogue
Landsat ETM+	30 m	1999-2021		
Landsat OLI	30 m	2013-2021		
MODIS Aqua LST	1000 m	2003-2021	LST computation	
Image SRTM V3	30 m	2000	Generation of elevation and slope	

Source: Author's field survey (2022)

3.1.2. Description of meteorological data

The meteorological data required for this research included daily air temperature data and daily rainfall data. Ground observation datasets involving daily rainfall and daily air temperature datasets were collected from the National Meteorological Agency (ANAM) of Burkina Faso and used for the study area description. Additional datasets including reanalysis (model data combined with observation data) hourly air temperature data were collected from the European Centre for Medium-Range Weather Forecasts Reanalysis version 5 (ECMWF/ERA5) and utilized to establish the relationship between 2 m above ground air temperature and LST. The reanalysis data have an original spatial resolution of 11,132 metres and ranged from 2003 to 2021 as the ground station data. Table 3.2 presents the details of the meteorological data.

Table 3.2.: Details of the Meteorological Data Used for the Study

Data type	Resolution	Usage	Source
Air temperature data (min, max)	Daily	Study area description	National Meteorological Agency-Burkina Faso
Air temperature reanalysis data (mean)	Hourly	Air temperature trend analysis, LST gap-filling	ECMWF/ERA5-Land (Google Earth Engine Data catalogue)
Surface latent heat flux	Hourly	Energy budget patterns description	
Surface sensible heat flux	Hourly		
Rainfall data	Daily	Study area description	National Meteorological Agency-Burkina Faso

Source: Author's field survey (2022)

3.1.3. Description of reference samples and socio-economic data

The reference samples were collected using Very High Resolution (VHR) images from Google Earth Pro. Moreover, statistical data on temperature-related diseases (reported cases) were gathered from the Ministry of Health, Burkina Faso, to assess the health impact of LST. Table 3.3 shows the details of the socio-economic and reference data used.

Table 3.3.: Details of Socio-Economic Data Used for the Study

Data type	Resolution	Usage	Source
Temperature-related disease statistics	District level	LST and diseases relationship	Ministry of health, Burkina Faso
Reference samples (training and testing)	Yearly	LULC classification	Google Earth Pro VHR images

Source: Author's field survey (2022)

3.2. Description of Methods of Data Collection

In this subsection, the different methods employed in the data collection process are described. The subsection involves three sub-subsections: remote sensing data collection methods, meteorological data collection methods and field data collection methods.

3.2.1. Remote sensing images collection

For this study, the satellite images from Landsat 5, Landsat 7, Landsat 8 OLI, provided by the United States Geological Survey (USGS) were freely assessed from Google Earth Engine (GEE) data catalogue (https://code.earthengine.google.com). A search was made through Landsat collections, from 1st October to 31st December, each year, to identify the available images covering Ouagadougou Metropolitan area and Bobo-Dioulasso Metropolitan area as well. That procedure allowed for the collection of the longest possible time-based urban land use history of the study area (Hackman *et al.,* 2020).

Landsat satellites have a repeat cycle of sixteen (16) days, which means that the entire Earth is covered every sixteen days. The study area is covered by three Landsat scenes with the following references according to the Worldwide Reference System (WRS) version 2: path 195, row 51 for Ouagadougou and path 197, row 52; path 196, row 52 for Bobo-Dioulasso (Figure 3.1). Ouagadougou is sensed on cycle day number 4, between 09:30 am and 10:30 am, while the satellite passes over Bobo-Dioulasso on cycle day number 2 between 10:05 am and 10:38 am. That means, in a month there is a maximum of two images covering the study area.

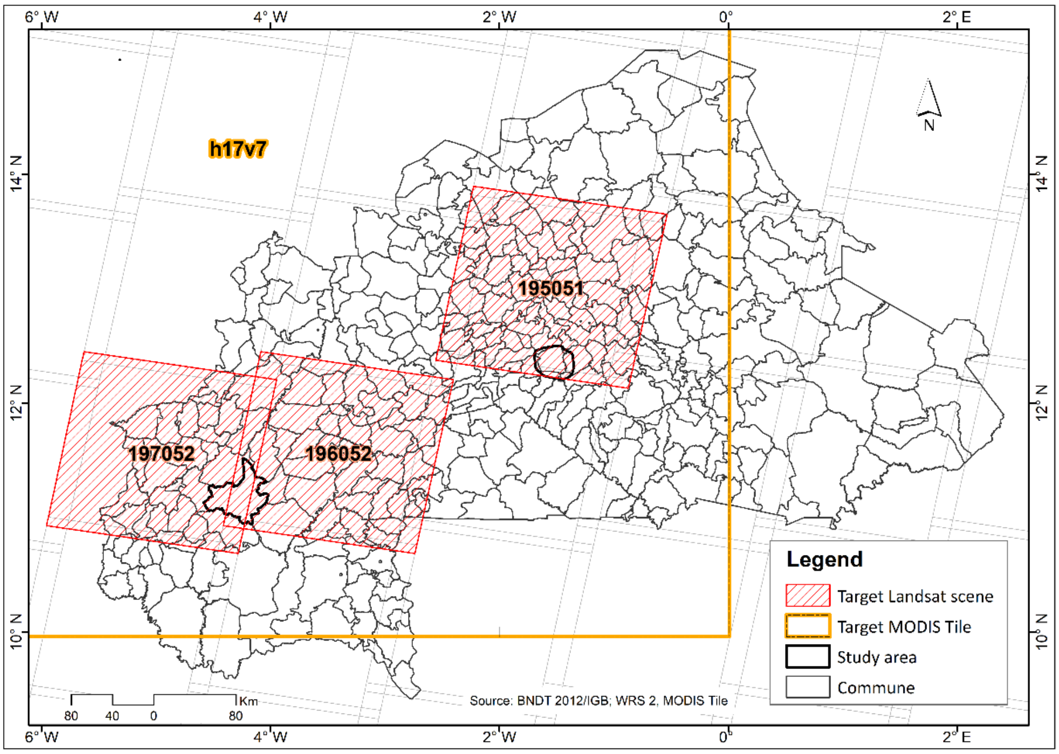

Figure 3.1.: **Localisation of Landsat Scenes and MODIS Tiles Covering the Area**

Source: Author's field survey (2022)

Landsat 5 and Landsat 7 have both four Visible Near Infrared (VNIR) bands namely Blue (band 1), Green (band 2), Red (band 3) and Near-Infrared (band 4) at 30 m spatial resolution. They also have two Short-wave Infrared (SWIR) bands: SWIR 1 (band 5 SWIR 2 (band 7) and one thermal band (band 6) with an original spatial resolution of 60 metres, which was resampled to 30 metres for harmonization purpose with the other spectral bands. In addition to these bands, Landsat ETM+ has a panchromatic band (band 8) with 15 metres spatial resolution.

Landsat 8 carries two sensors namely Operational Land Imager (OLI) and Thermal Infrared Sensor (TIRS). The OLI sensor comprises one coastal aerosol band (band 1); four VNIR bands: Blue (band 2), Green (band 3), Red (band 4) and Near-Infrared (band 5); two Short-wave Infrared (SWIR) bands: SWIR 1 (band 5 SWIR 2 (band 7); one Cirrus band (band 9), all at 30 metres spatial resolution (USGS, 2019). It also records images for one panchromatic band (band 8) at 15 m spatial resolution. The TIRS sensor collects data for two thermal bands (band 10 and band 11) at 100 metres original spatial resolution, resampled to 30 metres (USGS, 2019). The VNIR and SWIR bands were used to assess the LULC dynamics in the study area, from 2003 to 2021.

In addition to Landsat images, MODIS LST data (Tile h17v7) were used for analysing the LST patterns in the study area. MODIS is a sensor onboard polar-orbiting satellites, Aqua and Terra. The Terra platform was launched in December 1999 and Aqua was launched in May 2002 (Chang *et al.,* 2018). The Terra equatorial crossing time is around 10:30 am in descending mode and 10:30 pm in ascending mode, while Aqua overpass time is around 1:30 pm in ascending mode and 1:30 am in descending mode (Wan *et al.,* 2004). It has 36 spectral bands with wavelengths ranging from 410 nm to 14,400 nm (Xiong *et al.,* 2006). The bands' spatial resolutions vary from 250 metres (bands 1-2) to 500 metres (bands 3-7) and 1,000 metres (bands 8-36) (Xiong *et al.,* 2006).

For this research, Google Earth Engine (GEE) platform was used. GEE is a cloud-based geospatial analysis platform which provides easy and instant access to satellite products and the necessary computing resources for direct processing on the platform (Parastatidis *et al.,* 2017), without the need for downloading and storing in local system (Gorelick *et al.,* 2017). There are many types of data in the GEE catalogue, but for this research two types of datasets were used: Landsat 5 - TM, Landsat 7 - ETM+, Landsat 8 - OLI surface reflectance data and MODIS Aqua daytime and night-time LST product.

3.2.2. Meteorological data collection

The air temperature and rainfall datasets were collected from the National Meteorological Agency-Burkina Faso. The required meteorological data for this study are daily tabular datasets covering the areas of Ouagadougou and Bobo-Dioulasso. The ERA 5-Land reanalysed hourly air temperature data were also extracted from GEE Data Catalogue. The hourly data were aggregated into daily datasets in GEE platform and exported for further time-series analyses.

3.2.3. Reference samples and socio-economic data collection

The field survey consisted of reference samples (training and testing) collection for LULC classification. Statistical data on temperature-related diseases were also collected.

3.2.3.1. ***Reference samples collection***

The reference samples were collected by observing a minimum mapping unit of 30 x 30 metres of homogeneous landscape (Forkuor *et al.,* 2018) to match the Landsat satellites images resolution (30 m). A point was then picked at the centre of each homogenous unit. The samples were collected from Google Earth Pro version 7.3.6.9345 high-resolution images through on-screen digitization.

In total, four years were considered for the LULC analysis with an epoch of six years: 2003, 2009, 2015 and 2021. The classification scheme used in this study is composed of five LULC classes including built-up, bare land, forest, agricultural land and water (Table 3.4). Agricultural areas were combined with shrub land to have agricultural land class. This is because of the fact that agricultural areas look like savannah parks in the case of cultivated areas or shrubs in the case of fallow lands. This similarity implies a spectral confusion between the two classes in the region. The class considered as bare land is composed of areas cleaned for construction or used for public activities such as football, and meetings (Hackman *et al.,* 2020) or untarred roads.

Table 3.4: **Land Use/Land Cover Classification Scheme and Description**

LULC classes	Description
Built-up	Area dominated by urban, peri-urban and rural settlements including pavement, tarred roads, and other concrete surfaces
Bare land	Surface without vegetation, building or water, untarred roads
Forest	Area occupied by urban parks, forests
Agricultural land	Cultivated lands including seasonal, permanent crops and fallows, shrubland, grassland
Water	Rivers, dams, lakes

Source: Adapted from Di Gregorio *et al.* (2000); Appiah (2016)

For the purposes of quantitative analyses and comparison, homogenous point samples were collected throughout the four years. Given that the area is in continuous urbanisation and most of the LULC classes are being transformed to built-up areas, a change logic was adopted to collect the samples. Thus, for the built-up class, the earliest image was used as reference, assuming that in urban areas the conversion from other classes to built-up is irreversible.

Moreover, to ensure that the samples are consistent throughout the period, the "Show historical imagery" tool in Google Earth Pro was employed to move forward, year after year, in order to record the pixels that remained built-up from 2003 to 2021. For the other classes (water, forest, bare land and agricultural land), the latest image was used making sure that the class of each sample is the same throughout the time series by going back in time and retaining the consistent pixels for the analysis. It is important to note that points features were created instead of polygons, because GEE treats polygons by transforming them into spatial points and more attention has to be paid to digitize same-size polygons to get strong autocorrelation between pixels within each one (Abu *et al.,* 2021).

In total, 289 and 144 homogeneous and consistent samples were collected in Ouagadougou and Bobo-Dioulasso, respectively (Figure 3.2). Ouagadougou has more samples than Bobo-Dioulasso because more cloud-free historical high-resolution images were found over this area. However, in Bobo-Dioulasso, only the central area (urban core) was covered by clear images.

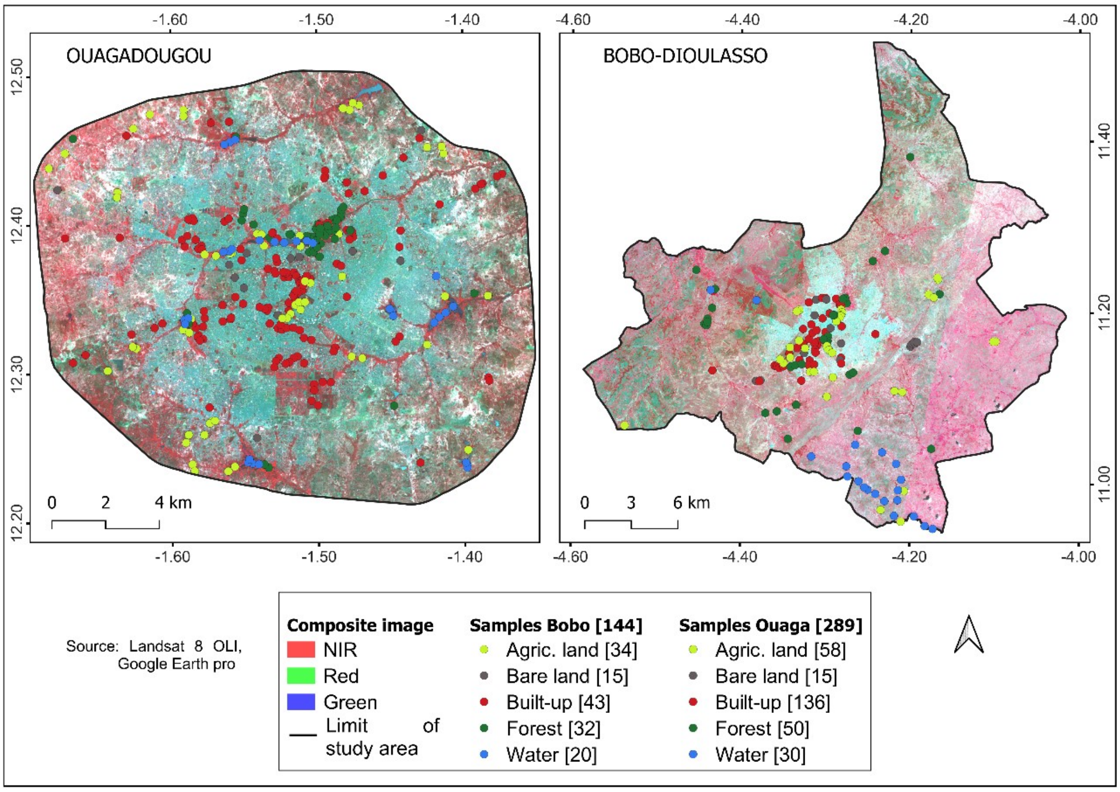

Source: Landsat 8 OLI, Google Earth pro

Figure 3.2: **Distribution of Reference Samples in the Study Sites**

Source: Author’s field survey (2022)

3.2.3.2. *Socio-economic data collection*

Data on selected temperature-related diseases were collected from the Ministry in charge of Health, Burkina Faso. The data were composed of monthly reported cases of malaria, dengue fever and meningitis from 2017 to 2021, based on data availability.

3.3. Description of Methods of Data Analysis

This subsection presents the data analyses processes, the specific methods used and the software or tools as well. It also comprises the methodological flowcharts describing graphically the steps followed to achieve each objective of the study.

3.3.1. Data analysis for land use/land cover dynamics assessment

To assess the dynamic of LULC, the analyses consisted of the pre-processing and processing of satellite images, the LULC classification and the accuracy assessment. An intensity analysis was carried out to capture the different LULC classes changes pattern.

3.3.1.1. *Satellite images pre-processing*

For this research, GEE platform was used for the LULC mapping. The satellite images for the LULC mapping were collected from Landsat 5 TM, Landsat 7 ETM+ and Landsat 8 OLI sensors, provided by the USGS. All the images were surface reflectance data from the Level 2 Collection 2 Tier 1 datasets, which are the second-generation of Landsat pre-processed products. Indeed, prior to their ingestion into GEE Data Catalogue, the images were pre-processed to at-surface reflectance level through the Landsat Ecosystem Disturbance Adaptative Processing System (LEDAPS) in the case of Landsat 5 and Landsat 7 and the Landsat Surface Reflectance Code (LaSRC) in the case of Landsat 8 OLI (USGS, 2020).

Additional pre-processing tasks including scaling and cloud masking were performed on the images. Regarding the scaling procedure, the scale factor and offset value provided in the bands description in the GEE catalogue were used to reconstitute the surface reflectance values of the images. A cloud masking, using the Quality Assessment (QA) band, was also done on images with low cloud cover (<10 per cent). Furthermore, in May

2003, the Scan Line Corrector (SLC) onboard the Landsat 7 Enhanced Thematic Mapper Plus (ETM+) instrument failed (Singh and Prasad, 2015). The function of the SLC was to compensate for the forward motion of the satellite during data acquisition. This failure has resulted in data gaps (about 22 per cent of data lost) on each Landsat 7 scene and removed its capacity to provide spatially continuous fields, but the remaining spectral information maintains the same radiometric and geometric quality as images collected before the instrument's failure (Yin *et al.,* 2017; Asare *et al.,* 2020).

Many methods such as Weighted Linear Regression (WLR), integrated with Laplacian Prior Regularization Method (LPRM), Localized Linear Histogram Matching (LLHM), Neighbourhood Similar Pixel Interpolator (NSPI), Geostatistical Neighbourhood Similar Pixel Interpolator (GNSPI) and Multiple-Point Geostatistics (MPS) have been developed to fill the gaps. For this research, the USGS Landsat 7 gap-filling method was employed to fill the gaps in GEE platform (USGS, 2004).

3.3.1.2. *Satellite images processing*

For the LULC mapping, six atmospherically corrected surface reflectance bands, namely, Blue, Green, Red, Near-Infrared, and Shortwave-Infrared band 1 (SWIR 1) and Shortwave-Infrared band 2 (SWIR 2) were used. Assuming that the land cover type and configuration remained the same in both rainy and dry seasons, the median image for the October-December period for each year was computed from the image collections obtained for each classification year. In addition to the spectral bands, additional inputs composed of topographic derivatives (elevation, slope), as well as vegetation and some land cover specific indices were computed.

The vegetation indices useful to discriminate vegetation from other LULC classes include the Normalized Difference Vegetation Index (NDVI) (Hackman *et al.,* 2020) and

Enhanced Vegetation Index (Forkuor *et al.,* 2018). Dry Built-up Index (DBI), Dry Bare-soil Index (DBSI) and Normalized Difference Built-up Index (NDBI) (Rasul *et al.,* 2018), Bare Soil Index (BSI) and Soil Adjusted Vegetation Index (SAVI) (Polykretis *et al.,* 2020), and Normalized Difference Water Index (NDWI) (Kafy *et al.,* 2020) were the biophysical indices used. SAVI is used to correct NDVI for the influence of soil brightness in areas with low vegetation cover. BSI is used to show the difference between agricultural and non-agricultural land due to its ability to detect bare soil and fallow lands (Polykretis *et al.,* 2020). DBI and DBSI are used in combination with NDBI to help distinguish between built-up class and bare land class, rather than using only NDBI due to its inability to distinguish between the two units in dry climate (Rasul *et al.,* 2018), as in the context of Burkina Faso.

Furthermore, Principal Component Analysis (PCA), a statistical approach that reduces the dimensionality of large datasets, was performed on the median images to extract the main uncorrelated bands that contain most of the spectral information (Tassi and Vizzari, 2020). In sum, the predictors used for the image classification were composed of the median images, the vegetation and biophysical indices, the topographic elements (elevation and slope, derived from DEM image at a spatial resolution of 30 m) and the three Principal Component (PC). Table 3.5 presents the description of the different predictors used for LULC mapping.

Table 3.5: Details of the Predictors Used in the Image Classification. All predictors are calculated on a spatial resolution of 30 m. ρ_x represents the reflection in band x.

Predictor	Computation equation	Description
med(Blue)	Median from October to December	Median band of all blue bands in the period
med(Green)	median from October to December	Median band of all green bands in the period
med(Red)	median from October to December	Median band of all red bands in the period
med(NIR)	median from October to December	Median band of all NIR bands in the period
med(SWIR 1)	median from October to December	Median band of all SWIR1 bands in the period
med(SWIR 2)	median from October to December	Median band of all SWIR2 bands in the period
Elevation	Automatic	Elevation level
Slope	Automatic	Slope classes
PC1	PCA	First principal component
PC2	PCA	Second principal component
PC3	PCA	Third principal component
NDVI	$\frac{\rho_{NIR} - \rho_{RED}}{\rho_{NIR} + \rho_{RED}}$	Index to differentiate vegetation class from others
SAVI	$1.5 * \frac{(\rho_{NIR} - \rho_{RED})}{(\rho_{NIR} + \rho_{RED} + 0.5)}$	Index to account for soil noise
NDWI	$\frac{\rho_{Green} - \rho_{NIR}}{\rho_{Green} + \rho_{NIR}}$	Index to discriminate water class from others
NDBI	$\frac{\rho_{SWIR1} - \rho_{NIR}}{\rho_{SWIR1} + \rho_{NIR}}$	Index to distinguish built-up for other classes
DBI	$\frac{\rho_{BLUE} - \rho_{TIR}}{\rho_{BLUE} + \rho_{TIR}} - NDVI$	Index to distinguish between built-up and bare land
DBSI	$\frac{\rho_{SWIR1} - \rho_{GREEN}}{\rho_{SWIR1} + \rho_{GREEN}} - NDVI$	Index to distinguish between built-up and bare land

Source: Author's data analysis (2022)

3.3.1.3. *Land Use/Land Cover classification*

The image classification was performed using machine learning algorithms. Then, the collected reference datasets were divided into training and testing set to avoid overfitting (Gholamy *et al.,* 2018). In general, the best results are obtained with 70 per cent – 80 per cent of the samples assigned to training sets and 20 per cent – 30 per cent of the data for testing sets. For this study, 80 per cent of the samples were used to train the model and 20 per cent were used for testing. A pixel-based image classification method was applied using three different supervised classifiers available in GEE: Random Forest (RF), Support Vector Machine (SVM), and Gradient Tree Boost (GTB). RF is a supervised machine learning algorithm founded on an ensemble of classification trees which employs bagging operation to generate multiple decision trees (ntree) based on a randomly selected subset of training data. Each tree is then grown to its maximum size based on a bootstrapped sample from the training dataset without any pruning, and each node is split using the best among a subset of input variables (mtry) (BREIMAN, 2001). The classification is performed by using the most voted class from each tree predictor.

SVM is a non-parametric supervised learning algorithm considering that for a nonlinear separable dataset, consisting of points from two classes, all the points of one class can be separated from those of the other class by using an infinite number of hyperplanes. The best hyperplane with the largest margin between the two classes is selected by using a subset of training samples known as support vectors (Cracknell and Reading, 2014). RF and SVM have high performance in time-series image classification (Nery *et al.,* 2016), achieving good accuracies in several studies conducted in the region (Zoungrana *et al.,* 2014, Zoungrana *et al.,*2015; Forkuor *et al.,* 2015, Forkuor *et al.,*2018). GTB is a gradient boosting algorithm that uses regression trees as weak classifiers. The weak learners measure the error in each node, split the node and return the values (Son *et al.,* 2015).

3.3.1.4. *LULC post-classification majority filtering*

After producing the LULC maps from the different classifiers and in order to improve the final results, the LULC images were converted to an image collection and a vertical majority filtering (using the mode function) was performed to have a single classified image. To perform the image classification in GEE, numbers were assigned to each class (0: water, 1: Built-up, 2: Agricultural land, 3: Forest, 4: Bare land). Thus, the majority filtering process consisted of a spatial overlay of the outputs of the different classifiers after which, for each pixel, the most frequently occurring LULC class (the corresponding number) across the collection was selected as the final pixel label.

In other words, the majority voting calculated the most common class at each pixel level across the image collection. When there is one majority vote (for example: 1,1,3), the majority value is returned (the majority pixel value is 1). In case there are multiple mode values (not applicable for this study, because it used three classifiers) or there is no majority vote (for example: 2, 1, 5), the minimum pixel value is returned (the minimum value is 1). Naboureh *et al.* (2020) found an improvement in LULC maps when applying majority voting with random under sampled SVM classifications. Figure 3.3 presents how the mode filter works in GEE under different conditions of majority voting.

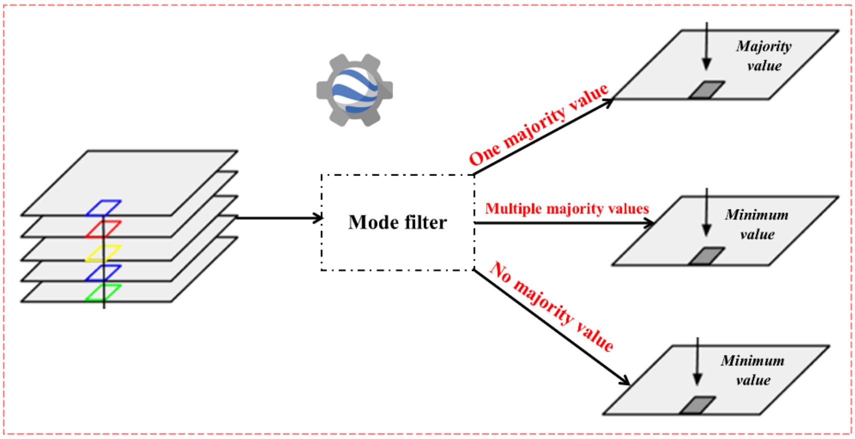

Figure 3.3: Majority Filter Process

Source: Author’s data analysis (2023)

The accuracy of the majority voting was assessed using 1 000 random points. The pixel values of the random points were extracted from the majority vote image and each of the individual classifier results. The overall accuracy of each majority image was calculated by dividing the number of majority pixels to the total number of pixels. The accuracies of the majority filtering results are presented in table 3.6.

Table 3.6: Majority Filtering Overall Accuracy

Year	Ouagadougou	Bobo-Dioulasso
2003	0.88	0.84
2009	0.89	0.86
2015	0.82	0.88
2021	0.86	0.93

Source: Author's data analysis (2023)

The final classification comes with "salt and pepper" effects due to misclassified pixels. Consequently, a post-classification horizontal majority filter (with a 3x3 neighbourhoods) was applied to replace the isolated pixels with the most common pixel values.

3.3.1.5. *Land Use/Land Cover accuracy assessment*

The accuracy of each classified map was assessed using the error matrix (Table 3.6), which is a two-entry table comparing the classified map to the actual data. Based on the different error matrices generated from the four time points classified maps, the LULC classification accuracy metrics were computed.

Table 3.7: Error Matrix Design

		Actual						
		1	2	…	j	...	q	Total t_{i+}
Classified map	1	t_{11}	t_{12}	…	t_{1j}	…	t_{1q}	t_{1+}
	2	t_{21}	t_{22}	…	t_{2j}	…	t_{2q}	t_{2+}
	⋮	⋮	⋮	⋮		⋮	⋮	⋮
	i	t_{i1}	t_{i2}		t_{ij}		t_{iq}	t_{i+}
	⋮	⋮	⋮	⋮		⋮	⋮	⋮
	q	t_{q1}	t_{q2}			…	t_{qq}	t_{q+}
	Total t_{+j}	t_{+1}	t_{+2}	…	t_{+j}	…	t_{+q}	

Source: Adapted from Mas *et al.* (2014)

The LULC maps accuracy metrics including overall accuracy (*OA*) and kappa coefficient (*k*) were computed based on the error matrix. The overall accuracy is the proportion of all pixels correctly classified in their categories (Mas *et al.,* 2014). It is computed according to Equation (3.1).

$$OA = \frac{\sum_{i=1}^{q} t_{ii}}{N} \times 100 \tag{3.1}$$

where q is the number of LULC classes, t_{ii} is the number of pixels of class i correctly classified in class *I*, N is the total number of pixels in the study area.

The kappa coefficient which is known to be more robust than the *OA* because it takes into consideration the agreement occurring by chance (Loosvelt *et al.,* 2012) was also calculated. A value of k below 0 indicates no agreement between the classified map and the observations, 0-20% means a slight agreement, 21-40% corresponds to a fair agreement, 41-60% is a moderate agreement, 61-80% shows a substantial agreement, and 81-100% indicates an almost perfect agreement (Loosvelt *et al.,* 2012). The kappa coefficient is computed following Equation (3.2).

$$k = \frac{N\sum_{i=1}^{q} t_{ii} - \sum_{i=1}^{q}(t_{i+}t_{+j})}{N^2 - \sum_{i=1}^{q}(t_{i+}t_{+j})} \tag{3.2}$$

Where t_{i+} is the total number of classified pixels in class *i*, and t_{+j} is the total number of prediction pixels in class *j*. N is the total number of prediction pixels.

3.3.1.6. *Land Use/Land Cover intensity analysis*

Intensity analysis is a mathematical framework that compares a uniform intensity to observed intensities of temporal changes among categories (Pontius *et al.,* 2013). Uniform intensity is defined as the hypothetical change intensity when the overall change occurred during a time interval was uniformly distributed, from the beginning to the end of the interval (Aldwaik and Pontius, 2012). In this study, the categories refer to the different LULC classes, namely built-up, agricultural land, forest, bare land and water. Based on the classified maps years, the time intervals include 2003 - 2009, 2009 - 2015, 2015 - 2021. Intensity analysis takes place at three levels including interval level, category level and transition level (Quan *et al.,* 2019). To perform intensity analysis, in this study, the equations based on Aldwaik and Pontius (2012) were used. The following mathematical notations were used: Y_t corresponds to the year at time point t; Y_{t+1} is the year at time point $t+1$. J is the number of categories; j is the index for a category at the latter time point of an interval; i is the index for a category at the initial time point of an interval; n is the index of the gaining category for the selected transition; C_{tij} is the size of transition from category i to category j during interval Y_t - Y_{t+1}; C_{tin} is the size of annual transition from i to n during interval Y_t - Y_{t+1}; C_{tnj} is the size of transition from n to j during interval Y_t -Y_{t+1}. C_{tnn} is the size of annual gain of n during interval Y_t -Y_{t+1}.

The interval level analyses the overall change size and the annual change intensity of the whole area in each time interval (Quan *et al.,* 2019). The annual change intensity of the study area during time interval t (S_t) is computed through Equation (3.3). Equation (3.4) shows how to compute uniform change intensity during time interval t (U_T). If $S_t < U_T$ then the change is slow. In case $S_t > U_T$ then the change is fast.

$$S_t = \frac{\text{change during interval } t}{\text{study area size}\times\text{interval } t \text{ duration}} \times 100 = \frac{\sum_{j=1}^{J}[(\sum_{i=1}^{J} C_{tij}) - C_{tij}]}{(Y_{t+1} - Y_t)(\sum_{j=1}^{J}\sum_{i=1}^{J} C_{tij})} \times 100 \qquad (3.3)$$

$$U_T = \frac{\text{change during all intervals}}{\text{study area size}\times\text{study duration}} \times 100 = \frac{\sum_{t=1}^{T-1}(\sum_{j=1}^{J}\sum_{j=1}^{J} C_{tij})}{(Y_T - Y_1)(\sum_{j=1}^{J}\sum_{i=1}^{J} C_{tij})} \times 100 \qquad (3.4)$$

The category level compares the variation in size and intensity of gross gains and gross losses across categories during each time period (Quan *et al.,* 2019). The loss intensity (L_{ti}) from a category i is the lost percentage of the start size of that category i during the time interval t (Equation 13). The gain intensity (G_{tj}) to a category j corresponds to the percentage of the end size of that category *j* that gained during the time interval *t* and is computed according to Equation (3.5). The intensity of a uniform change during time interval *t* is defined by S_t is given by equation (3.6). If $L_{ti} < S_t$ or $G_{tj} < S_t$, then the loss from category *i* or gain to category *j* during time interval *t* is dormant. If $L_{ti} > S_t$ or $G_{tj} > S_t$, then the loss from category *i* or gain to category *j* during time interval *t* is active.

$$L_{ti} = \frac{\text{loss of category } i \text{ during interval } t}{interval\ t\ duration \times \text{size of category } i \text{ at start time}} \times 100 = \frac{\sum_{i=1}^{J} C_{tij} - C_{tii}}{(Y_{t+1} - Y_t)\sum_{i=1}^{J} C_{tij}} \times 100 \quad (3.5)$$

$$G_{tj} = \frac{\text{gain of category } j \text{ during interval } t}{interval\ t\ duration \times \text{size of category } j \text{ at end time}} \times 100 = \frac{\sum_{i=1}^{J} C_{tij} - C_{tij}}{(Y_{t+1} - Y_t)\sum_{j=1}^{J} C_{tij}} \times 100 \quad (3.6)$$

The transition level computes for each time interval how each category's transitions vary in size and intensity across (Pontius *et al.,* 2013). The transition intensity from category i to category n during time-interval t (R_{tin}), where *i* is different from *n*, is defined by equation (3.7). Equation (3.8) presents the uniform or hypothetical transition intensity to category n during time interval t (W_{tn}). In case $R_{tin} < W_{tn}$, then the gain or loss of *n* avoids *i* during interval *t*. If $R_{tin} > W_{tn}$, then the gain or loss of n targets i during time interval t.

$$R_{tin} = \frac{transition\ area\ from\ category\ i\ to\ n\ during\ interval\ t \times 100}{interval\ t\ duration \times size\ of\ category\ i\ at\ start\ time} = \frac{C_{tin} \times 100}{(Y_{t+1} - Y_t)\sum_{j=1}^{J} C_{tij}} \quad (3.7)$$

$$W_{tn} = \frac{gain\ of\ category\ n\ during\ interval\ t \times 100}{interval\ t\ duration \times size\ of\ non\ category\ n\ at\ start\ time} = \frac{\sum_{i=1}^{J} C_{tin} - C_{tnn} \times 100}{(Y_{t+1} - Y_t)\sum_{j=1}^{J}[(\sum_{i=1}^{J} C_{tij}) - C_{tnj}]} \quad (3.8)$$

To perform the intensity analysis, the "OpenLand" package (Exavier and Zeilhofer, 2020) in R environment was used. The LULC outputs from the four years were used as input data in the "ContingencyTable" function to generate a cross-tabulated matrix comprising the quantity of changes in square kilometre from one category to another between two consecutive time points. This cross-tabulated matrix was utilized as input in the "intensityAnalysis" function to compute the interval, category and transition levels of changes that have occurred between the different categories, during the three-time intervals. Figure 3.4 presents the overall methodological flowchart for LULC mapping in the study area.

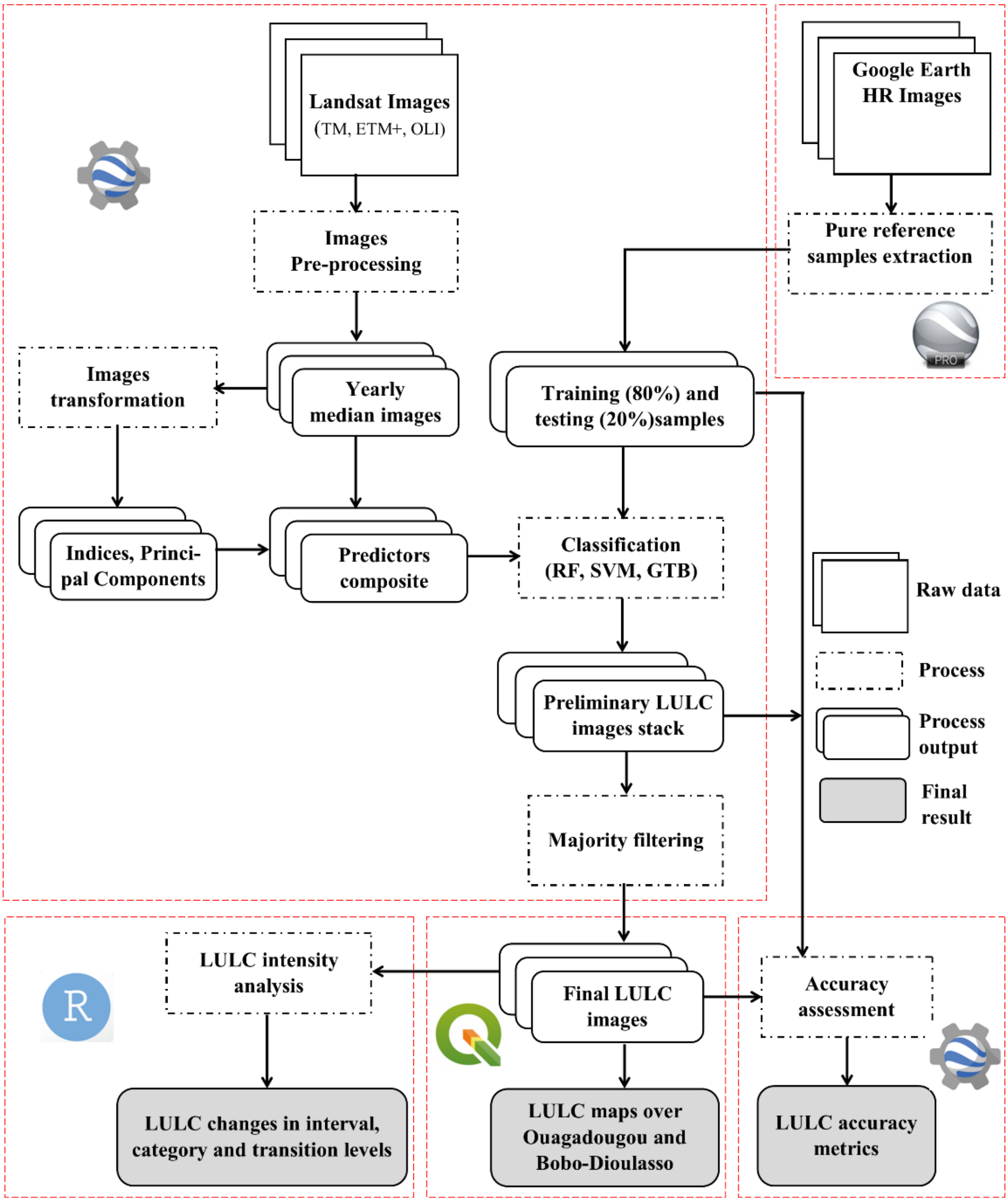

Figure 3.4.: Flowchart of the image classification process

Source: Author's data analysis (2023)

3.3.2. Data analysis for LST and air temperature trend assessment

To assess LST and air temperature trend, the analysis consisted of LST missing data assessment and LST gap-filling. LST and air temperature trend and LST and air temperature relationship were also performed.

3.3.2.1. *LST missing data assessment*

Satellite LST is vital for climatological and environmental studies, but the available dataset are not continuous in time and space due to cloud cover (Shiff *et al.,* 2021). Indeed, MODIS produces daily both daytime and night-time, almost global coverage, LST data at a spatial resolution of 1 km. However, the datasets are often discontinued due mainly to cloud cover. In this research, the daily LST data extracted from MODIS thermal imagery were analysed to detect missing data. The missing values in each dataset from 2003 to 2021 are presented in Figure 3.5.

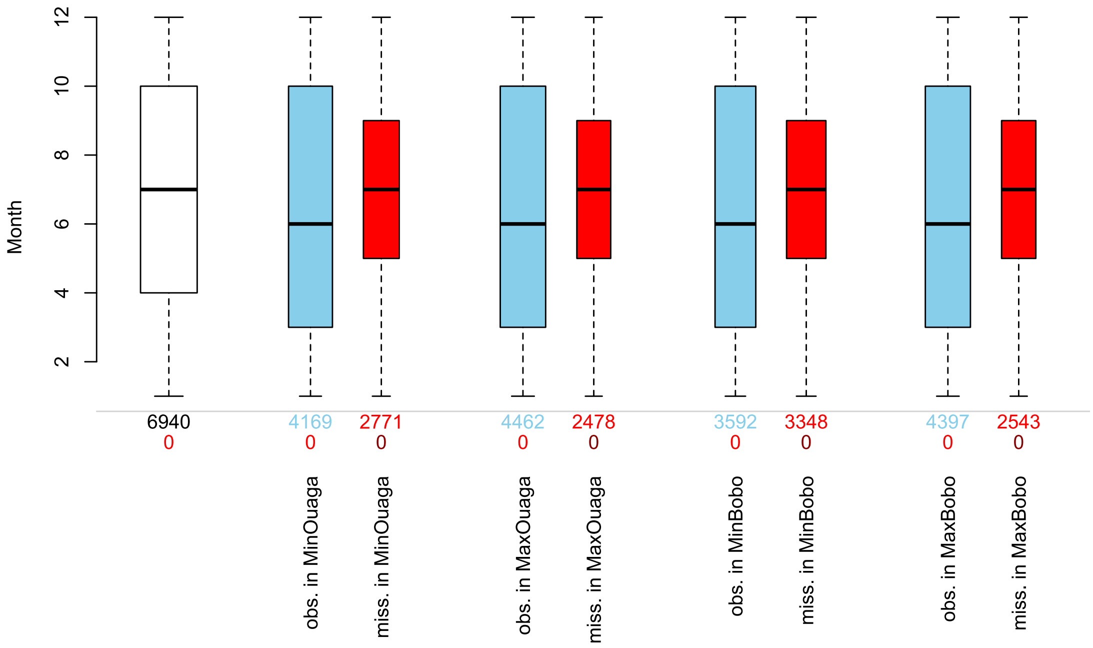

Figure 3.5: **Missing LST Data**

Source: Author's data analysis (2022)

The figure 3.5 shows that over the site of Ouagadougou, there was 36% daytime and 40 % night-time missing LST data. In Bobo-Dioulasso, the missing data was estimated at 37% and 48% during daytime and night-time, respectively. Indeed, these daily missing data over the urban area could alter the quality of monthly, seasonal and yearly average LST computation (Li *et al.,* 2018). For example, there are months with more than five missing daily data, and to include them in the calculation of monthly means, a gap-filling operation was performed to compute the missing data based on the observed daily LST values (Anderson and Gough, 2018).

3.3.2.2. *LST gap-filling*

To fill the data gaps and produce a continuous LST, different interpolation methods including the use of available early observations data or data from nearby pixels to compute LST in pixels with data gaps (Jin and Dickinson, 2000), as well as air temperature to LST relationships (Shiff *et al.,* 2021) were used. For this research, an approach combining the 1-km MODIS LST product with the 0.1°x 0.1° ERA5-Land 2 meters above ground air temperature datasets were used to produce a spatiotemporally continuous gap-filled LST of MODIS at the spatial resolution of 1-km. The method was based on the following considerations: Firstly, daily minimum LST and air temperature values are recorded in early morning while the air temperature peak occurs 1-3 hours after LST maximum at noon (Good, 2016); secondly, LST under cloud coverage is close to 2-m air temperature value; thirdly, LST at a specific time and location involves two components: the long-term mean (climatology) and the deviation from that climatology (anomaly) due to weather conditions (Shiff *et al.,* 2021).

So, a Temporal Fourier Analysis (TFA) was performed on the daytime and night-time existing LST values and the 2 metres above ground air temperature data as well. TFA is a mathematical method that decomposes a time-dependent periodic phenomenon into series of sinusoidal functions, each defined by unique amplitude and phase (Jakubauskas and Legates, 2000). It describes the seasonal cycles of temperature in terms of annual, bi-annual and tri-annual components or harmonics, and the combination of those components is considered as the climatology in the present study. The application of TFA in both temperature variables resulted in LST and air temperature climatology values from 2003 to 2021. Based on the daytime and night-time climatology values, the air temperature anomaly was computed. To proceed to the gap-filling, the cloud free daytime and night-time LST climatology values were added, respectively, to the daytime and night-time air temperature anomalies to generate the daytime and night-time continuous LST values of the study sites, as shown in Equation (3.9) (Shiff *et al.,* 2021).

$$\mathrm{LST}_{under\_cloud} = \mathrm{LST}_{clim} + \mathrm{T}_{anomaly} \tag{3.9}$$

Where $\mathrm{LST}_{under\_cloud}$ is the value of missing LST, LST_{clim} is the climatological clear sky mean LST and $\mathrm{T}_{anomaly}$ is the anomaly value of 2-m air temperature.

To assess the performance of the derived continuous LST model, the commonly used statistical metrics including Root Mean Square Error (RMSE) and Mean Absolute Error (MAE) (Bartkowiak *et al.,* 2019) were calculated with the daytime and night-time cloud free pixel LST values. In addition, Pearson correlation was performed to evaluate the strength of the relationship between the two datasets. Table 3.8 presents the error metrics.

Table 3.8: Error Metrics of MODIS Gap-Filled LST Dataset

	Ouagadougou			**Bobo-Dioulasso**		
	RMSE	**MAE**	**Pearson**	**RMSE**	**MAE**	**Pearson**
LST Day	3.84	2.00	0.83	4.11	2.42	0.84
LST Night	2.23	1.21	0.89	1.38	0.69	0.90

Source: Author’s data analysis (2022)

The RMSE ranges between 1.38 and 4.11, while the MAE fluctuates between 0.69 and 2.42. For the correlation, all the coefficient values are greater than 80 per cent. These values are acceptable, because they are within the validation interval of previous research work which performed models' performance assessment using similar metrics (Kou *et al.,* 2016; Malamiri *et al.,* 2018; Shiff *et al.,* 2021). After validating the computed continuous daytime and night-time LST data, they were used to fill only the missing values in the MODIS LST product, through blending method, to produce a spatio-temporal continuous LST datasets.

3.3.2.3. *LST and air temperature trend analysis*

The trend of air temperature and LST dataset from 2003 to 2021, was computed through the non-parametric Mann-Kendall's trend test. The Mann-Kendall test is one of the most popular non-parametric trend test based on observational ranking and is less sensitive to outliers (Yadav *et al.,* 2014). It is used to analyse time-series data for consistently increasing or decreasing trends detection. It works for all distributions, which means the data need not meet a normal distribution. The purpose was to determine if the temperatures time series exhibited a significant monotonic increasing or decreasing trend, using a threshold (p-value) of 0.05 (95 per cent Confidence Interval).

To perform a trend test in a dataset without any autocorrelation, the levels of serial correlation of the seasonal and yearly time series datasets were investigated. The presence of serial correlation among the datasets was verified visually, using the Auto-Correlation Function (ACF) functions in R environment, which compute the autocorrelation in the dataset. The Bias corrected Prewhitening (bcpw) function from the Modified Versions of Mann-Kendall and Spearman's Rho Trend Tests package (modifiedmk) was applied to the datasets with autocorrelation before running the trend (Patakamuri and O'Brien, 2021). For the yearly and seasonal temperatures trend, the Mann-Kendall Test of Time Series Data Without Modifications (mkttest) function was used (Patakamuri and O'Brien, 2021), because no significant autocorrelation was found within the datasets.

3.3.2.4. *LST and air temperature relationship*

To assess the relationship between the LST and 2-m above ground air temperature two multivariate statistical methods were used. First of all, the datasets were checked to test the normality assumption (Ghasemi and Zahediasl, 2012). The normality test was performed through quantile-comparison plot (Figure 3.6) and Kolmogorov-Smirnov (KS) Test (for more than 5 000 entries).

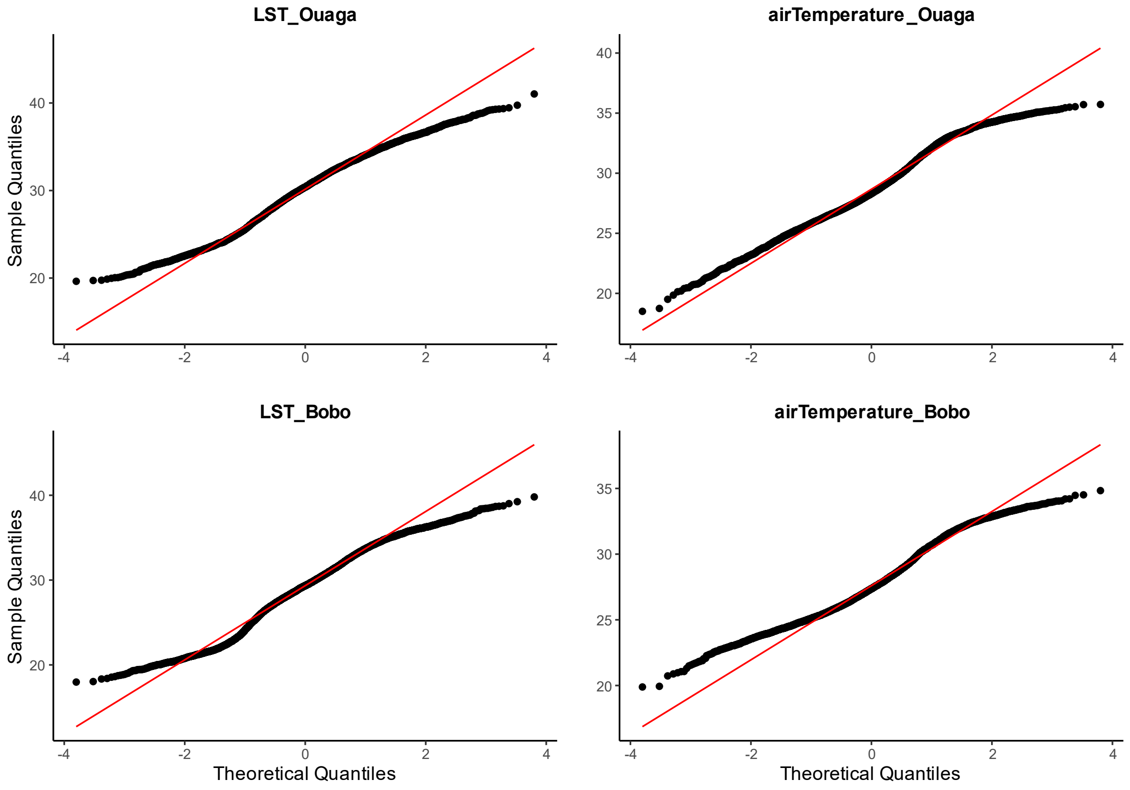

Figure 3.6: **Quantile-Comparison of Temperature Datasets**

Source: Author's data analysis (2023)

The visualisation of the plot indicated a non-normal distribution of the datasets for both cities, because the points do not follow the diagonal reference line. In addition, the p-values of the KS test are greater than the threshold value of 0.05 for both sites, then the datasets do not meet the normal distribution. However, according to the central limit theorem, “sample means are approximately normal for moderately large sample sizes even if the original populations are non-normal” (Elliott and Woodward, 2007). Therefore, with such a large sample size (the dataset has more than 6,000 entries) and given that the dataset is composed of two groups (LST and air temperature) of quantitative variables, a t-Test was performed to compare them in terms of mean values, following a simple conservative approach (in case of unequal variances).

In addition, Spearman correlation was performed to assess the degree of relationship between the two variables. The values are comprised between -1 and +1, indicating a positive correlation when the ranks of the two variables increase at the same time, whereas the correlation is negative when the rank of one variable increases as the other one decreases (Patra *et al.,* 2018). A value of zero or close to zero means no relationship between the two variables.

3.3.2.5. *Estimation of surface urban heat island intensity*

The Surface Urban Heat Island (SUHI) was assessed in this study as the LST difference from the average LST of the whole area. SUHI intensity over the study area was quantified using the Relative surface temperature (T_R) concept (Xu *et al.,* 2013). It is a relative concept calculated by subtracting the average LST value of the whole area from the LST value of each pixel and dividing by the average LST, as shows in Equation (3.10).

$$T_R = \frac{LST_i - LST_a}{LST_a} \tag{3.10}$$

Where, LST_i is the surface temperature value for a pixel i, LST_a is the average surface temperature value of the area.

After the computation of the T_R, the values were grouped into classes and the corresponding SUHI intensities were defined (Table 3.9). Figure 3.7 shows the methodological flowchart for LST and air temperature analysis.

Table 3.9: SUHI Intensity Definition

Relative surface temperature (°C)	**SUHI intensity level**
< 0	Weak heat island
0 – 0.05	Moderate heat island
> 0.05	Strong heat island

Source: Adapted from Xu *et al.* (2013)

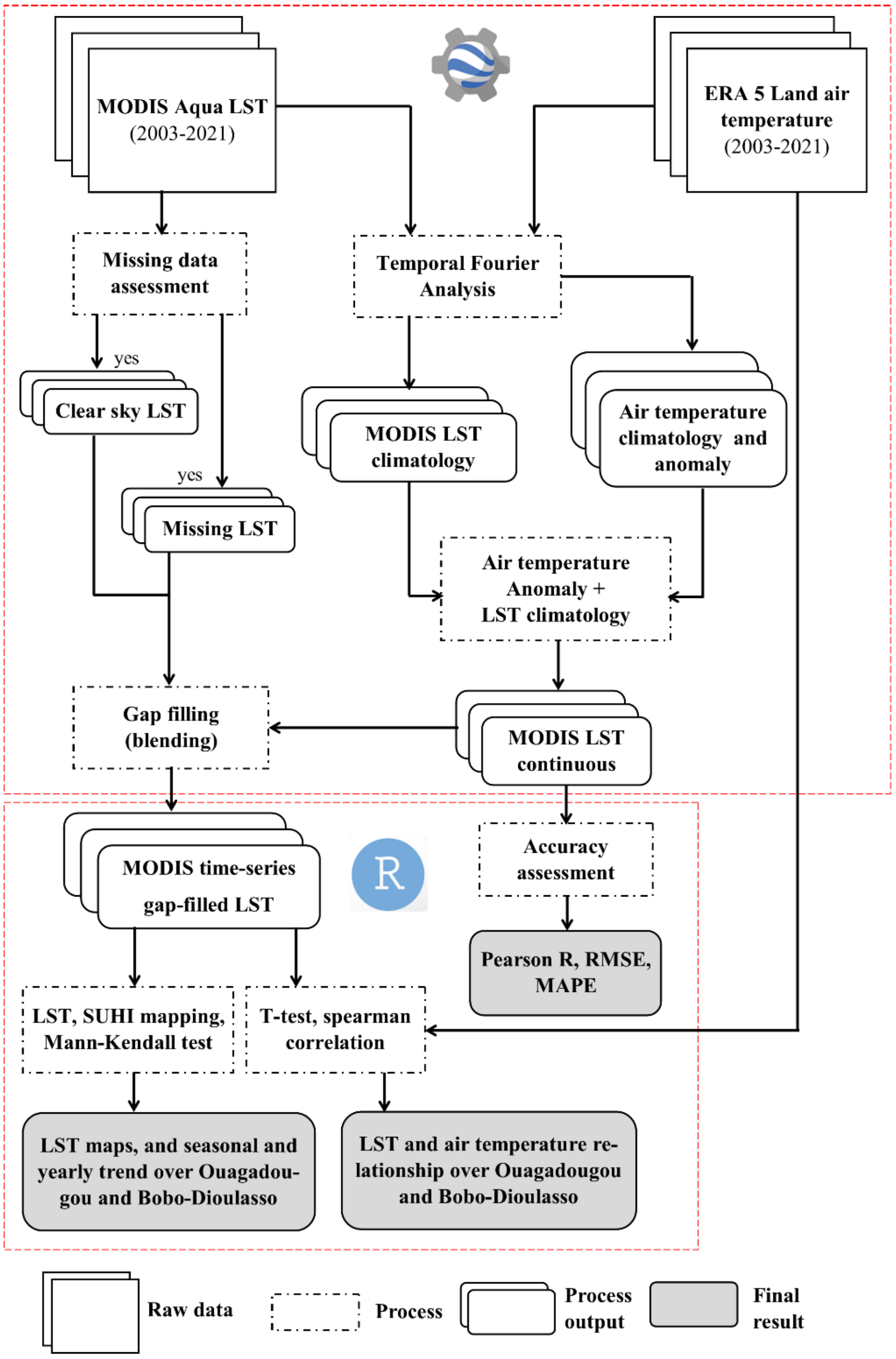

Figure 3.7.: Flowchart for LST and Air Temperature Trend Assessment

Source: Author’s data analysis (2022)

3.3.3. Data analysis for LULC and LST relationship

A fractional cover analysis was done, using the "aggregate" function in R to extract the proportion of each LULC class per pixel for the assessment of the relationship between the LULC dynamics and LST trend. Indeed, the algorithm takes a classified high-resolution image (LULC from Landsat images), downscales it and calculates the fraction of a given land cover class within each coarse pixel. To perform that analysis, the LULC maps for 2003, 2009, 2015 and 2021 were reclassified to have two homogeneous classes: built area and non-built area (Table 3.10). The objective is to evaluate the implication of human footprint (built-up areas) in LST intensification and the contribution of natural areas (non-built-up) to lower the LST values in urban settings.

Table 3.10: **Reclassified Homogeneous LULC Classes**

LULC classes	Reclassified
Built-up Bare land	Built-up
Forest Agricultural land Water	Non-built-up

Source: Author's data analysis (2022)

The spatial resolution of the LULC images was set to 900 metres instead of 1,000 metres as the LST images because the aggregate function accepts integer multiple factors (a factor of 30 was applied). The aggregate function was used in the R environment to calculate the proportion of each LULC class within 900×900 square metres pixels. After the computation of the proportions, the LULC datasets were stacked with the LST images. In addition, a grid layer of 900×900 square metres was created. Using the stacked layer together with the grid layer, the built and non-built cover ratio and the equivalent LST values per pixel were extracted through the "Zonal statistics" tool in QGIS. The coverage rates were then grouped into 5 classes (0 per cent -20 per cent, 20-40 per cent, 40-60 per cent, 60 per cent -80 per cent, and 80 per cent -100 per cent) to examine the LST patterns.

Furthermore, statistical analyses comprising median differences and Pearson correlation were performed to show the correlation between the LST and the different LULC rates, and the cooling effects of non-built surfaces. Indeed, to show the impact of non-built pixels on urban cooling, the median LST value of each of the five non-built coverage classes (0 per cent -20 per cent, 20 per cent -40 per cent, 40 per cent -60 per cent, 60 per cent -80 per cent, and 80 per cent -100 per cent) was subtracted from the median LST value of the fully built-up pixels (Alavipanah *et al.,* 2015). The higher the median difference, the higher the cooling effect of the concerned non-built cover rate. The methodological flowchart for assessing the relationship between LULC and LST is presented in Figure 3.8.

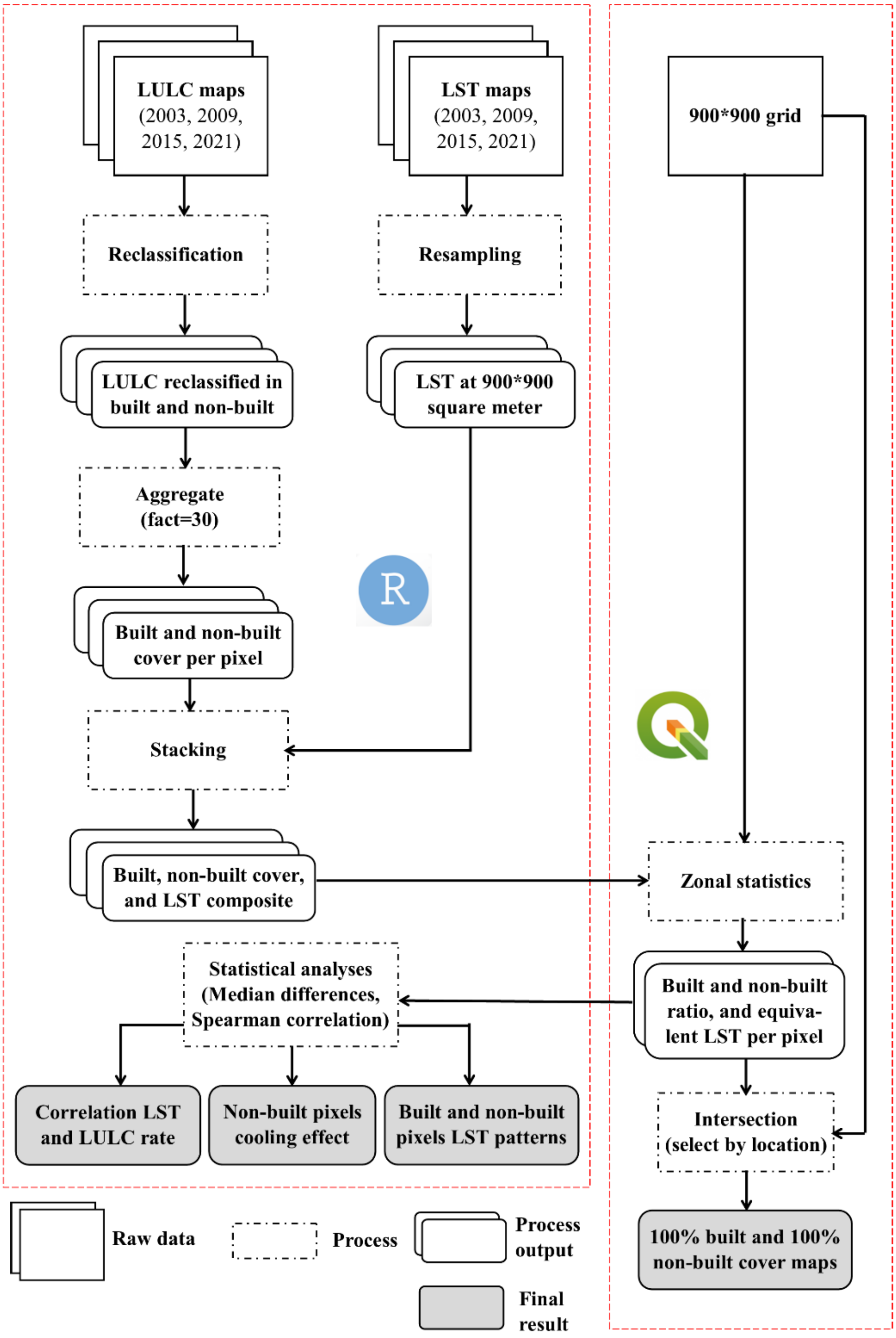

Figure 3.8: Flowchart for LULC and LST Relationship Assessment

Source: Author’s data analysis (2022)

3.3.4. Data analysis for LST and diseases relationship

The derived LST data and the reported cases of selected temperature-related diseases, including *Plasmodium falciparum* malaria, dengue fever and meningitis, collected from the Ministry of Health at district level were used. The choice of the diseases is motivated by the fact that in the literature, investigations were only made on the link between the air temperature and diseases such as *Plasmodium falciparum* malaria (Chastel, 2006; Gething *et al.,* 2010; Millogo *et al.,* 2022), dengue (Chastel, 2006) and meningitis (Chen *et al.,* 2022).

Moreover, these diseases are all considered as potential epidemic diseases under monitoring in the National health system of Burkina Faso (Ministère de la santé, 2012). The urban area in the two cities were considered for the analyses because the statistical datasets on the diseases were full of gaps, particularly concerning the peripheral areas. The urban areas were divided into 5 and 3 zones respectively for Ouagadougou and Bobo-Dioulasso in line with the spatial coverage (district level) of the data received. Later on, "Zonal statistics" tool was employed in QGIS software to extract the average annual Land Surface Temperature values for each zone.

The generated mean LST values were used with the reported case statistics for each disease to perform a correlation analysis in R environment applying Spearman method, which is a non-parametric method, because the data did not follow a normal distribution. Figure 3.9 presents the flowchart for assessing the relationship between LST and diseases.

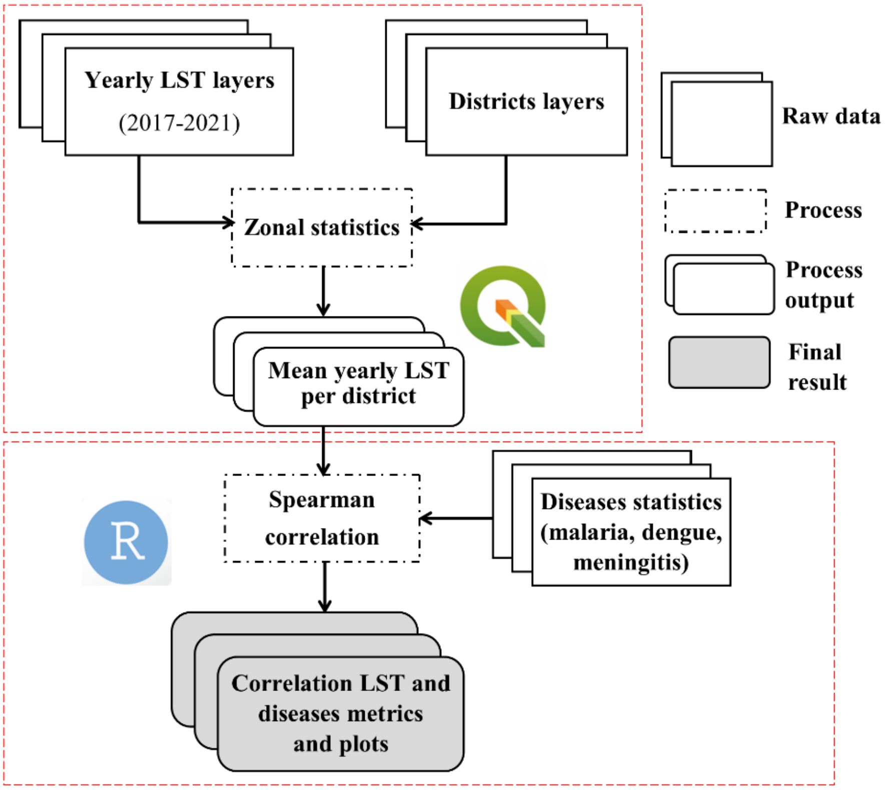

Figure 3.9: Flowchart for LST and Diseases Relationship Assessment

Source: Author's data analysis (2022)

3.3.5. Data analysis for future LULC and LST prediction

3.3.5.1. *Future LULC prediction*

The future prediction of LULC was performed using Land Change Modeler (LCM), an integrated software embedded in TerrSet package (Eastman, 2020b). LULC simulation in LCM follows an empirical stepwise process including change analysis, transition potential modelling, and prediction (Eastman, 2020b). The process is based on the historical changes between time 1 (t1=2009) and time 2 (t2=2015) to predict the future LULC in both cities. The change analyses showed that anthropogenic actions are increasing in both studied cities, through the development of built-up areas. To comprehend the patterns of change in the area, the spatial trend tool in LCM was used to produce trend maps following a 9th order polynomial function (Eastman, 2020b).

LULC future prediction needs to consider independent variables (earliest and latest images) and some main driver variables. The common driver' variables used in LULC simulation in LCM included distance from river, distance from road, distance from urban (settlement area), elevation, slope (Mungai *et al.,* 2022) and evidence likelihood (Yangouliba *et al.,* 2022). Table 3.11 describes the contribution of the driver' variables.

Table 3.11: **LULC Change Drivers**

Variable	Description
Elevation	Physical constraint to LULC change
Slope	Physical constraint to LULC change
Distance from rivers	Dynamic variable that provides convenience to access resources while changing LULC
Distance from roads	Dynamic variable that expresses accessibility and drives urban expansion
Distance from urban	The closer the land to an existing settlement area, the easier it is for that land to change to built-up surface
Evidence likelihood	Expresses the likelihood of finding change between built-up and all other LULC class in a pixel

Source: Adapted from Leta *et al.* (2021) and Girma *et al.* (2022)

LCM has a set of models for predicting LULC potential transitions based on the driver variables and the independent LULC maps. The most common used is the Multi-Layer-Perceptron Neural Network (MLP-NN) (Mungai *et al.,* 2022). For this study, the MLP-NN was used because of its ability to model many non-linear transitions' potential at once (Eastman, 2020a). This model also showed good performance in predicting future LULC in the region (Yangouliba *et al.,* 2022). Based on the selected driver variables and the major LULC transition between 2009 and 2015, the model was trained to simulate the LULC maps for 2021 in order to assess the model's ability to predict future LULC in the study area. Thus, the agreement between the simulated and classified LULC maps of 2021 were evaluated through the VALIDATE module in IDRISI GIS Analysis. The validation metrics used were the k statistics including the overall accuracy (K_{no}) and the model's ability to identify correct locations ($K_{locality}$) (Sibanda and Ahmed, 2020).

To predict future LULC in the study area, the Business As Usual (BAU) scenario was used within a Markov Chain model. This scenario is the one that follows the normal course of land use activity in the area and involves predicting what the landscape would look like in 2027 and 2050 if the nature of urban development remains unrestricted, dominated by the development of built-up surface at the expense of natural areas. 2027 is the following year based on the six years epoch as considered in historical LULC analysis, while and 2050 corresponds to the target year for reaching global net zero CO_2 emission to limit the warming level to 1.5°C (IPCC, 2023). Figure 3.10 presents the flowchart for future LULC prediction.

3.3.5.2. *Future LST prediction*

The correlation analyses performed between LST and built-up rate and LST and non-built-up rate in Objective 3 showed that the two variables had a strong linear relationship with LST. A Multiple Linear Regression (MLR) model was then built using the historical LST and LULC data for the years 2009 and 20015 as shown by Equation (3.11) (Estoque and Murayama, 2017; Sekertekin and Zadbagher, 2021). In order to evaluate the model accuracy, for predicting future LST, LST maps of 2021 was simulated and compared with the initial LST maps of 2021, using Kappa Index of Agreement.

$$LST = a_0 + a_1 \times built\_up + a_2 \times non\_built\_up + e \qquad (3.11)$$

Where LST corresponds to the LST value of a pixel, a_0 is the intercept of the regression line, a_1 is the regression coefficient of built-up, a_2 is the regression coefficient of non-built-up and e is the residual standard error. Afterwards, the predicted LULC maps of

2027 and 2050 were reclassified into two classes namely built-up and non-built-up. The proportion of each class per pixel of 900 × 900 square metres was also calculated. The LST maps for 2027 and 2050 were then predicted using the MLR model with the independent variables being built-up and non-built-up rate of the respective years (Figure 3.10).

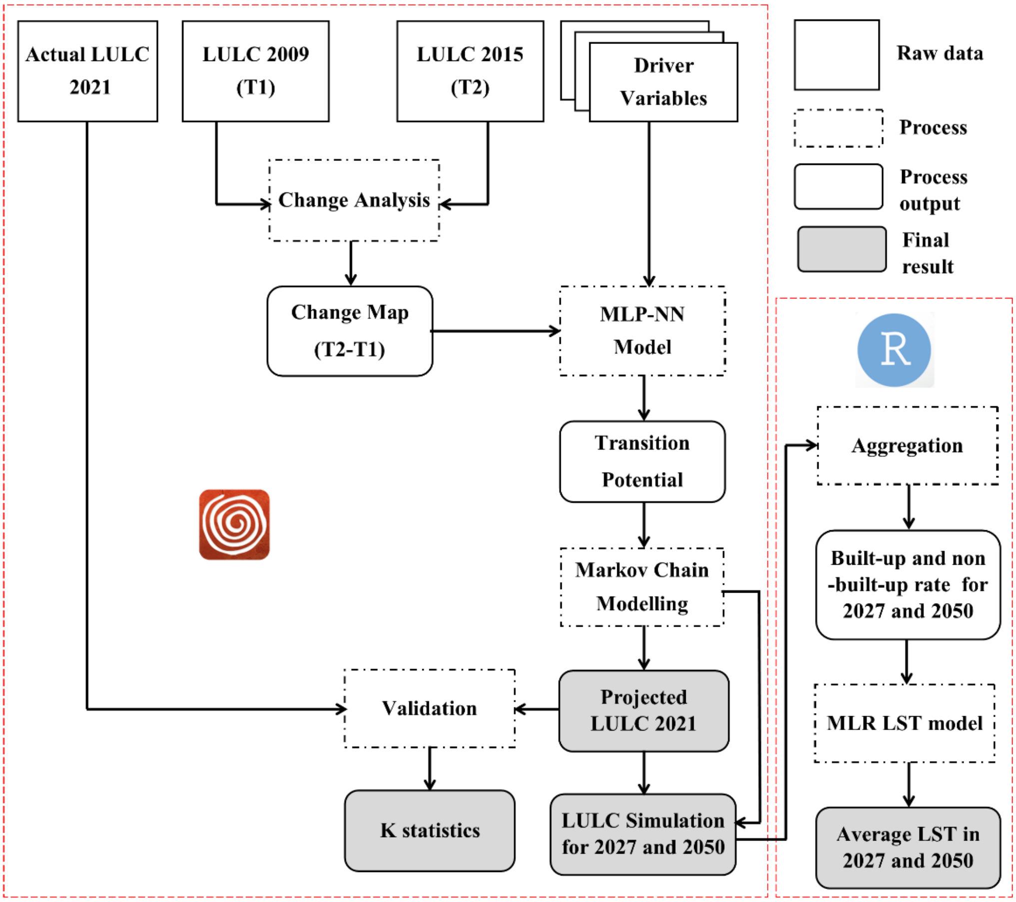

Figure 3.10: Flowchart for Future LULC and LST Prediction

Source: Author’s data analysis (2023)

CHAPTER FOUR

4.0. RESULTS AND DISCUSSION

4.1. Results

The results section is composed of five subsections based on the objectives of the study. It presents firstly the results of the LULC dynamics assessment in Ouagadougou and Bobo-Dioulasso. Secondly, the findings on the LST and air temperature trend analysis across the study area are presented. Thirdly, the results on the correlation between LST and urban LULC changes are presented. The fourth subsection presents and analyses the results on the relationship between the distribution of LST and the prevalence of temperature-related diseases in the two cities. The last subsection presents the findings related to the future predictions of LULC changes and LST in the study area.

4.1.1. Land use/land cover dynamics assessment

4.1.1.1. *Land use/land cover spatial distribution*

The LULC maps of Ouagadougou (Figures 4.1) show that the dominant classes are agricultural land and built-up area. There was a continuous expansion of settlement areas from the inner city towards the peripheral areas at the expense of other land uses such as agricultural areas. Being the two main land use classes in the area, they have a negative correlation in terms of spatial growth. While built-up is expanding in the area, agricultural lands are decreasing, indicating the intensification of human footprint throughout the years. Other LULC classes such as water bodies, forest and bare land were also present in the maps. In Bobo-Dioulasso, agricultural land, forest and built areas are the most represented (Figure 4.2). Like Ouagadougou, the settlement areas in Bobo-Dioulasso kept growing, at the expense of natural landscape such as forest areas. The expansion of built-up areas towards the northern part of Bobo-Dioulasso's city is due to the development of a new estate, named “Bobo 2010”, beginning from year 2007. The water bodies and bare land areas occupy small surfaces in the maps.

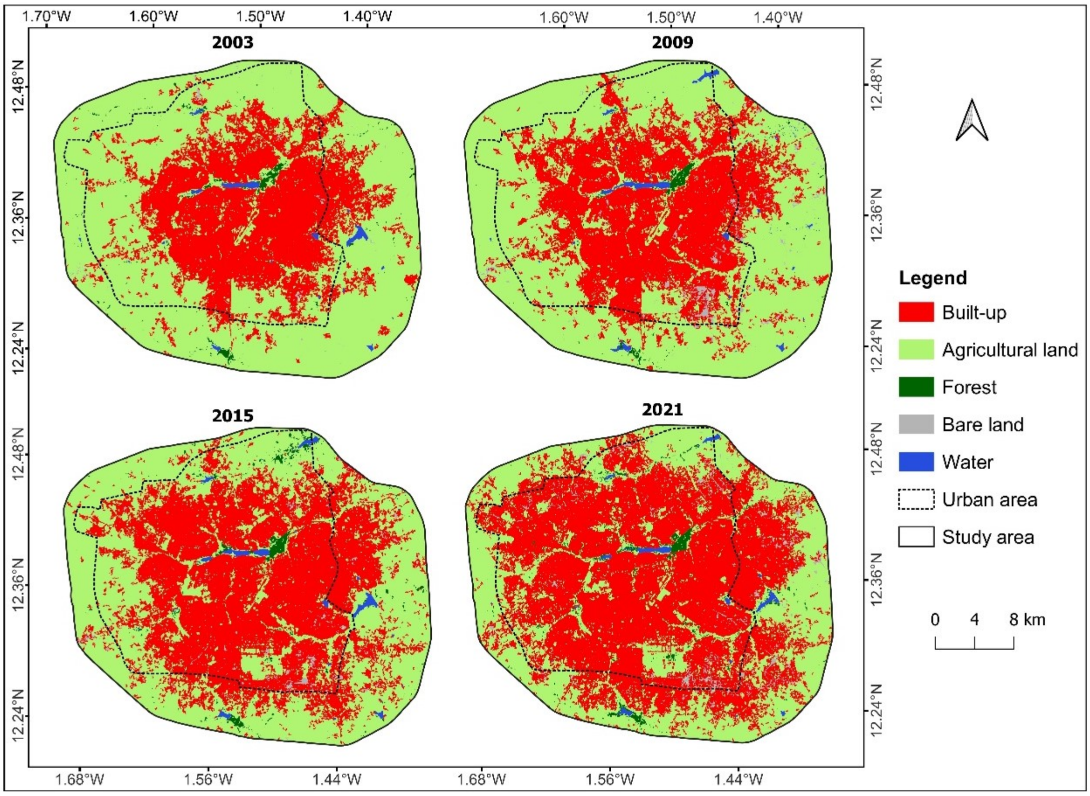

Figure 4.1: LULC Distribution in Ouagadougou

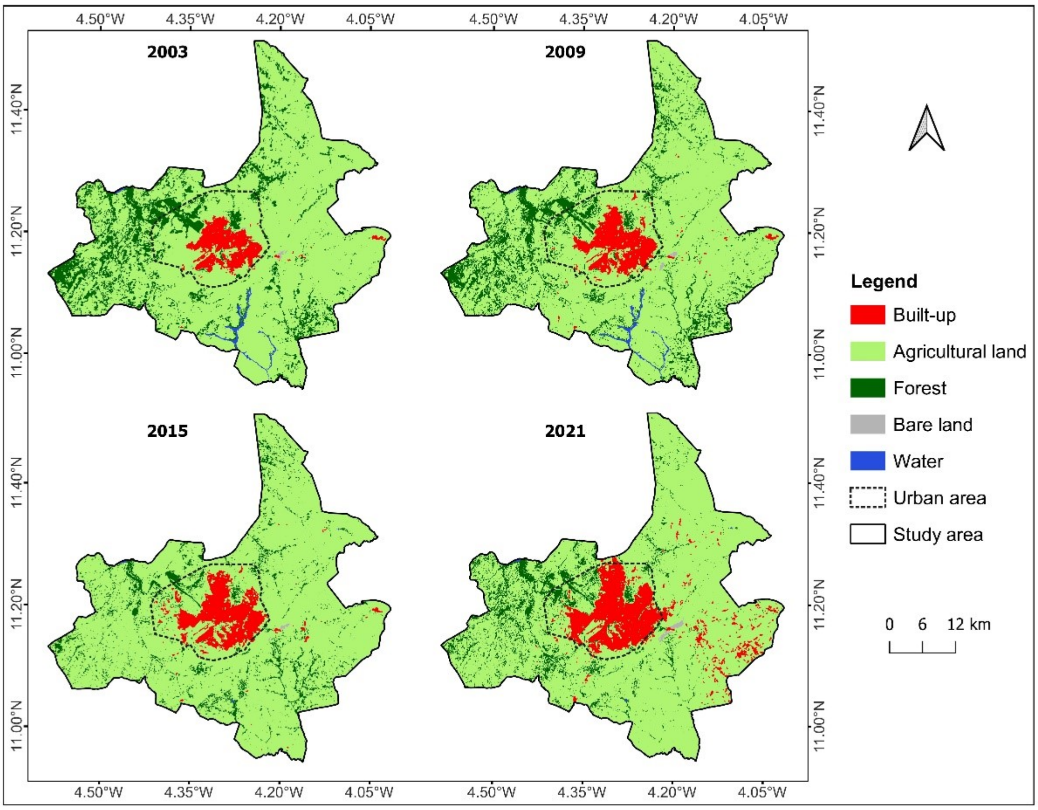

Figure 4.2: LULC Distribution in Bobo-Dioulasso

4.1.1.2. *Land use/land cover classification accuracy*

The accuracies of the classified LULC images were assessed using the overall accuracy and the kappa coefficient. The individual classifications overall accuracy varied between 0.8 and 0.94 performed by the Random Forest (RF) classifier, respectively in 2021 and 2003 in Ouagadougou. In Bobo-Dioulasso, the minimum accuracy was achieved by RF in 2015 (0.66) while the maximum was performed by the Support Vector Machine (SVM) classifier in 2003 (0.77). The majority voting results showed smoothed overall accuracies and kappa coefficients for all the years in Ouagadougou (Table 4.1). However, there is an improvement for both metrics, compared to the results of all the individual classifiers, for year 2009. For Bobo-Dioulasso, the majority filtered images presented stable (2009 and 2015) to totally improved values (2003 and 2021) compared to the individual classifiers for the overall accuracy and the kappa coefficient (Table 4.2).

Table 4.1: LULC Accuracy Metrics in Ouagadougou

Year	RF	GTB	SVM	Majority	RF	GTB	SVM	Majority
	Overall Accuracy				kappa coefficient			
2003	0.94	0.89	0.82	0.87	0.9	0.81	0.69	0.79
2009	0.81	0.8	0.85	0.87	0.68	0.66	0.74	0.79
2015	0.85	0.87	0.85	0.85	0.74	0.77	0.75	0.77
2021	0.8	0.83	0.92	0.82	0.66	0.72	0.87	0.72

Source: Author's data analysis (2023)

Table 4.2: LULC Accuracy Metrics in Bobo-Dioulasso

Year	RF	GTB	SVM	Majority	RF	GTB	SVM	Majority
	Overall Accuracy				kappa coefficient			
2003	0.66	0.71	0.77	0.81	0.52	0.6	0.7	0.75
2009	0.74	0.71	0.74	0.74	0.63	0.58	0.64	0.64
2015	0.66	0.74	0.74	0.74	0.52	0.64	0.63	0.64
2021	0.71	0.78	0.71	0.85	0.57	0.69	0.59	0.79

Source: Author's data analysis (2023)

4.1.1.3. *Land Use/Land Cover trend*

The landscape units have changed in different ways in Ouagadougou and Bobo-Dioulasso, between 2003 and 2021. In Ouagadougou, the built area occupied 32.75 per cent, 35.95 per cent, 46.86 per cent and 58.34 per cent of the total landscape for 2003, 2009, 2015 and 2021 respectively (Table 4.3). Conversely, the agricultural land areas experienced a decreasing trend represented by 65.45 per cent, 60.86 per cent, 50.13 per cent and 37.80 per cent of the area for 2003, 2009, 2015 and 2021 respectively. These figures indicate a linear increase of 78.13 per cent for built area against a decrease of 42.25 per cent in agricultural land between 2003 and 2021. The forest areas experienced a global increase of 55.56 per cent, while the water bodies increased by 2.84 per cent due to the construction of a new dam in the northern part of Ouagadougou in 2007. Bare land surfaces also increased and occupied more than 19 per cent of the area in 2021.

Table 4.3: Proportion of LULC Classes in Ouagadougou (% of the total area)

LULC class	2003	2009	2015	2021
Built	32.75	35.95	46.86	58.34
Agricultural land	65.45	60.86	50.13	37.80
Forest	0.81	0.67	1.22	1.26
Bare	0.39	1.71	0.98	1.98
Water	0.60	0.81	0.81	0.62

Source: Author’s data analysis (2023)

In Bobo-Dioulasso, like Ouagadougou, the built areas continuously increased during the study time span. The built-up areas represented 4.10 per cent, 5.19 per cent, 6.36 per cent and 9.86 per cent of the total area for 2003, 2009, 2015 and 2021 respectively (Table 4.4), corresponding to a variation of +140.7 per cent during the study period. Unlike Ouagadougou, the trend of agricultural lands was not linear in Bobo-Dioulasso. While there was a gradual and consistent growth between 2003 and 2015 represented by 79.59

per cent (2003), to 79.85 per cent (2009) and 84.99 per cent (2015), a decline to 80.69 per cent was recorded for 2021. The decrease of agricultural land in 2021 could be due to the 0.68 per cent increase of forest area after a continuous decline from 15.58 per cent (2003) to 8.51 per cent (2015). The bare land had a global increase, whereas the water bodies decreased across the study period.

Table 4.4: Proportion of LULC Classes in Bob-Dioulasso (% of the total area)

LULC class	**2003**	**2009**	**2015**	**2021**
Built	4.10	5.19	6.37	9.87
Agricultural land	79.59	79.85	84.99	80.69
Forest	15.58	14.25	8.51	9.19
Bare	0.11	0.10	0.07	0.19
Water	0.62	0.62	0.06	0.06

Source: Author’s data analysis (2023)

Figure 4.3 presents the evolution of LULC classes in the cities between 2003 and 2021. The figure shows a rapid expansion of built-up surfaces in Ouagadougou. The built-up expansion rate varied from 0.53 between 2003 and 2009 to 1.82 between 2009 and 2015 and achieved 1.91 between 2015 and 2021. In Bobo-Dioulasso, the same trend applies but at a slower pace compared to Ouagadougou. The expansion rate fluctuated from 0.18 to 0.2 and 0.58 between 2003 and 2009, 2009 and 2015 and 2015 and 2021, respectively.

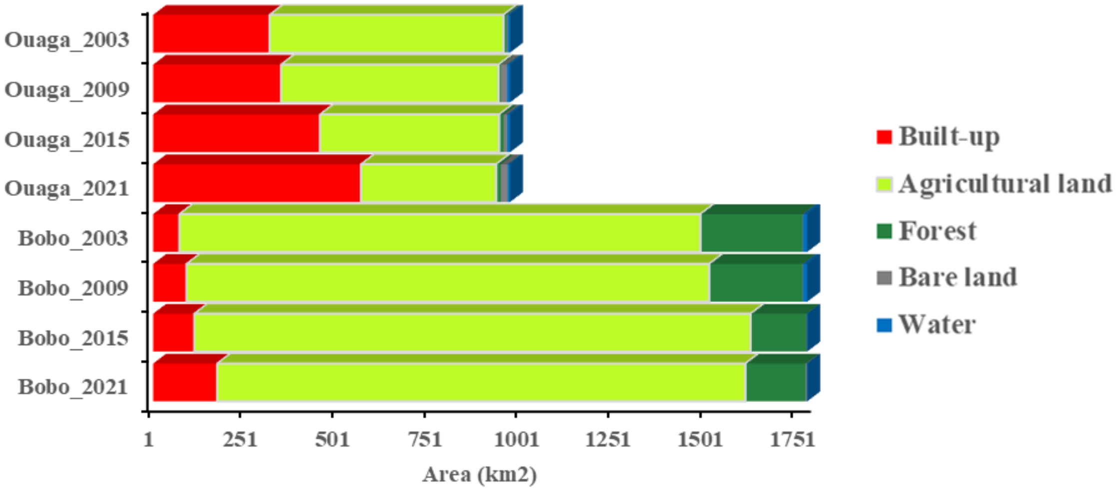

Figure 4.3: Land Use/Land Cover Evolution Between 2003 and 2021

4.1.1.4. *Land use/land cover intensity analysis*

The generated LULC maps for the years 2003, 2009, 2015 and 2021 were overlayed to create a transition matrix for each time interval. The matrices present the rates of change/conversion between the different LULC categories as a percentage of the total area. The diagonal entries represent persistence values of classes, while the off-diagonal entries indicate changes from one class to another. The last row represents the gross gains per category at the final year, while the last column indicates the gross loss for each category at the final year. Table 4.5 presents the transition matrix for Ouagadougou.

Table 4.5: Transition Matrices in Ouagadougou (% of total area)

				2009				
		Agricultural	Bare	Built	Forest	Water	Initial total	Overall loss
2003	Agricultural	55.80	0.61	8.48	0.23	0.33	65.45	9.64
	Bare	0.05	0.18	0.16	0.00	0.00	0.39	0.21
	Built	4.47	0.93	27.29	0.00	0.06	32.75	5.46
	Forest	0.34	0.00	0.01	0.44	0.03	0.81	0.37
	Water	0.20	0.00	0.01	0.00	0.40	0.60	0.20
	Final Total	60.86	1.71	35.95	0.67	0.81	100.00	
	Overall gain	5.06	1.54	8.66	0.23	0.41		15.90
				2015				
		Agricultural	Bare	Built	Forest	Water	Initial total	Overall loss
2009	Agricultural	47.23	0.16	12.55	0.69	0.23	60.86	13.63
	Bare	0.19	0.50	1.02	0.00	0.00	1.71	1.21
	Built	2.43	0.32	33.19	0.00	0.01	35.95	2.76
	Forest	0.15	0.00	0.02	0.49	0.02	0.67	0.18
	Water	0.14	0.00	0.09	0.03	0.55	0.81	0.26
	Final Total	50.13	0.98	46.86	1.22	0.81	100.00	
	Overall gain	2.90	0.48	13.68	0.73	0.26		18.05
				2021				
		Agricultural	Bare	Built	Forest	Water	Initial total	Overall loss
2015	Agricultural	34.22	0.28	15.07	0.55	0.02	50.13	15.91
	Bare	0.05	0.33	0.59	0.00	0.00	0.98	0.64
	Built	2.82	1.37	42.62	0.04	0.02	46.86	4.25
	Forest	0.56	0.00	0.03	0.61	0.01	1.22	0.61
	Water	0.14	0.00	0.04	0.06	0.57	0.81	0.23
	Total	37.80	1.98	58.34	1.26	0.62	100.00	
	Overall gain	3.58	1.65	15.73	0.65	0.05		21.64

Source: Author’s data analysis (2023)

The major transitions observed in Ouagadougou were from agricultural land to built-up, during the three periods. The rate of conversion of agricultural land to built-up area was higher between 2003 and 2009 (4.47 per cent of the landscape) and relatively low during the other two periods. The conversion of built-up areas to agricultural lands, shown in the matrices, could be explained by misclassification errors.

As for Bobo-Dioulasso, the major transitions were from agricultural to forest areas (Table 4.6). The results show that 6.24 per cent of the total landscape was converted to forest land from 2003 to 2009, 8.23 per cent from 2009 to 2015, and 3.95 per cent from 2015 to 2021.

Table 4.6: **Transition Matrices in Bobo-Dioulasso (% of total area)**

		2009						
		Agricultural	Bare	Built	Forest	Water	Initial total	Overall loss
2003	Agricultural	73.27	0.05	1.36	4.91	0.00	79.59	6.32
	Bare	0.05	0.03	0.03	0.00	0.00	0.11	0.08
	Built	0.30	0.01	3.79	0.00	0.00	4.10	0.31
	Forest	6.23	0.00	0.01	9.34	0.00	15.58	6.24
	Water	0.00	0.00	0.00	0.00	0.62	0.62	0.00
	Final Total	79.85	0.10	5.19	14.25	0.62	100.00	
	Overall gain	6.58	0.06	1.40	4.91	0.00		12.95
		2015						
		Agricultural	Bare	Built	Forest	Water	Initial total	Overall loss
2009	Agricultural	75.88	0.03	1.61	2.32	0.01	79.84	3.96
	Bare	0.05	0.03	0.01	0.00	0.00	0.10	0.06
	Built	0.44	0.00	4.74	0.00	0.00	5.19	0.45
	Forest	8.23	0.00	0.01	6.00	0.02	14.25	8.25
	Water	0.39	0.00	0.00	0.20	0.03	0.62	0.59
	Final Total	84.99	0.07	6.36	8.51	0.06	100.00	
	Overall gain	9.11	0.04	1.62	2.52	0.03		13.31
		2021						
		Agricultural	Bare	Built	Forest	Water	Initial total	Overall loss
2015	Agricultural	76.47	0.12	3.77	4.63	0.00	84.99	8.52
	Bare	0.01	0.06	0.00	0.00	0.00	0.07	0.01
	Built	0.27	0.01	6.08	0.00	0.00	6.36	0.28
	Forest	3.94	0.00	0.01	4.56	0.00	8.51	3.95
	Water	0.00	0.00	0.00	0.00	0.06	0.06	0.00
	Final Total	80.69	0.19	9.86	9.19	0.06	100.00	
	Overall gain	4.22	0.13	3.78	4.63	0.00		12.76

Source: Author's data analysis (2023)

a. Interval level

Figure 4.4 presents the graphical representation of the interval level analysis results, which compare annual changes in intensity for all the area within each time interval.

A fast annual change in intensity was recorded in Ouagadougou between 2015 and 2021 (3.61 per cent per year against 3.09 per cent as uniform intensity), while in Bobo-Dioulasso it was fast between 2009 and 2015 (2.22 per cent, compared to a uniform intensity of 2.17 per cent). During the two other time periods, 2003-2009 and 2009 - 2015 for Ouagadougou, and 2003 - 2009 and 2015 - 2021 for Bobo-Dioulasso, the annual intensity of change was slow.

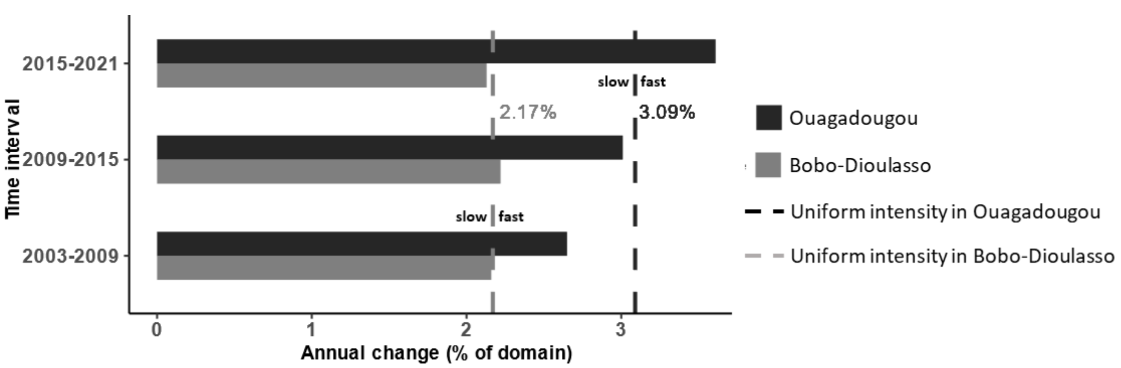

Figure 4.4: **Interval Level Changes of Land Use/Land Cover Categories.**

b. Category level

The category level analysis plots present the size and annual intensity of change of each category's gain relative to the size of the category at the interval's end time point. It also shows the size and annual intensity of each category's loss in relation to the size of the category at the interval's initial time point. The dotted vertical lines represent the uniform intensity rate, which provides information on the patterns of each category if the changes were uniform, for every time interval.

Figures 4.5a and 4.5b present the graphical outputs of category analysis for each time interval in Ouagadougou. Built-up class was the largest gainer for all the time intervals, followed by bare and agricultural lands. The gain for built-up area increased continuously, from 8.6 per cent in 2003 - 2009, 13.68 per cent in 2009 - 2015 to achieve 15.73 per cent of the total landscape in 2015 - 2021. As for the annual change intensity, the uniform intensity (S_t) values indicated an intensification of change from 2003 - 2009 (2.65 per cent) to 2015 - 2021 (3.61 per cent). Bare land, forest and built-up had active changes during the three-time intervals, with bare land having the most active gain ($G_{tj} > S_t$) in 2003 - 2009 and 2015-2021, while forest gain was very active between 2009 and 2015 and 2015 and 2021. Water class showed active gain between 2003 and 2009 and 2009 and 2015. Concerning agricultural category, the gain intensity was dormant ($G_{tj} < S_t$) throughout the study period.

In terms of loss in Ouagadougou, agricultural land had the largest loss in terms of area during the three-time intervals, followed by built-up and bare lands. Agricultural land loss consistently increased from 9.64 per cent in 2003 – 2009 to 13.63 per cent in 2009 - 2015 and 15.91 per cent in 2015 - 2021. The active loss rates were recorded by agricultural, forest, bare land and water during 2009 - 2015 and 2015 - 2021. Built-up class was dormant, except in 2003 - 2009, where it showed a marginal loss in favour of bare land. Looking at the behaviour of each bar regarding the uniform rate, it emerged that less than half of the bar length for agricultural lands in 2009 - 2015 and 2015 - 2021 extend beyond the uniform rate, showing that the large size of area occupied by agricultural land in 2009 and 2015 is the cause of its large loss. In the period 2003 - 2009, more than 50 per cent of forest and water bar lengths exceed the uniform rate, indicating that active change intensity is the reason explaining the two categories' loss sizes. In each time interval, more than half of the bare land went beyond the uniform line, indicating that active intensity is more important than the size of bare land at the start time to explain the size of bare land's loss.

Figures 4.5c and 4.5d show the category level analysis plots in term of size and intensity of change for Bobo-Dioulasso. The larger gainers, in size, were respectively agriculture, forest and built-up during the three periods. The gains in agricultural land increased from

2003 (6.58 per cent) to 2015 (9.11 per cent) and decreased in 2021 (4.22 per cent) at the expense of forest area, which nearly doubled its gain compared to 2015 (2.52 per cent to 4.63 per cent). Built-up surface gains increased regularly during the different time intervals, going from 1.4 per cent in 2003 - 2009 to 1.62 per cent in 2009 - 2015 and 3.78 per cent in 2015 - 2021. The uniform rate showed a quasi-stationary change's intensity during the different time intervals. As for the gain intensity, bare land, forest, and built-up areas experienced the most active changes ($G_{tj} > S_t$). Agricultural change was dormant throughout the study period. In terms of loss, agricultural and forest areas were the larger losers. The intensity of loss for the forest category was active during the three periods. Bare land also experienced active loss during 2009 - 2015 and 2015 - 2021. The large loss in forest and bare areas could be explained by the very active change intensity because more than 50 per cent of the bar lengths exceed the uniform intensity rate.

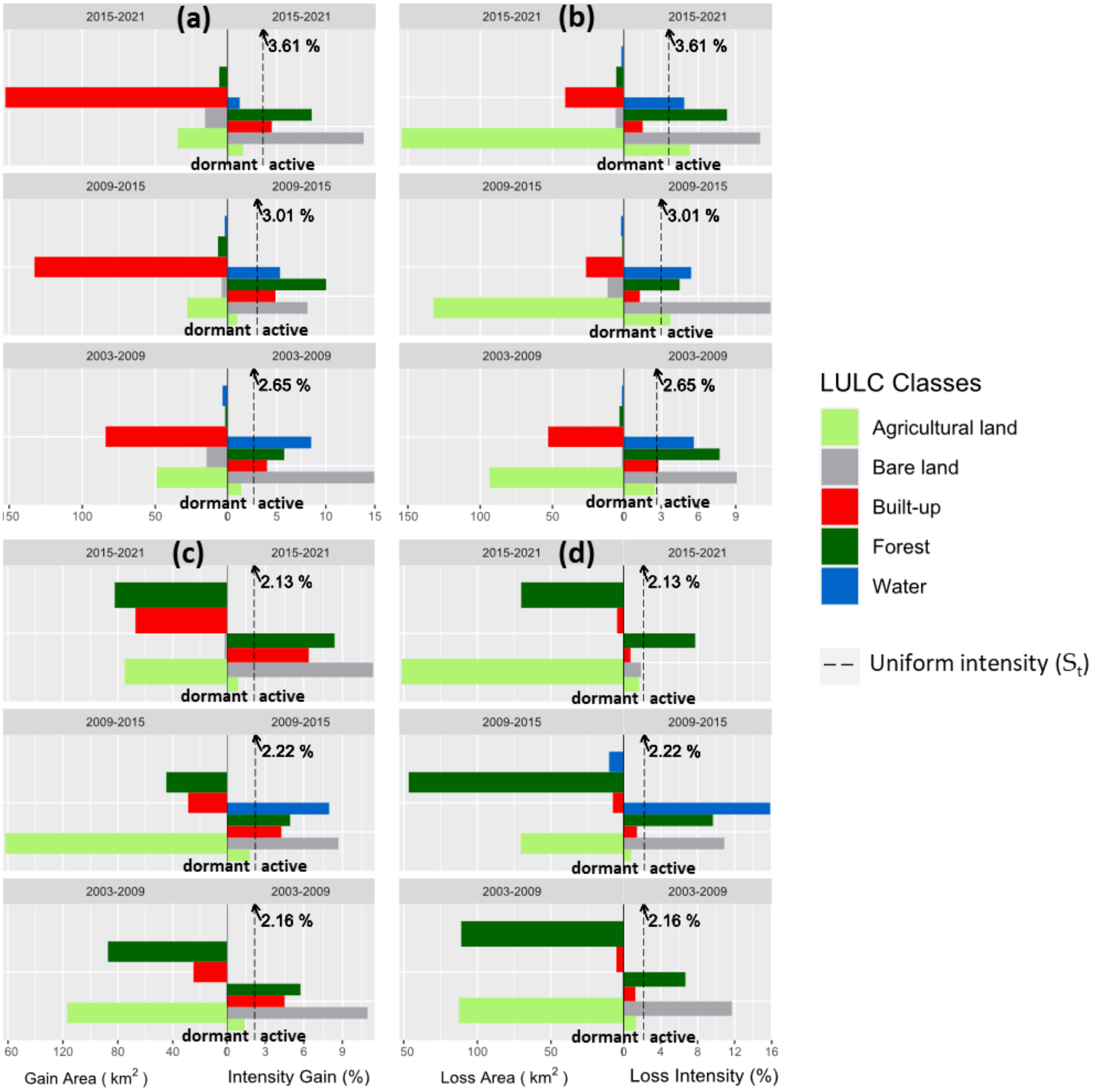

Figure 4.5: Category Level Changes of Land Use/Land Cover: (a) Gain in Ouagadougou, (b) Loss in Ouagadougou, (c) Gain in Bobo-Dioulasso, (d) Loss in Bobo-Dioulasso

c. Transition level

Figure 4.6 shows the transition level changes for built-up gain and agricultural loss in Ouagadougou and Bobo-Dioulasso. The transition level analyses focused on built-up and agriculture categories because they are the dominant classes throughout the four time points. The gain and loss intensities are analysed regarding the deviation of each category's intensity from the uniform intensity. When a category's intensity is higher than the uniform intensity, the transition targets that category; and when a category's intensity is less than the uniform intensity value, the transition avoids that category.

In Ouagadougou, the gain of built-up area targeted bare and agricultural lands ($R_{tin} > W_{tn}$) in all the time intervals (Figure 4.6a). The other classes were avoided ($R_{tin} < W_{tn}$). The major transition to built-up category came from bare land, with an increasing intensity (R_{tin}) going from 6.81 per cent in 2003 - 2009 to 9.91 per cent in 2009 - 2015 and 10.04 per cent in 2015 - 2021. That could be explained by the greater transition intensity of bare land which largely exceeds the uniform line. As for agricultural loss, it targeted forest in all the time intervals, while in 2003 - 2009, and 2009 - 2015, water was also converted to agricultural land (Figure 4.6b). In addition, between 2003 and 2009 and 2015 and 2021 bare land and built-up areas, respectively recorded some gains from agricultural land. The major gainer from agriculture was forest, with a peak intensity in 2009 - 2015.

In Bobo-Dioulasso, the built-up class only gained from bare and agricultural lands (Figure 4.6c). Indeed, the bare land class was targeted in 2003 - 2009 and 2009 – 2015 (R_{tin}=4.61 per cent and 1.34 per cent respectively), while in 2015 – 2021 the agricultural class took over and started getting targeted (R_{tin} = 0.74 per cent) by built-up. The explanation for such a situation could be that people used all the bare land areas for building and started exploiting agricultural lands. It could also be caused by classification errors resulting in a confusion between bare and agricultural lands. The loss of agricultural land area occurred in favour of forest, bare land and built-up (Figure 4.6d). The loss targeted ($R_{tin} > W_{tn}$) bare land and forest. Built-up gain from agricultural was avoided in Bobo-Dioulasso. This could be explained by the fact that the over-exploited agricultural areas got degraded with similar spectral characteristics as bare land. A few of these areas are used for building, pavement, road construction.

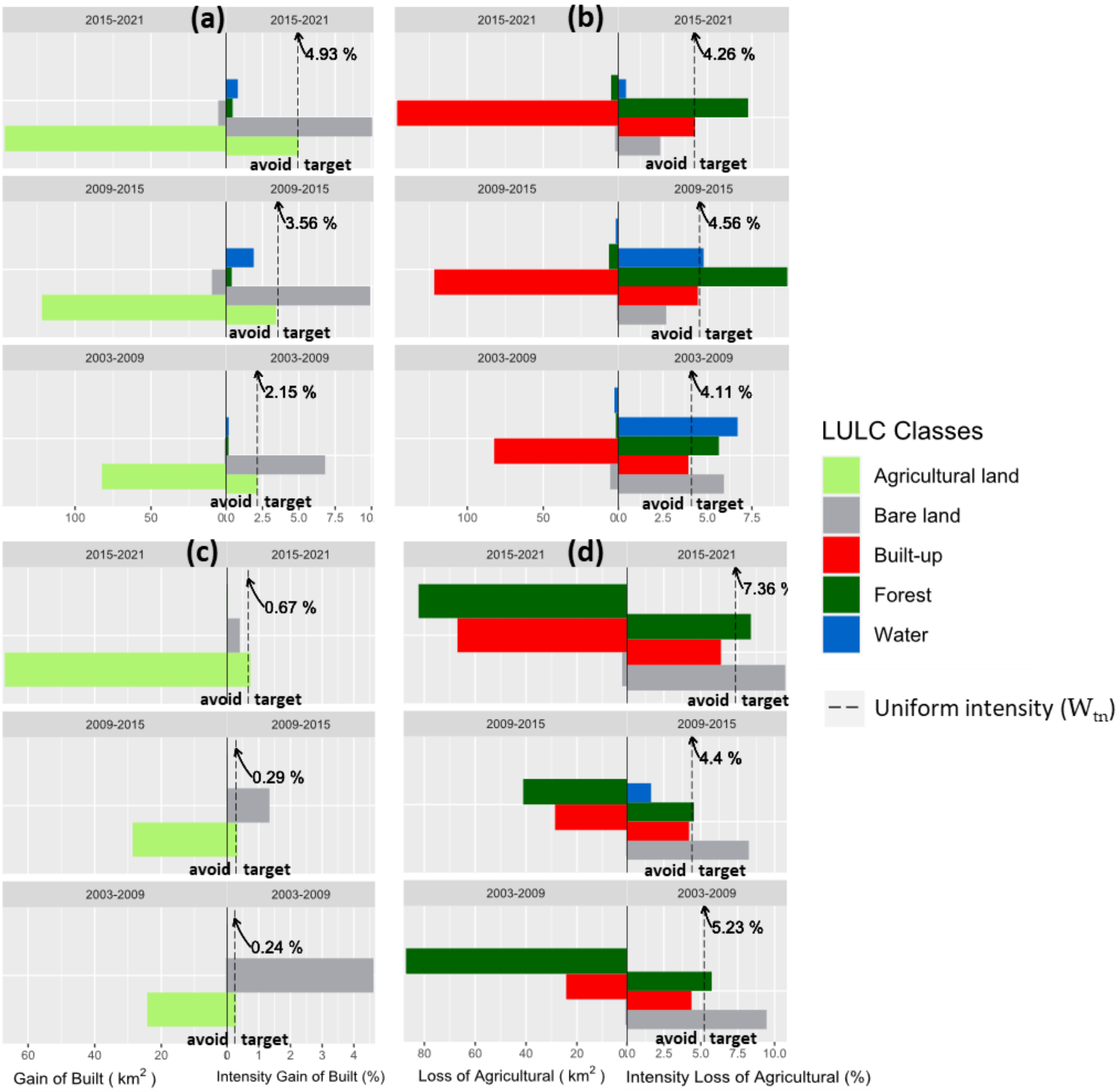

Figure 4.6: Transition Level Changes of Land Use/Land Cover: (a) Gain of Built in Ouagadougou, (b) Loss of agricultural in Ouagadougou, (c) Gain of Built in Bobo-Dioulasso, (d) Loss of Agricultural in Bobo-Dioulasso

4.1.2. LST and air temperature trend assessment

4.1.2.1. *Spatial distribution of day and night LST*

Figures 4.7 and 4.8 show the spatial distribution of yearly daytime, and night-time LST in Ouagadougou and Bobo-Dioulasso, respectively. The daytime LST showed high values in the city centre, the CBD area, while the outskirts recorded relatively low values with scattered hot spots of moderate to high LST values across the area. The high values in the CBD are due to the presence of concrete surfaces across that area. In Ouagadougou, the yearly minimum day LST was 39.03°C and was recorded in 2008, while a maximum value of 40.52°C was recorded in 2021. For Bobo-Dioulasso, the minimum daytime LST was 37.55°C, recorded in 2012, whilst the maximum recorded was 38.60°C in 2021. The coolest year in terms of daytime LST was 2008 for Ouagadougou and 2012 for Bobo-Dioulasso. Both sites experienced their hottest LST in 2021.

The night-time LST figures present persistent heat island, which got increased over time, in the city centre. Unlike the daytime LST, the night-time one exhibits hot spots only at the CBD area of both cities. This situation can be explained by the increases in heat storage due to expanding concrete surface. In Ouagadougou, the minimum annual night-time LST recorded was 19.60°C in 2008, while the maximum was 21.31°C in 2021. For Bobo-Dioulasso, the minimum night-time LST was 19.33 in 2008, and the maximum recorded was 20.49°C in 2021. During the study period, the minimum and the maximum LST, in both sites, were recorded in 2008 and 2021 respectively. In addition, Ouagadougou experienced higher LST values than Bobo-Dioulasso throughout the period, due to the high rate of concrete surface expansion, mainly built-up surfaces.

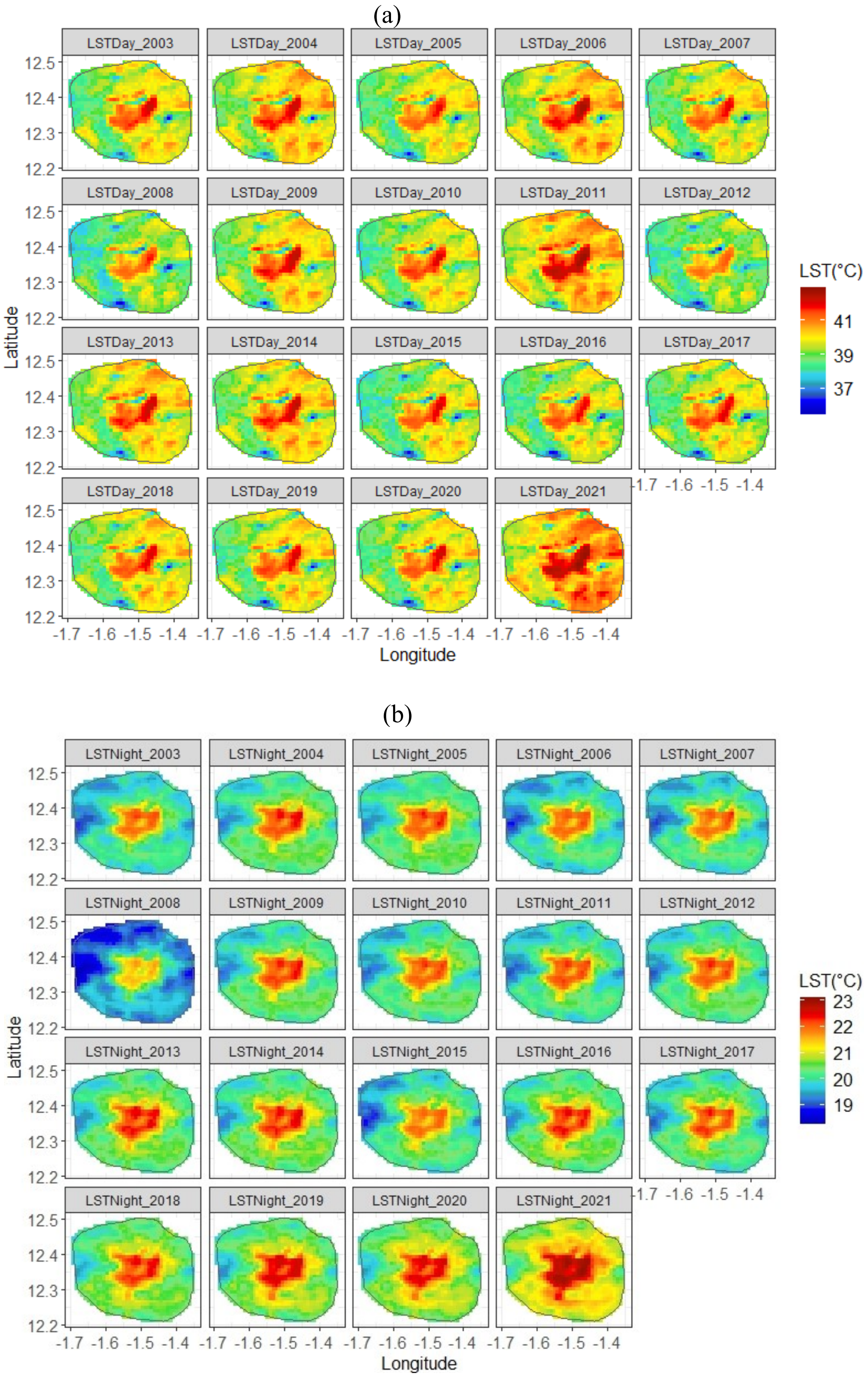

Figure 4.7: Distribution of Yearly Daytime (a) and Night-Time (b) LST in Ouagadougou

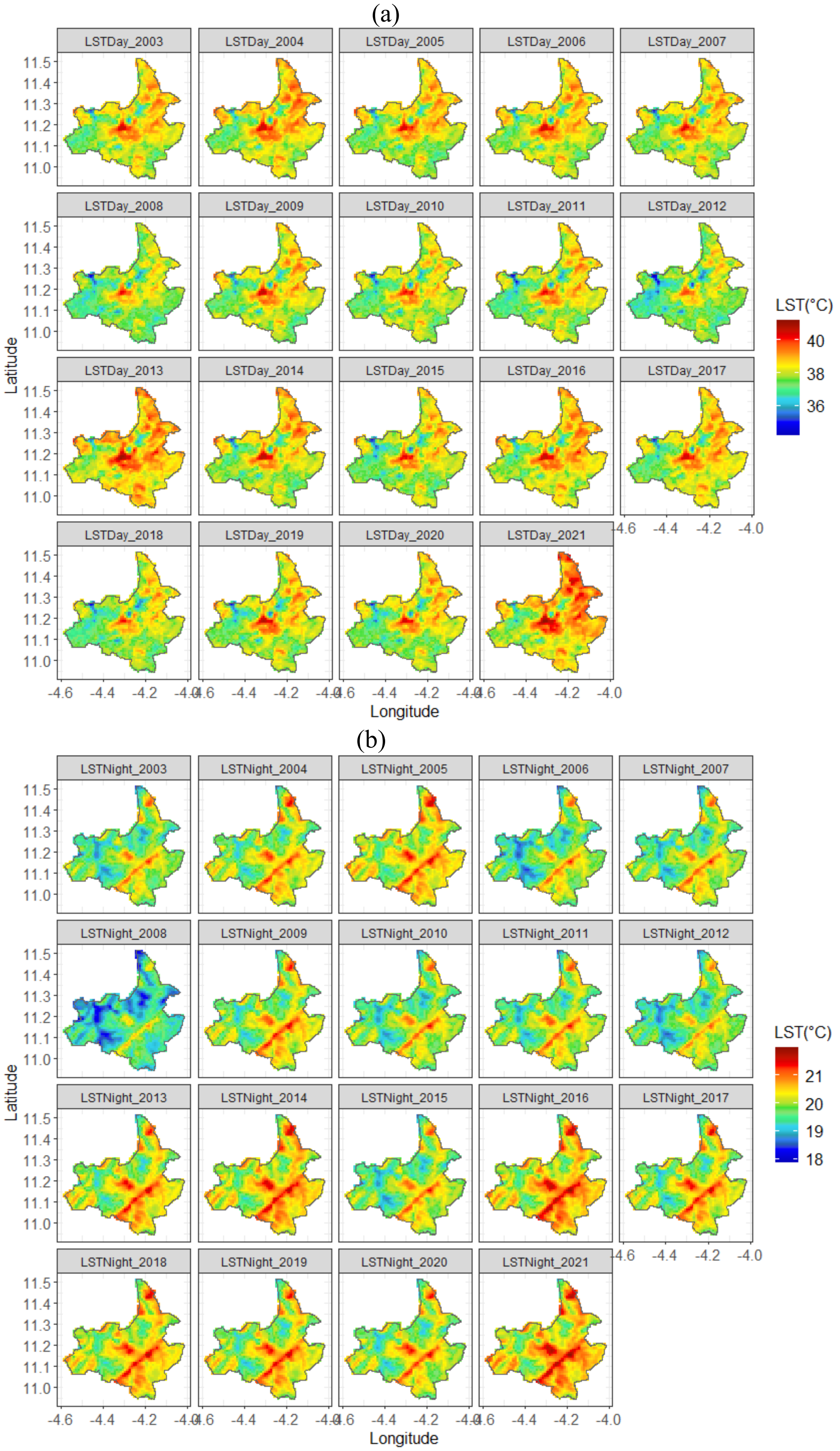

Figure 4.8: Distribution of yearly daytime (a) and night-time (b) LST in Bobo-Dioulasso

4.1.2.2. *Spatial distribution of yearly mean LST*

Figures 4.9 and 4.10 present the distribution of yearly mean surface temperature in Ouagadougou and Bobo-Dioulasso, respectively. Like the daytime and night-time LST, the mean maps show a persistent heat island in the cities' centres. The minimum yearly average LST recorded in 2008 were 29.33°C in Ouagadougou and 28.49°C in Bobo-Dioulasso. As for the maximum values, they were recorded in 2021 with 30.84°C in Ouagadougou and 29.51°C in Bobo-Dioulasso.

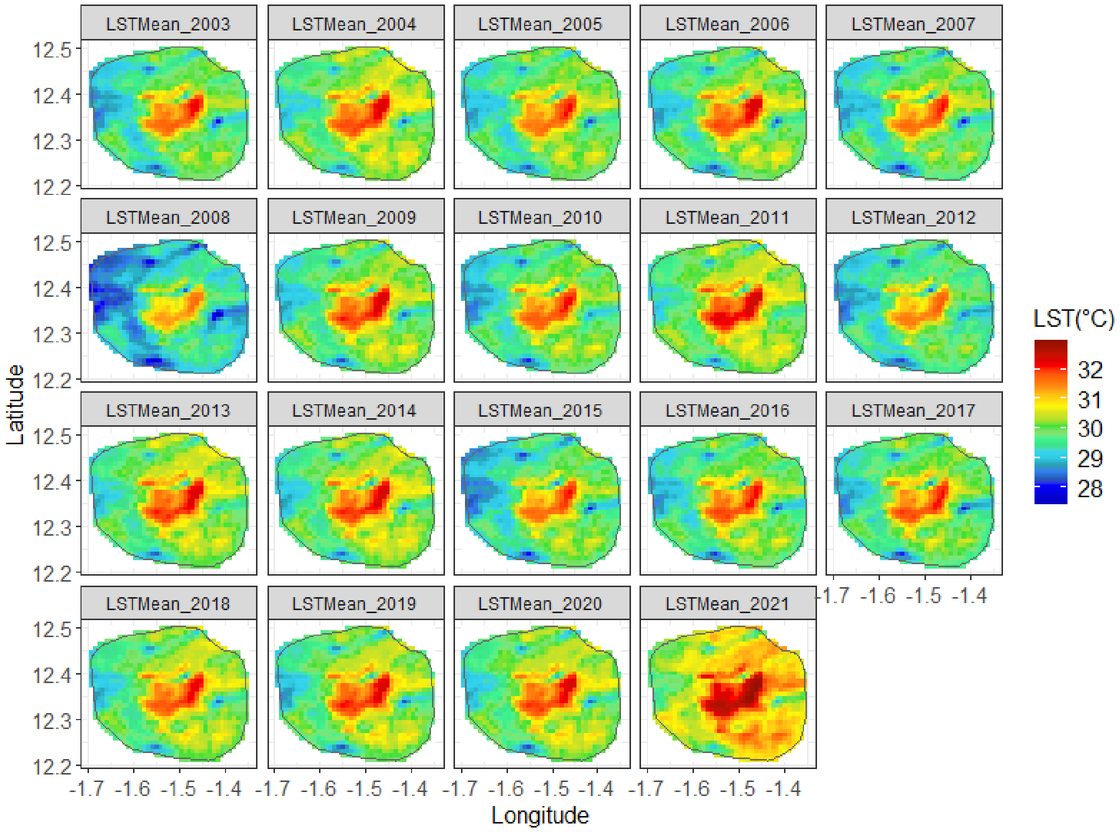

Figure 4.9: Distribution of Yearly Mean LST in Ouagadougou

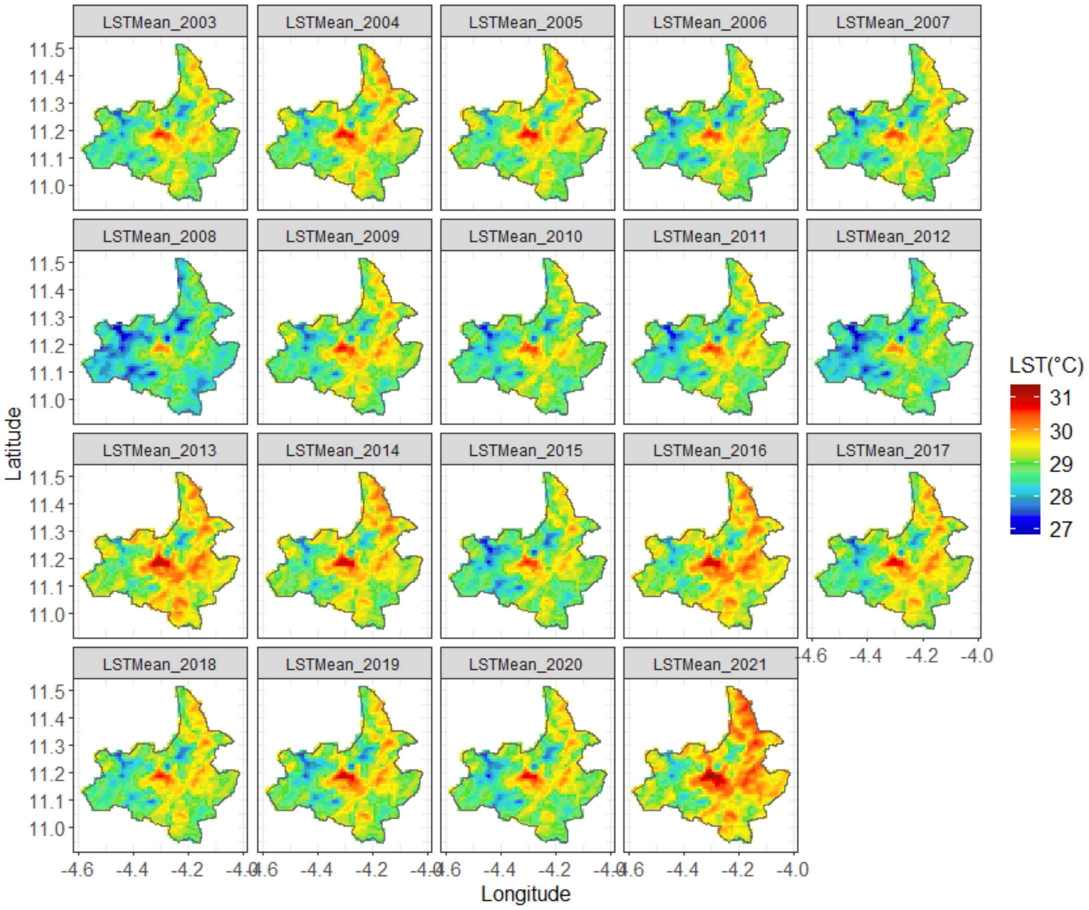

Figure 4.10: Distribution of Yearly Mean LST in Bobo-Dioulasso

4.1.2.3. *Temporal trends in LST*

Figure 4.11 which shows the evolution of yearly mean surface temperature indicates an increasing trend of LST from 2003 to 2021 for both cities. In Ouagadougou, the LST values are higher than they are for Bobo-Dioulasso. To give a deeper insight into the trends for the two sites, seasonal analysis was performed (Figure 4.12). Figure 4.12 shows that the surface temperature is increasing across all climatological seasons except June-July-August (JJA) and December-January-February (DJF) which show decreasing trends, respectively for Ouagadougou and Bobo-Dioulasso. Looking at the Mann-Kendall trend test metrics (Table 4.2), it appears that the yearly average LST exhibits a non-significant increasing trend with a Sen's slope of 0.18°C in Ouagadougou against 0.10°C in Bobo-Dioulasso. That shows that the yearly LST is increasing at a faster rate in Ouagadougou than Bobo-Dioulasso. Only the March-April-May (MAM) season shows a significant trend with a probability value (p −value) of 0.009, which is less than 0.05 in Ouagadougou. In Bobo-Dioulasso, all the p −values are more than 0.05, meaning that the trend is non-significant. The seasonal analysis highlighted that the yearly LST increases is mainly driven by the MAM season (Figure 4.14) with a mean variation of 0.05°C for Ouagadougou as against 0.03°C for Bobo-Dioulasso (Table 4.7). Despite its non-significant trend in the areas, the September-October-November (SON) season also contributes to the global yearly increasing trend of LST.

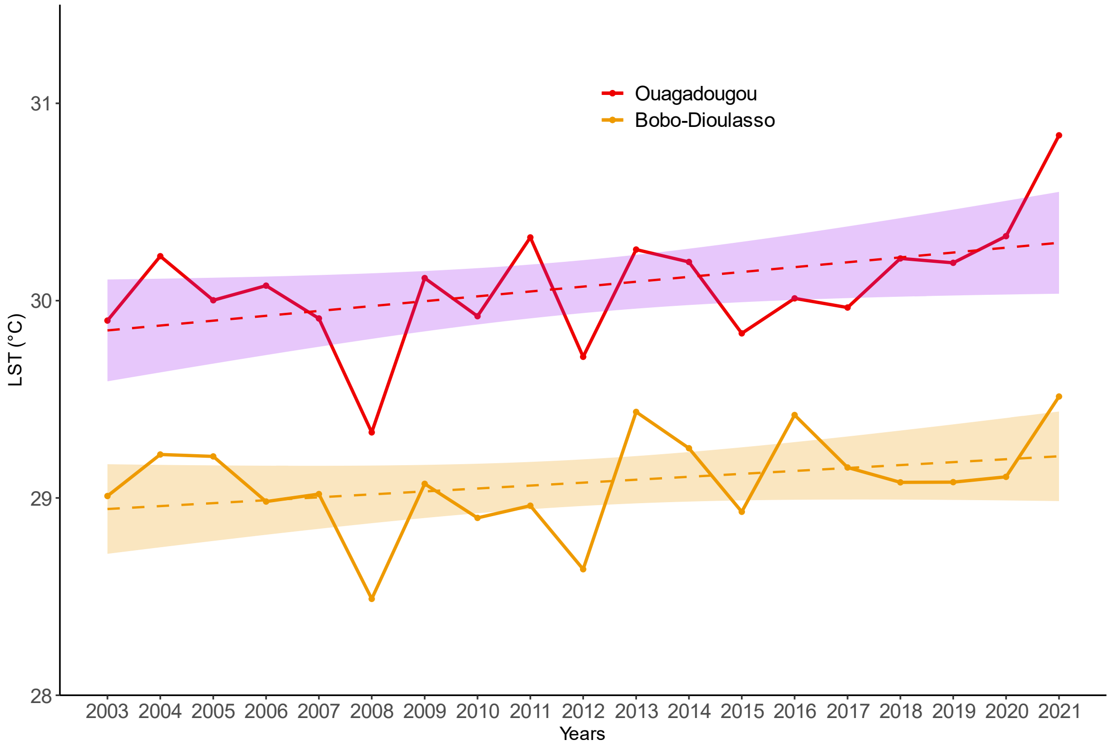

Figure 4.11: Yearly Mean LST Evolution from 2003 to 2021

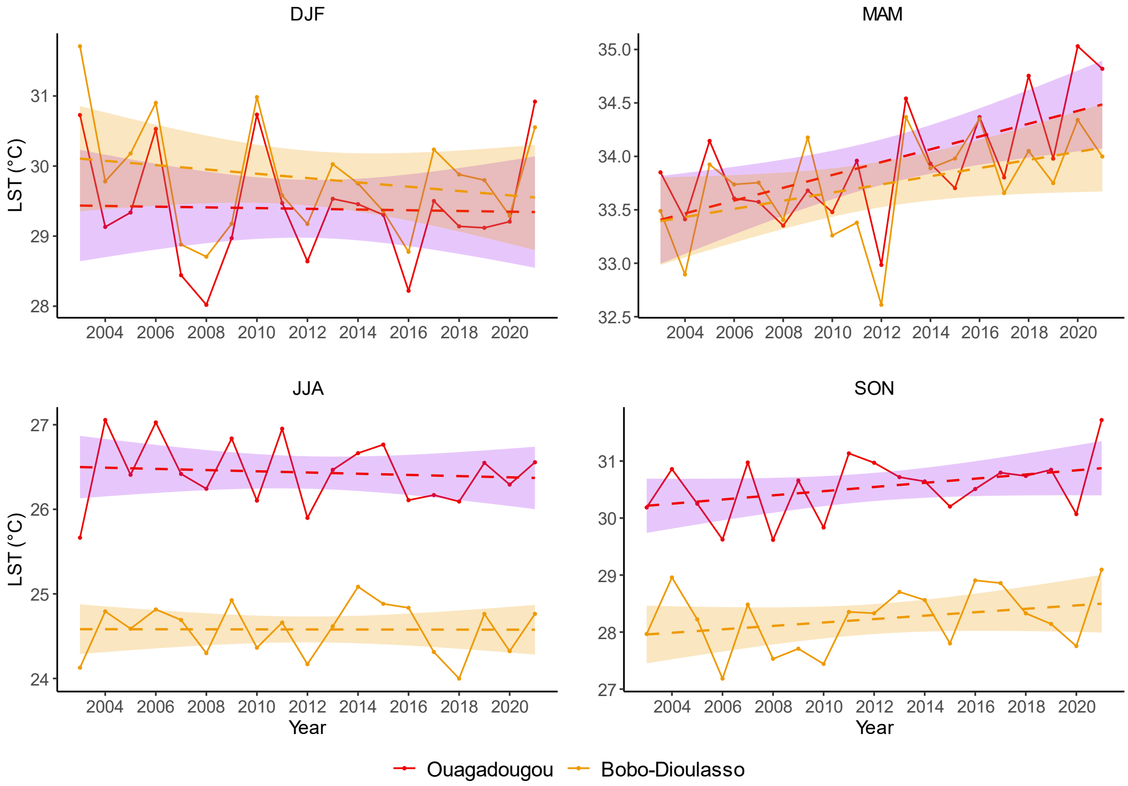

Figure 4.12: **Seasonal Mean LST Evolution from 2003 to 2021**

Table 4.7: Mann Kendall Trend Test Metrics for Surface Temperature

Ouagadougou

	Seasonal average				Yearly average
	DJF	**MAM**	**JJA**	**SON**	
Z value	0	2.59	-0.48	1.04	1.82
Sen's slope	-0.00084	0.05	-0.01	0.030	0.018
P value	1	0.009	0.62	0.29	0.068
Trend	Increasing	Increasing	Decreasing	Increasing	Increasing

Bobo-Dioulasso

	Seasonal average				Yearly average
	DJF	**MAM**	**JJA**	**SON**	
Z value	-0.27	1.75	0.07	1.12	1.26
Sen's slope	-0.02	0.03	0.001	0.038	0.010
P value	0.77	0.08	0.94	0.26	0.20
Trend	Decreasing	Increasing	Increasing	Increasing	Increasing

Source: Author's data analysis (2023)

4.1.2.4. *Temporal trends in air temperature*

Figure 4.13 presents the yearly trends in air temperature across Bobo-Dioulasso and Ouagadougou. There is an increasing trend in air temperature throughout the study time span over the two areas. The minimum yearly values recorded were 28.04°C in Ouagadougou and 27.04°C in Bobo-Dioulasso in 2008. The maximum values were recorded in 2021 with 29.32°C for Ouagadougou and 28.17°C for Bobo-Dioulasso. The Mann-Kendall test showed that the yearly temperature trend is non significant, because the p −values are greater than 0.05 for both cities (Table 4.8). The trend was more pronounced in Bobo-Dioulasso than Ouagadougou, regarding the respective Sen's slope values of 0.014°C and 0.018°C.

The seasonal trend (Figure 4.14) showed an increasing trend for all climatological seasons, except the DJF season which depicted a decreasing trend for both cities. The

MAM season showed the highest trend with a p −values of 0.012 for Ouagadougougou and 0.021 for Bobo-Dioulasso (Table.4.8). It was followed by the JJA season which presented a non-significant trend.

As for the surface temperature, the yearly global trend is engineered by the MAM season which showed an average temperature increase of 0.052°C in Ouagadougou and 0.047°C in Bobo-Dioulasso during the study period.

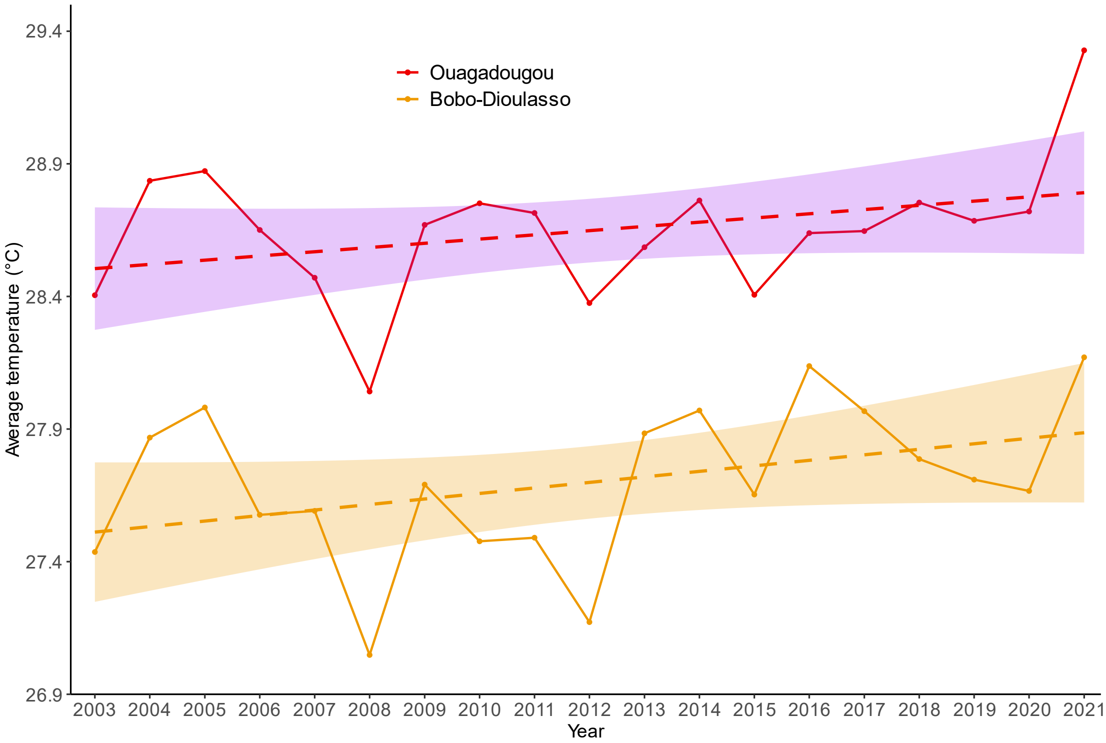

Figure 4.13: **Yearly Mean Air Temperature Evolution**

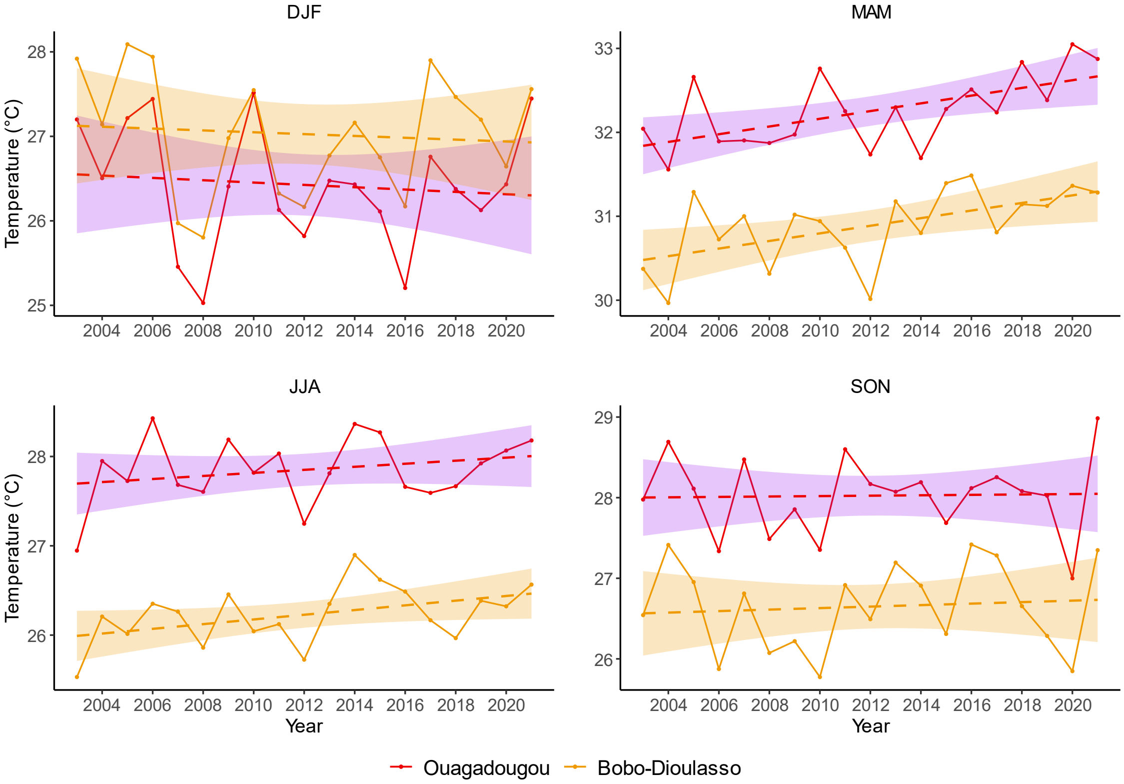

Figure 4.14: Seasonal Mean Air Temperature Evolution

Table 4.8: **Mann Kendall Trend Test Metrics for Air Temperature**

Ouagadougou

	Seasonal average				Yearly average
	DJF	**MAM**	**JJA**	**SON**	
Z value	-0.350	2.519	0.630	0.140	1.050
Sen's slope	-0.006	0.052	0.014	0.003	0.014
P value	0.726	0.012	0.529	0.889	0.294
Trend	Decreasing	Increasing	Increasing	Increasing	Increasing

Bobo-Dioulasso

	Seasonal average				Yearly average
	DJF	**MAM**	**JJA**	**SON**	
Z value	-0.210	2.309	1.749	0.280	1.679
Sen's slope	-0.011	0.047	0.023	0.014	0.018
P value	0.834	0.021	0.080	0.780	0.093
Trend	Decreasing	Increasing	Increasing	Increasing	Increasing

Source: Author's data analysis (2023)

4.1.2.5. *Spatial distribution of SUHI in the study area*

The LST anomaly between the city centre and the surrounding areas showed high values in the city core. During the study period, the daytime SUHI, at 1 square kilometre pixel scale, fluctuated between -0.098°C (2017) and 0.071°C (2015) in Ouagadougou, while in Bobo-Dioulasso, it oscillated between -0.092°C (2004) and 0.072°C (2019) Concerning the night-time SUHI, the values varied between -0.073°C (2021) and 0.11°C (2007) in Ouagadougou, and between -0.069°C (2011) to 0.080°C (2009) in Bobo-Dioulasso. Like the LST, the SUHI maps showed heat hotspots at the city centre and relatively cool hotspots at the surrounding areas. SUHI is more pronounced during night-time with a strong heat island covering the inner city, particularly in Ouagadougou (Figure 4.15). In Bobo-Dioulasso, strong heat island is found in the city centre and water areas during night-time (Figure 4.16).

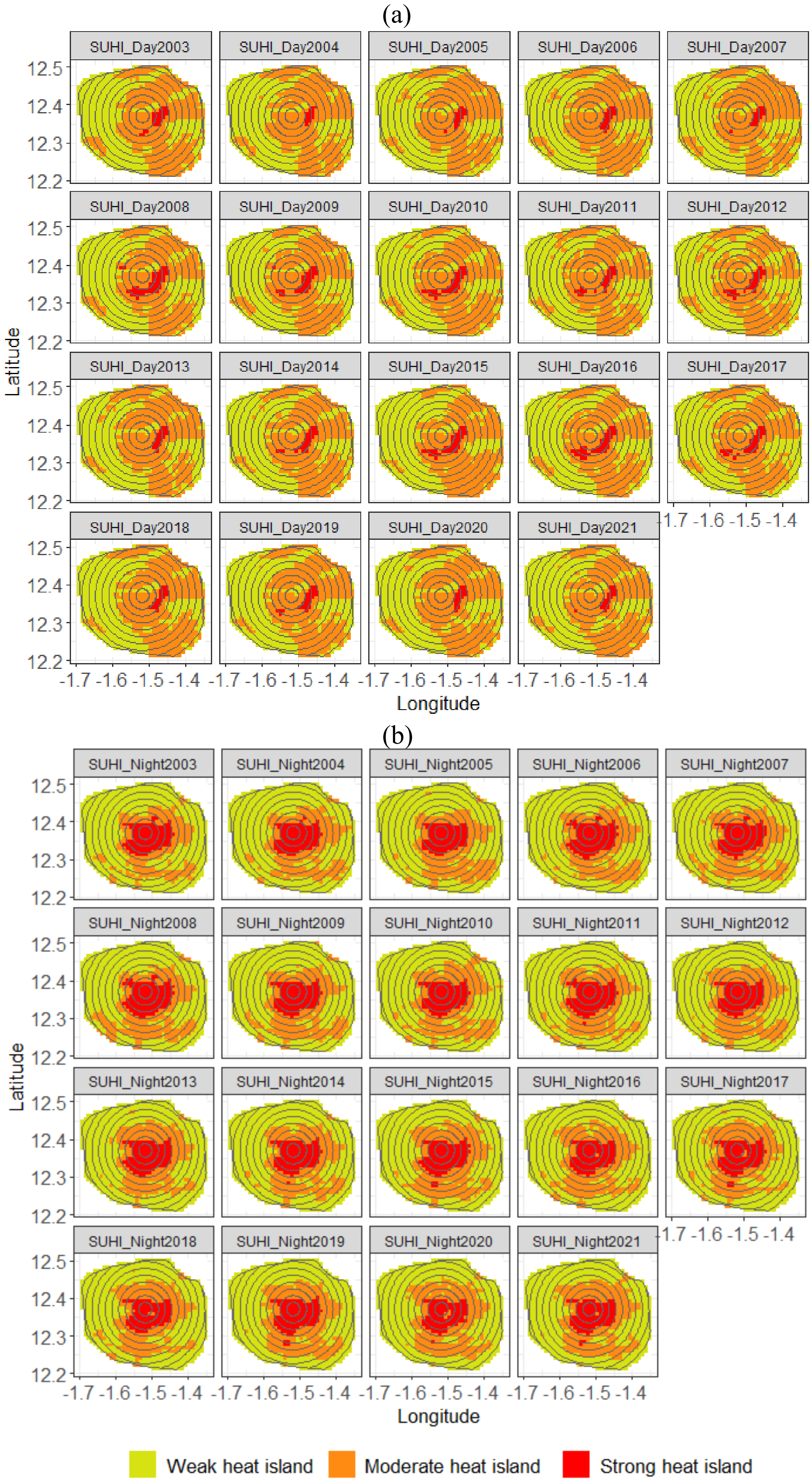

Figure 4.15: Distribution of Yearly Daytime (a) and Night-Time (b) SUHI in Ouagadougou

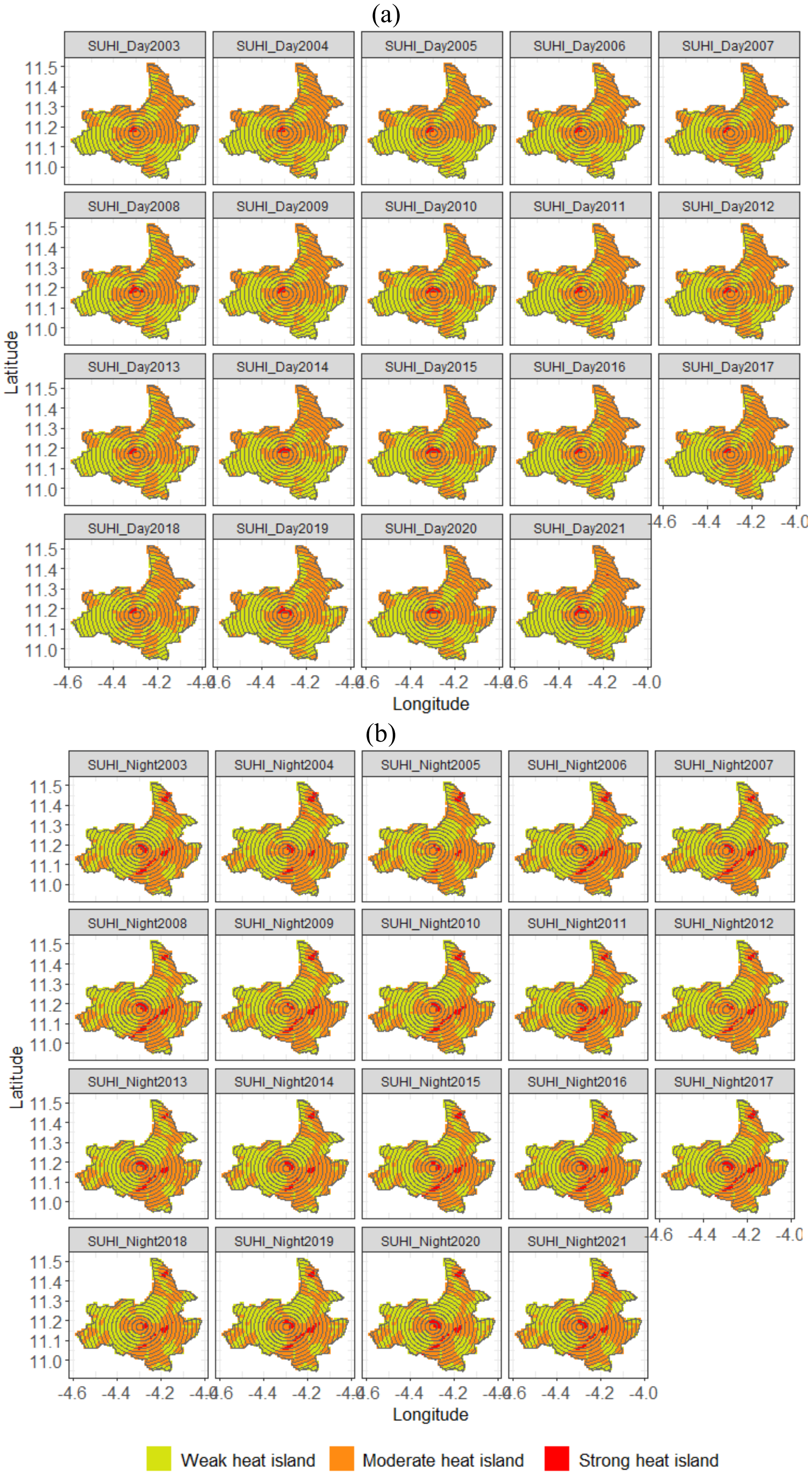

Figure 4.16: Distribution of Yearly Daytime (a) and Night-Time (b) SUHI in Bobo-Dioulasso

4.1.2.6. *SUHI trend in the study area*

The SUHI intensity, plotted according to the distance from the city centre, showed that the closer it is to the centre, the higher the intensity (Figure 4.17). The dotted horizontal line indicates the 0 zero value. There was a uniform trend throughout the study period with differences between daytime and night-time. Daytime SUHI increased in the inner city (1 – 6 kilometres for Ouagadougou and 1 – 3 kilometres for Bobo-Dioulasso). The break at 2 kilometres in Ouagadougou indicates the urban dams and forest areas. After the peak at 6 kilometres and 3 kilometres in the respective cities, the SUHI decreased up to 20 kilometres with some breaks due to water and forest areas. During night-time, the SUHI decreased from the city centre towards the periphery, with some breaks in Bobo-Dioulasso.

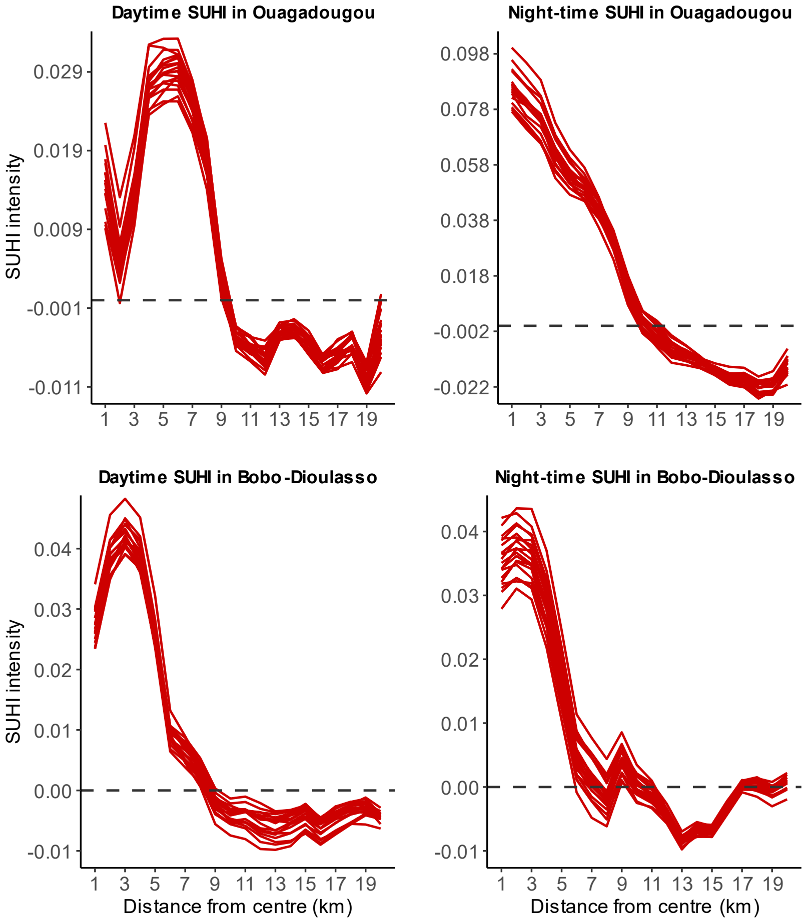

Figure 4.17: SUHI Intensity Patterns According to the Distance from the City centre

4.1.2.7. *Correlation between LST and air temperature*

In order to establish the relationship between LST and 2 metres above ground air temperature, a t-Test was performed to study the difference in mean values of the two variables. Table 4.9 presents the results of the test. The p −value of the test is less than 0.05 in both cities, indicating that there is a significant difference between the LST and the air temperature in terms of mean values. The average difference was 1.42 for Ouagadougou and 1.38 for Bobo-Dioulasso. The 95 per cent confidence interval lies between -1.54 and -1.31 for Ouagadougou and between -1.49 and -1.26 for Bobo-Dioulasso, which exclude the value zero. Based on the confidence interval, there is a significant difference between the mean values of the two datasets.

Table 4.9: Outputs of T-Test Between Surface and Air Temperature

Metric	Ouagadougou	Bobo-Dioulasso
Confidence interval	-1.54 to -1.31	-1.49 to -1.26
F-statistics	0.57	0.36
Mean LST	30.07	29.08
Mean air Temp.	28.65	27.70
p-value	P<0.05	P<0.05
Mean difference	1.42	1.38

Source: Author’s data analysis (2022)

Furthermore, a correlation analysis was performed to determine the level of relationship between LST and 2 metres above ground air temperature. The scatterplots presented in Figure 4.18 show a non-linear regression between air temperature and LST. The two variables have a strong positive correlation in both cities throughout the study time span. The Spearman correlation coefficient was 0.76 in Ouagadougou and 0.83 in Bobo-Dioulasso. Then, the correlation analysis showed a significant ($p<0.05$) positive correlation between the variables, indicating that when the LST increases, the air temperature also increases. Thus, the coefficients of determination R^2 showed that 58 per cent and 69 per cent of the increase in air temperature in Ouagadougou and Bobo-Dioulasso respectively, from 2003 to 2021, could be explained by the increase of the LST during the period.

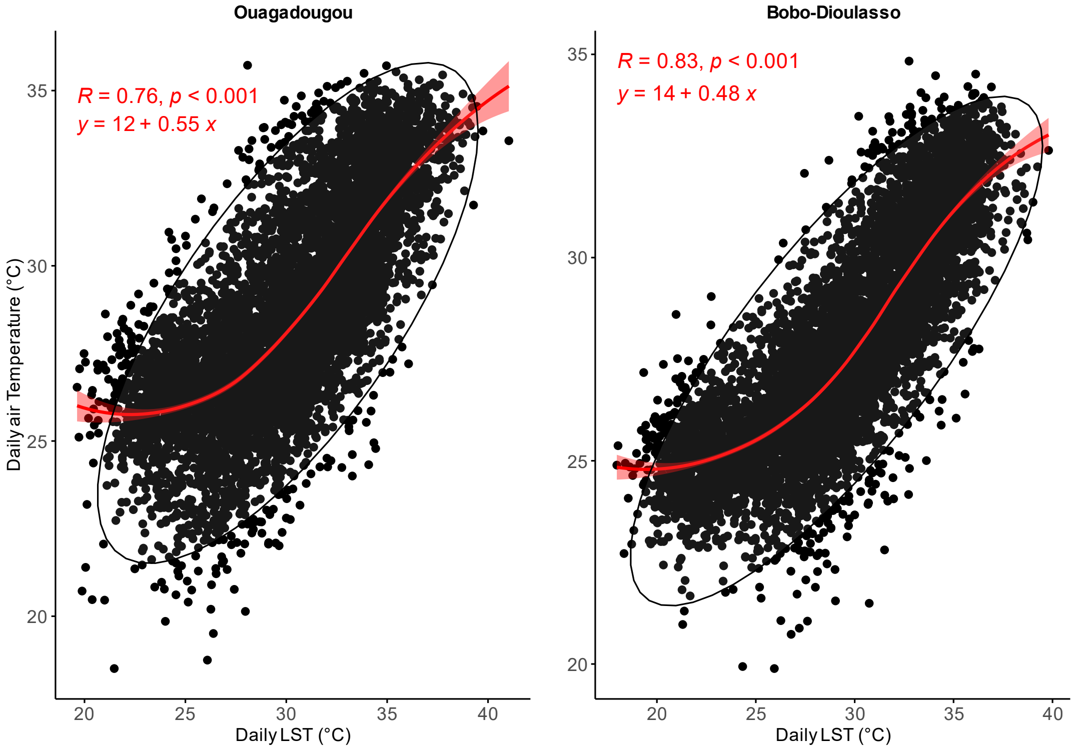

Figure 4.18: Daily LST and Air Temperature Regression

4.1.3. Land Use/Land Cover and LST relationship

4.1.3.1. *Land Use/Land Cover and LST patterns*

Figures 4.19 and 4.20 present the spatial distribution of the pure pixels (100 per cent built and 100 per cent non-built) in relation to LST. The pixels that are covered by pure built-up class increased while the pure non-built-up pixels decreased from 2003 to 2021 in both cities. The number of pure built-up pixels were 55, 39, 67, and 67 respectively in 2003, 2009, 2015 and 2021 for Ouagadougou (Figure 4.19). For Bobo-Dioulasso, the number of pure built-up pixels varied from 15 in 2003 to 21 in 2009, 29 in 2015, and reached 44 in 2021 (Figure 4.20). The expansion in the number of pure built-up pixels co-occurred with the increasing of LST from the city core towards the outskirts, at the expense of the pure non-built pixels. The relative low number of built-up pixels in Bobo-Dioulasso compared to Ouagadougou indicates a more rapid concrete surface formation and then higher LST values in Ouagadougou than Bobo-Dioulasso. Thus, there is a close link between the type of LULC within a 900×900 square metres grid and the average temperature at the surface at this grid.

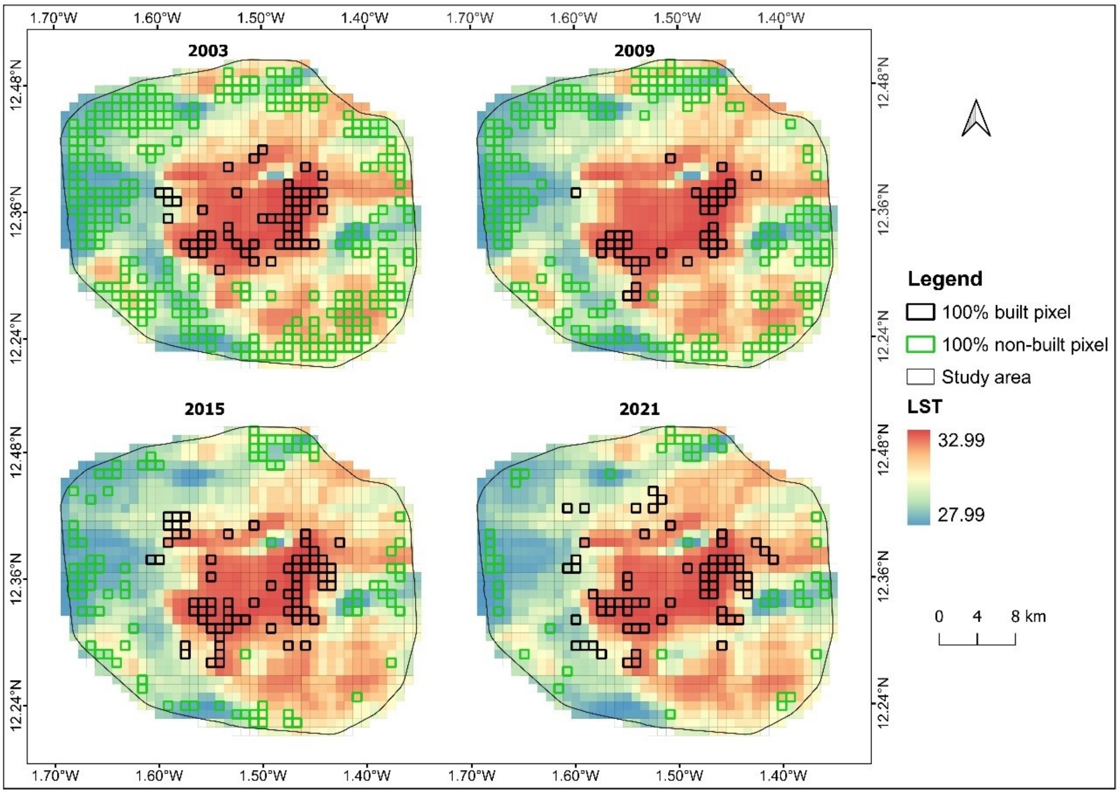

Figure 4.19: Spatial Distribution of Pure Built-Up and Non-Built-Up Pixels in Ouagadougou

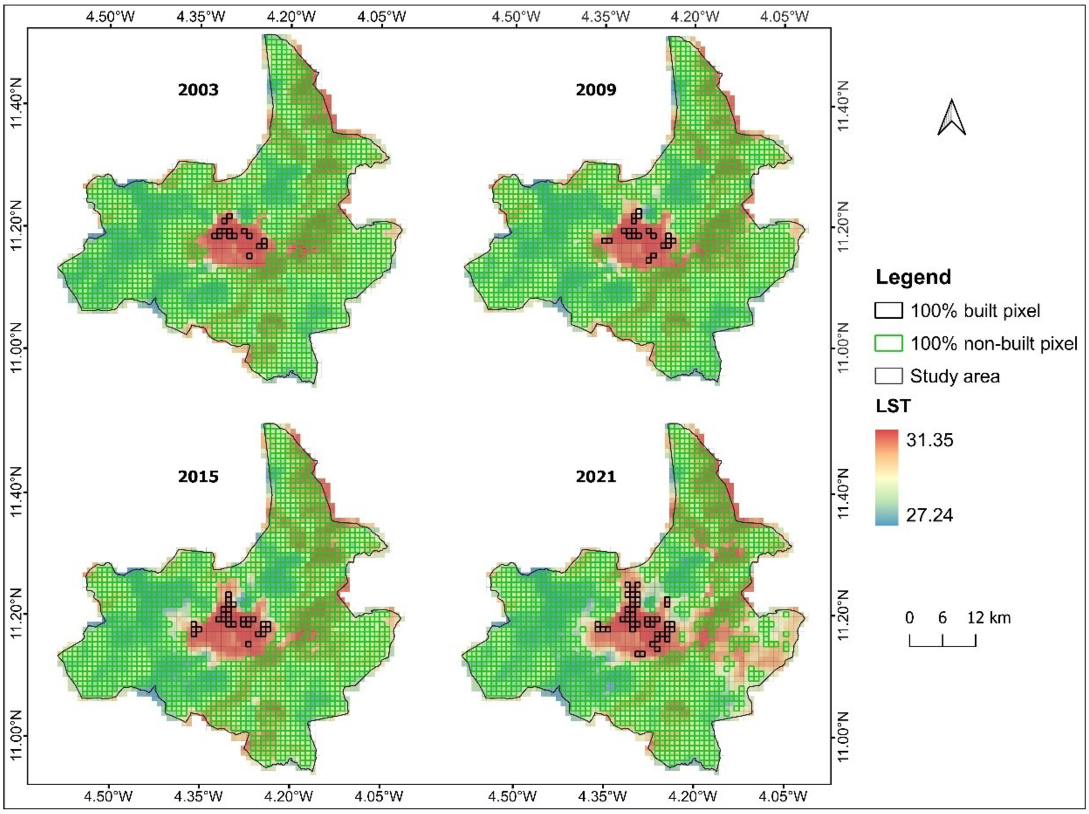

Figure 4.20: Spatial Distribution of Pure Built-Up and Non-Built-Up Pixels in Bobo-Dioulasso

Figure 4.21 presents the fluctuation of LST according to the percentage of built and non-built coverage in each 900 × 900 square metres grid. Indeed, the pixels covered totally by built-up area have a high surface temperature, while the temperature is low for those with of 100 per cent non-built coverage. Globally, when the non-built-up coverage increases, the LST shows a regressive variation. A large proportion of non-built-up area in a pixel indicates a decrease in LST while a larger built-up area implies an increase of surface temperature. The LST variation pattern regarding the rate of built-up and non-built-up coverage in a pixel was linear in Ouagadougou throughout the study period.

However, in Bobo-Dioulasso, particularly in 2003 and 2009, the pattern was non-linear. This could be due to the intervention of other factors influencing the LST such as soil moisture, wind or high heat capacity surfaces in areas with higher non-built-up cover in

Bobo-Dioulasso. The difference in LST between a fully built-up pixel and an entirely non-built-up pixel varied from 1.47°C to 1.87°C in Ouagadougou against 1.02°C to 1.27°C in Bobo-Dioulasso. These different values experienced decreases from 2003 to 2021 in both cities, showing that the LST in all LULC classes increased.

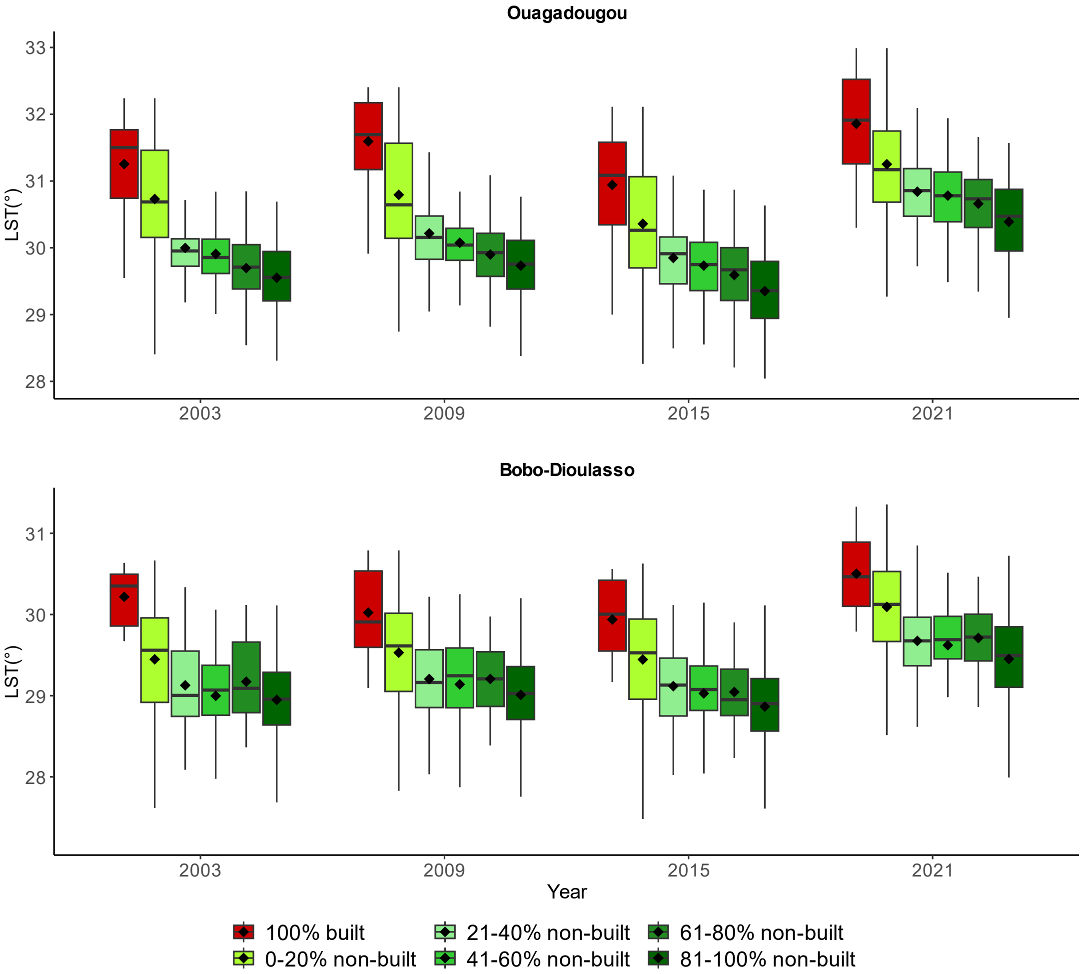

Figure 4.21: **Built-Up and Non-Built-Up Surface Temperature Patterns**

The analysis of LST and LULC patterns showed that the built-up areas present higher LST than non-built-up areas such as forest, water bodies and farmland. The LST trend throughout the study period showed that Ouagadougou was warmer than Bobo-Dioulasso, because Ouagadougou had greater built-up cover, compared to other LULC classes, than Bobo-Dioulasso. Indeed, the built-up cover varied from 32.75 per cent in

2003 to 35.95 per cent in 2009, 46.86 per cent in 2015 and 58.34 per cent in 2021 for Ouagadougou. However, for Dobo-Dioulasso, the built-up area occupied 4.10 per cent, 5.19 per cent, 6.36 per cent and 9.86 per cent of the area in 2003, 2009, 2015 and 2021 respectively.

At the pixel scale, the LST increased with the proportion of built-up (settlement and bare land) within the pixel, while decreasing with the non-built cover rate. There was a decrease in the average LST difference between a pixel fully covered by built-up and a pixel entirely covered by non-built-up class, indicating a general warming of all the landscape units.

4.1.3.2. *Correlation between LST and LULC rate*

The correlation between LST and LULC rates was performed to measure the strength of relationship existing between the two variables. Figure 4.22 shows the scatterplots and the correlation statistics between LST and built-up cover rate in a grid of 900×900 m^2. The figures show that there is a positive relationship between the LST and the different built cover rates: the higher the built cover rate in a pixel, the higher the corresponding LST value. The strength of correlation was moderate (Schober and Schwarte, 2018) for all the four years, with a correlation coefficient varying from 0.44 to 0.64 for Ouagadougou against 0.49 to 0.61 for Bobo-Dioulasso. Indeed, 19.36 per cent to 40.96 per cent of the LST increases in both cities, from 2003 to 2021, was due to the predominance of built-up cover in the area.

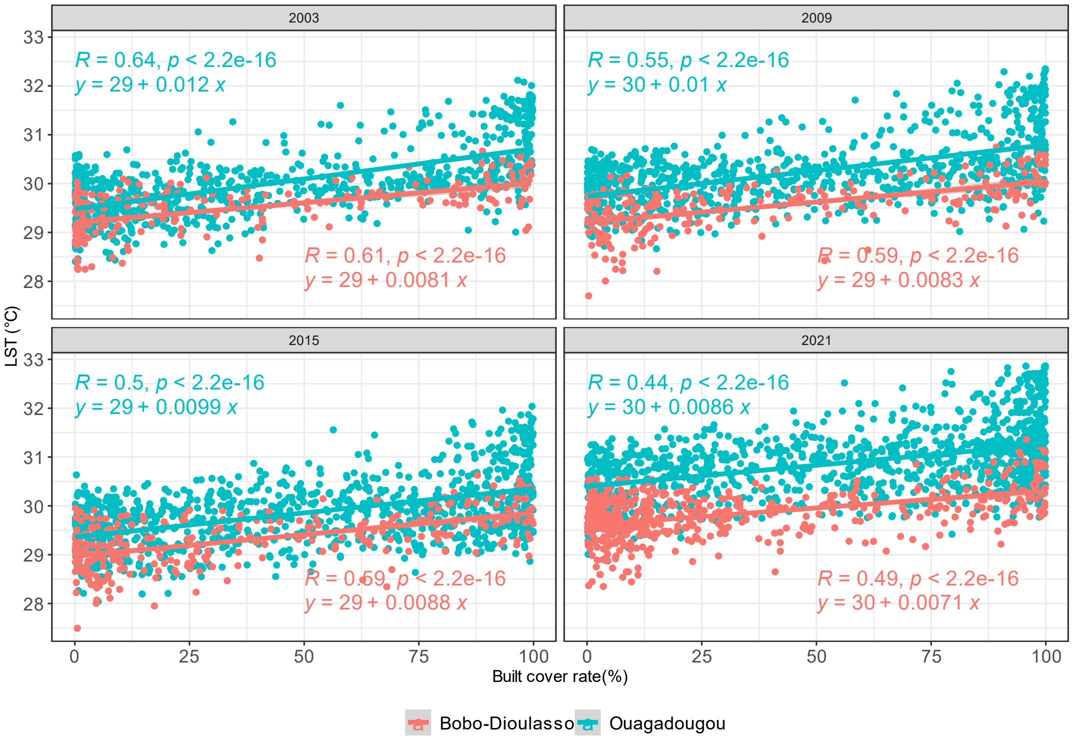

Figure 4.22: Correlation Between LST and Built-Up Cover Rate

Concerning the non-built-up cover, the correlation with the LST is negative (Figure 4.23). The correlation coefficients varied between -0.41 and -0.6 for Ouagadougou against -0.49 and -0.59 for Bobo-Dioulasso, showing a moderate negative correlation for both cities. The presence of non-built-up surface within a given pixel contributes to reduce the LST of that pixel: the higher the non-built-up proportion in the pixel, the lower the LST value.

Thus, from 2003 to 2021, 16.81 per cent to 36 per cent of the urban cooling related to surface temperature was linked to the presence of non-built-up lands such as forest, agricultural land and water bodies. Like the case of the built-up cover, the strength of the correlation decreased from 2003 to 2021 in the two cities.

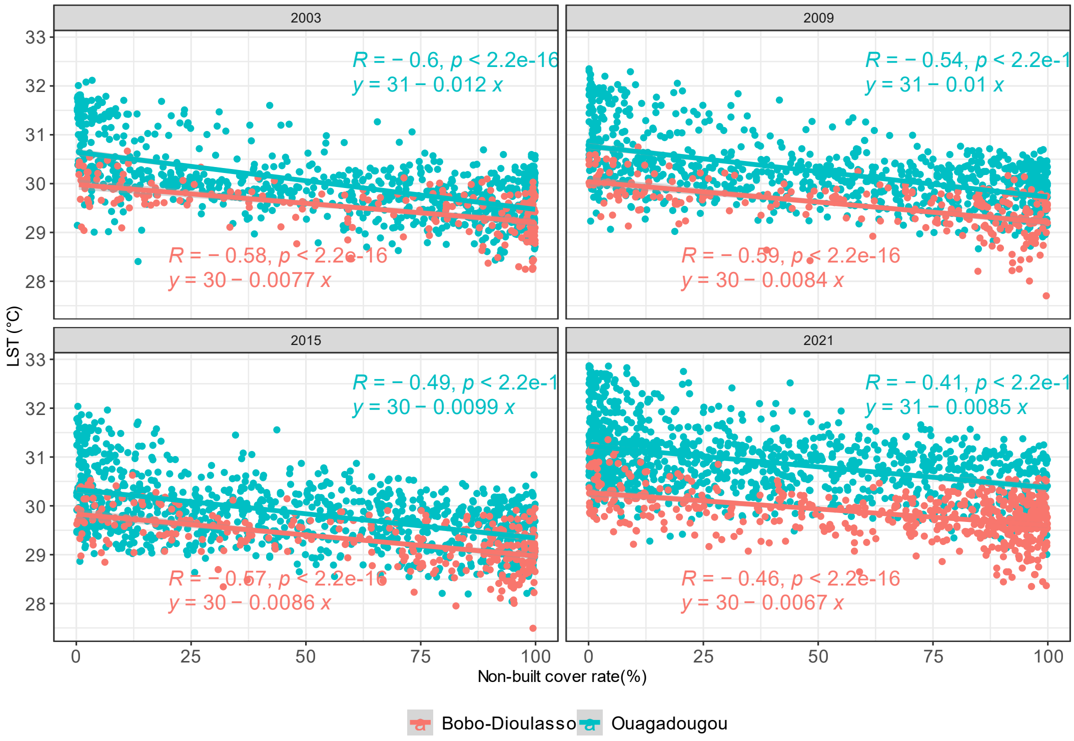

Figure 4.23: Correlation Between LST and Non-Built-Up Cover Rate

4.1.3.3. *Cooling effects of non-built cover*

Figure 4.24 shows the cooling effects of non-built-up surfaces in the study area from 2003 to 2021. The figure informs that the higher the median difference, the higher the cooling effect of the non-built cover rate. The non-built-up pixels' contribution to cooling varies according to the sites. It was lower in Bobo-Dioulasso (0.29 - 1.39°C) than in Ouagadougou (0.74 - 1.94°C). The highest contribution of non-built-up class to cooling was recorded in 2009 for Ouagadougou and 2003 for Bobo-Dioulasso.

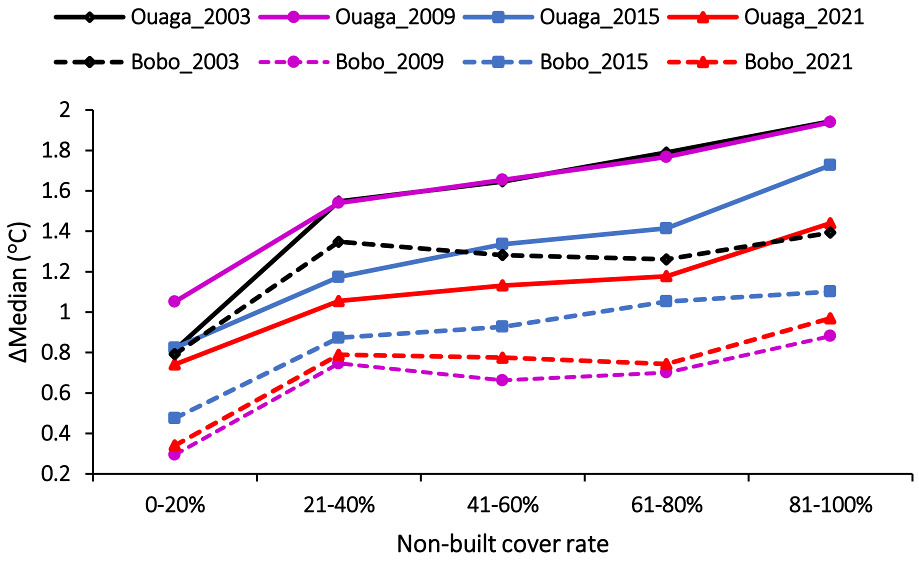

Figure 4.24: **Contribution of Non-Built-Up Cover to Urban Cooling**

In Ouagadougou, the cooling effect of non-built-up surface decreased from 2003 to 2021. With at least 21 per cent -40 per cent of non-built-up coverage in a pixel of 900×900 square metres, a surface cooling of more than 1°C was produced across the four years. However, in Bobo-Dioulasso, the non-built-up effect on cooling was not linear throughout the years. In 2003, 2009 and 2021, the cooling declined between 21 per cent coverage and 80 per cent coverage, and later peaked with 81 per cent -100 per cent coverage. Only the year 2015 showed a regular pattern in terms of cooling effects of non-built-up coverage. More than 1°C of surface cooling was achieved with 21 per cent -40 per cent coverage in 2003, 61 per cent -80 per cent coverage in 2015, while 2009 and 2021 surface cooling was less than 1°C for all the five non-built-up cover classes.

4.1.4. Relationship between LST and diseases

The relationship between LST and the number of reported cases of malaria, dengue and meningitis was computed. The monthly reported cases from the five districts of Ouagadougou and the three districts of Bobo-Dioulasso were used with the yearly mean surface temperature per district.

4.1.4.1. *Evolution of selected public diseases reported cases from 2017 to 2021*

Figures 4.25 and 4.26 present the evolution of the reported cases per month in Ouagadougou and Bobo-Dioulasso respectively. In Ouagadougou, malaria exhibited one peak in October, and dengue showed a peak between October and November. In Bobo-Dioulasso, malaria showed two peaks during the year: one in February and the other one in October, while dengue's peak was found between October and November as in Ouagadougou. As for meningitis, the figures show two peaks in both cities, one occurring between February and May, and a second one in October. The peak occurrence of the diseases corresponds to the dry hotter periods of the year when the surface receives and stores more solar radiation. The energy stored could serve to create suitable environment for the diseases' vectors evolution.

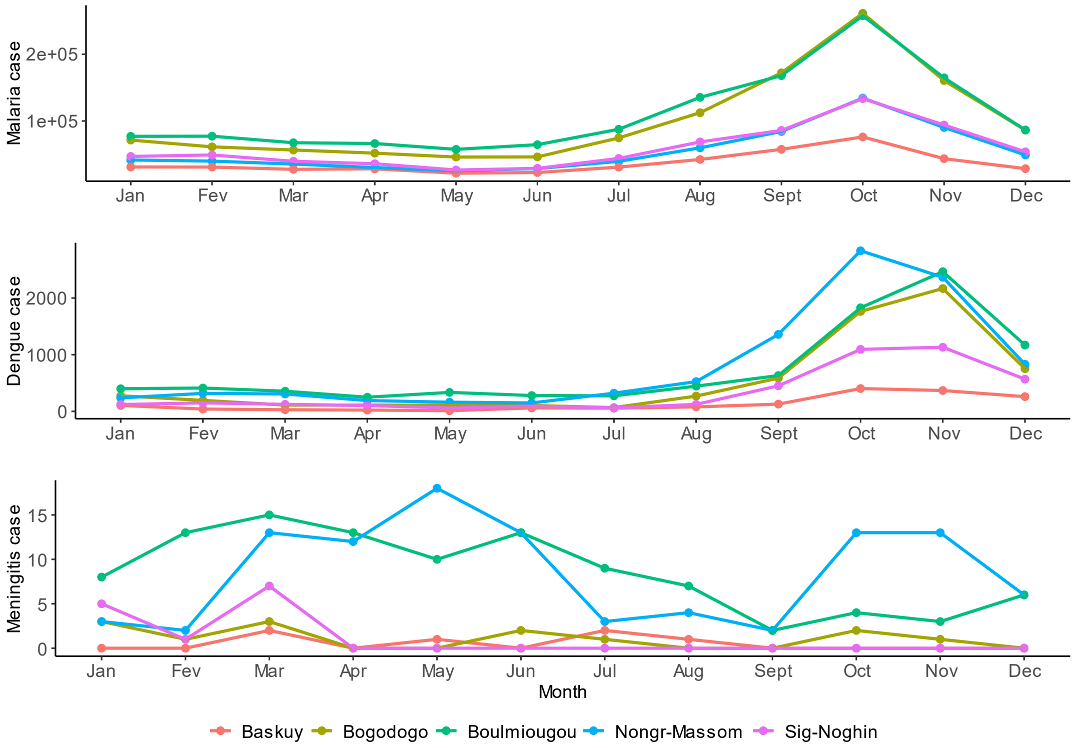

Figure 4.25: **Evolution of Monthly Reported Cases in Ouagadougou**

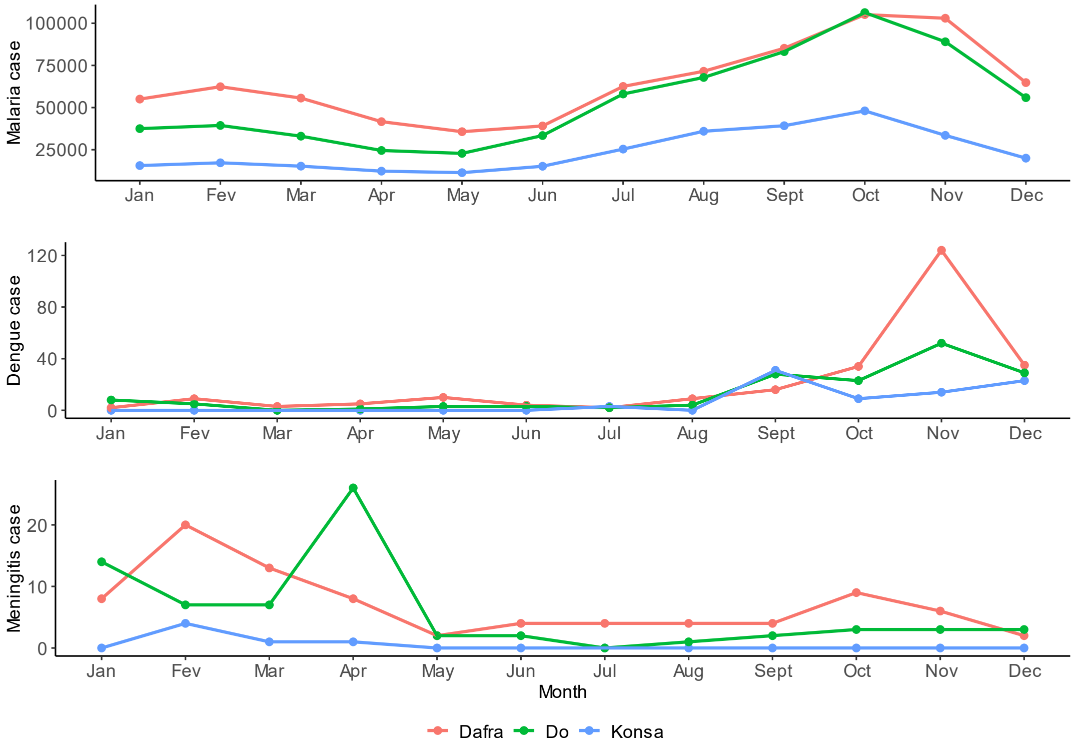

Figure 4.26: **Evolution of Monthly Reported Cases in Bobo-Dioulasso**

4.1.4.2. *Correlation between surface temperature and selected public diseases*

The level of the relationship between LST and diseases was assessed through a correlation analysis. Figure 4.27 presents the scatterplot of the correlation between LST and the diseases in Ouagadougou and Bobo-Dioulasso from 2017 to 2021. Malaria and dengue had a weak to negligible correlation with LST in the two cities. In the districts of Bogodogo, Nongr-Massom, Sig-Noghin, Do and Konsa when the LST increased, the number of reported malaria cases decreases. In the case of dengue, all the districts except Nongr-Massom and Konsa showed an increase in the number of cases when the surface temperature increases. Concerning the meningitis, the scatterplots indicate a strong positive correlation (Do) to moderate positive correlation (Dafra, Konsa, Sig-Noghin), and negligible negative correlation (Baskuy, Bogodogo, Boulmiougou, Nongr-Massom) with the surface temperature.

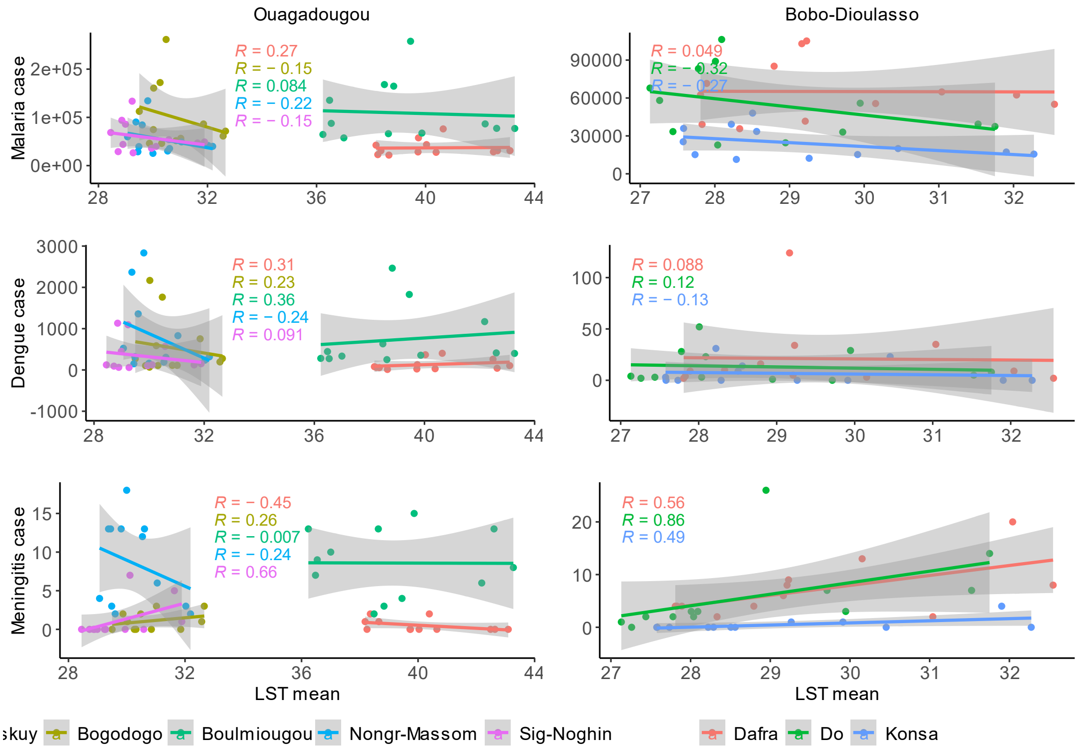

Figure 4.27: Correlation Between Surface Temperature and Diseases

4.1.5. Future LULC and LST patterns

4.1.5.1. *Driving variables for LULC changes*

The LULC changes driver variables considered for the prediction were composed of distance from river, distance from road, distance from urban, elevation, slope and evidence likelihood for Ouagadougou (Figure 4.28) and Bobo-Dioulasso (Figure 4.29). These variables were considered to run the transition potentials different LULC classes.

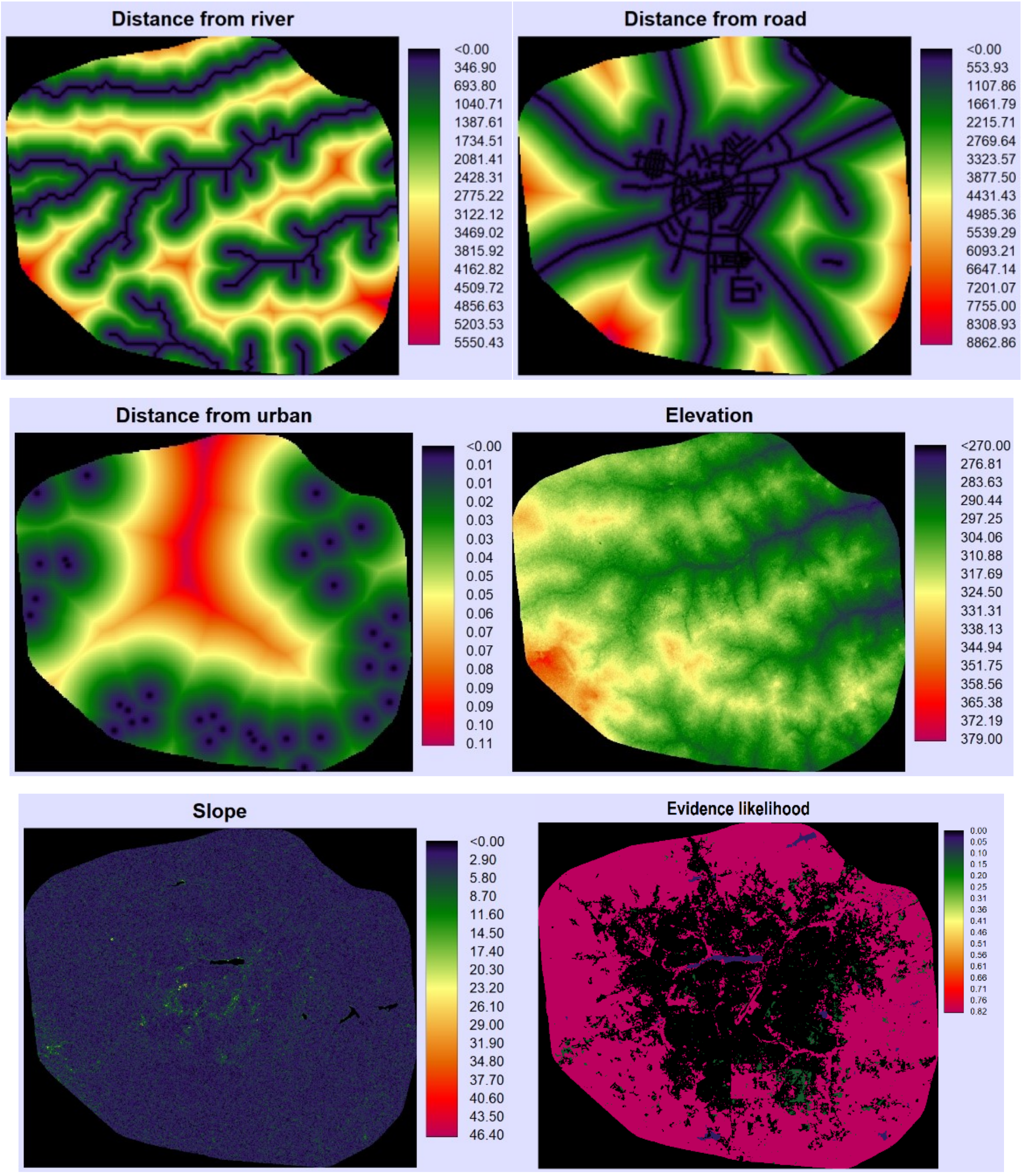

Figure 4.28: LULC Change Driver Variables in Ouagadougou

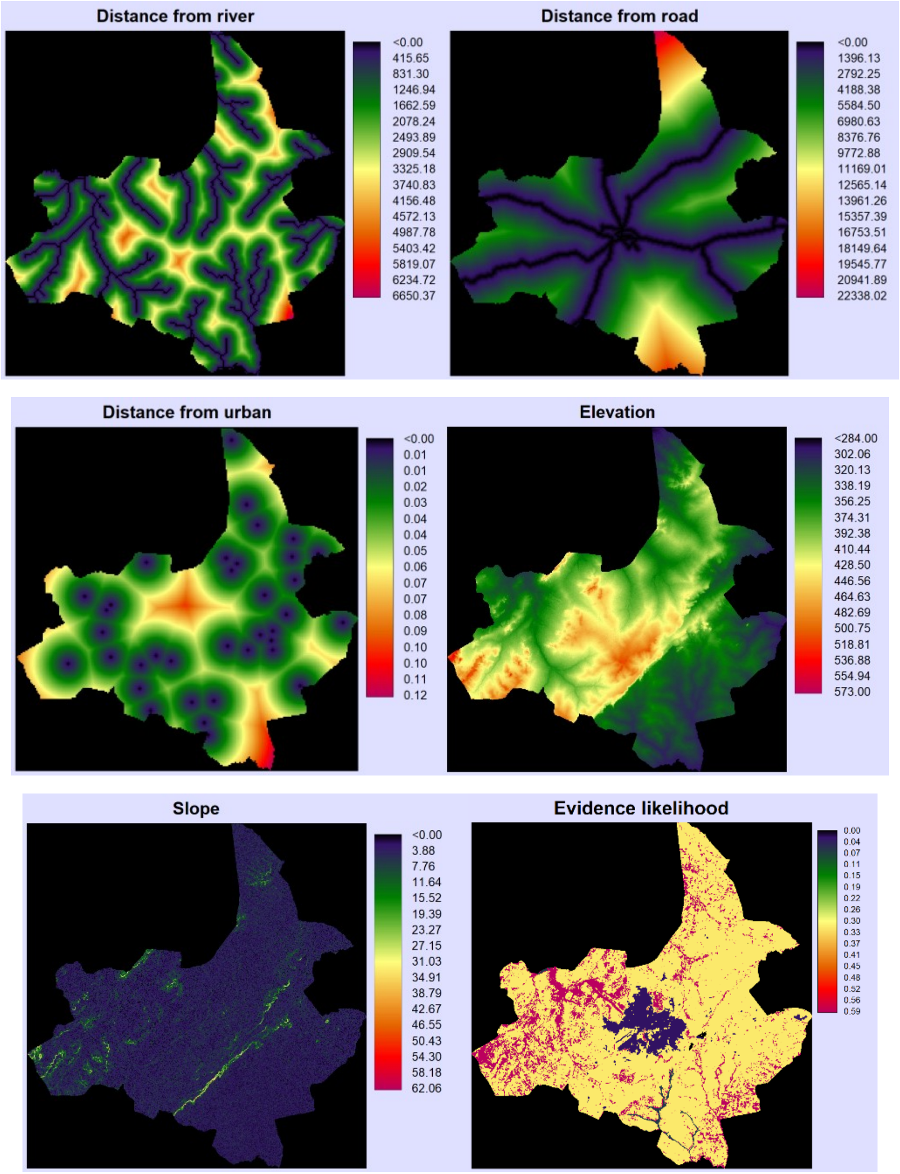

Figure 4.29: LULC Change Driver Variables in Bobo-Dioulasso

4.1.5.2. *Model validation*

To validate the MLP-NN-MC model, the LULC maps of 2021 were simulated using the changes between 2009 and 2015. The accuracy assessment performed showed an overall accuracy (K_{no}) of 0.80 and 0.92 for Ouagadougou and Bobo-Dioulasso respectively. The model ability to identify correct locations of changes ($K_{locality}$) was evaluated at 0.75 for Ouagadougou and 0.92 for Bobo-Dioulasso.

Though there are some discrepancies between the simulated and classified maps of 2021, the accuracy values achieved indicate that the model performs well in predicting future

LULC changes. Figure 4.30 presents the classified and simulated maps for 2021 in Ouagadougou (4.30a) and Bobo-Dioulasso (4.30b).

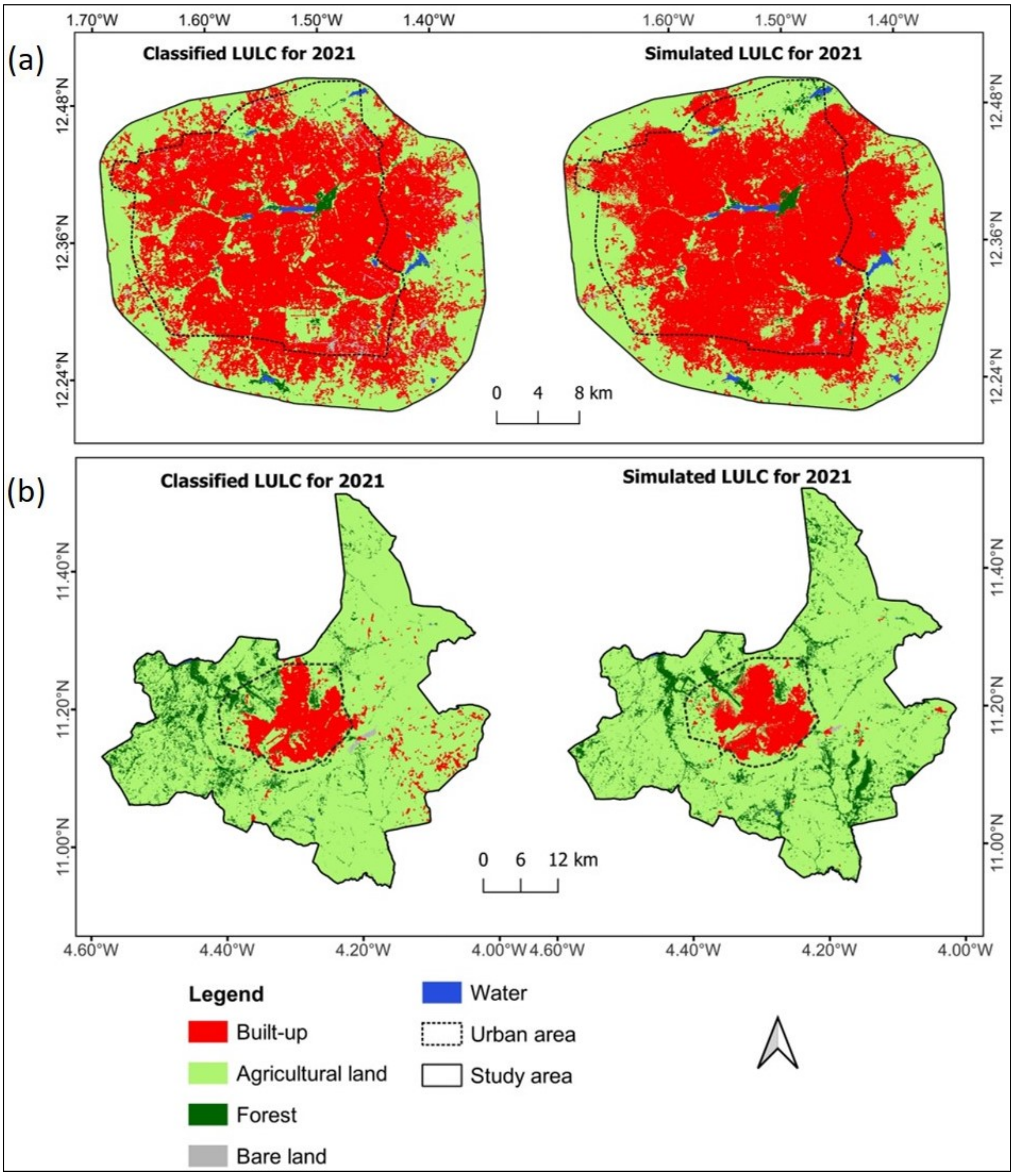

Figure 4.30: Classified and Simulated LULC for 2021 in Ouagadougou (a) and Bobo-Dioulasso (b)

The comparison between the classified and simulated maps of 2021 showed an underestimation of built-up and bare land areas, while agricultural lands were overestimated in both cities (Table 4.10). The model revealed a decreased in forested area in Ouagadougou against an increase in Bobo-Dioulasso.

Table 4.10: Area Statistics of Classified and Simulated LULC of 2021

Ouagadougou

LULC class	**2021 classified**		**2021 simulated**		**Difference**	
	km²	**%**	**km²**	**%**	**km²**	**%**
Built-up	566.00	58.34	560.55	57.78	-5.45	-0.56
Agricultural	366.67	37.79	386.06	39.79	19.39	1.99
Forest	12.22	1.26	11.84	1.22	-0.38	-0.04
Bare land	19.24	1.98	3.85	0.39	-15.40	-1.58
Water	5.98	0.61	7.82	0.80	1.84	0.119

Bobo-Dioulasso

LULC class	**2021 classified**		**2021 simulated**		**Difference**	
	km²	**%**	**km²**	**%**	**km²**	**%**
Built-up	175.33	9.86	143.54	8.07	-31.80	-1.79
Agricultural	1434.01	80.69	1436.30	80.82	2.29	0.13
Forest	163.33	9.19	195.06	10.97	31.72	1.78
Bare land	3.44	0.19	1.23	0.07	-2.22	-0.12
Water	1.04	0.05	1.04	0.06	0.00	0.00

Source: Author’s data analysis (2023)

4.1.6. Future LULC patterns

The projection of LULC under the BAU scenario in both cities showed that the built-up class will continue to extend towards the peripheral areas. There will also be a persistence and densification of built-up areas in the inner city. Figure 4.31 shows the spatial distribution of the different LULC classes in 2027 and 2050 for both cities.

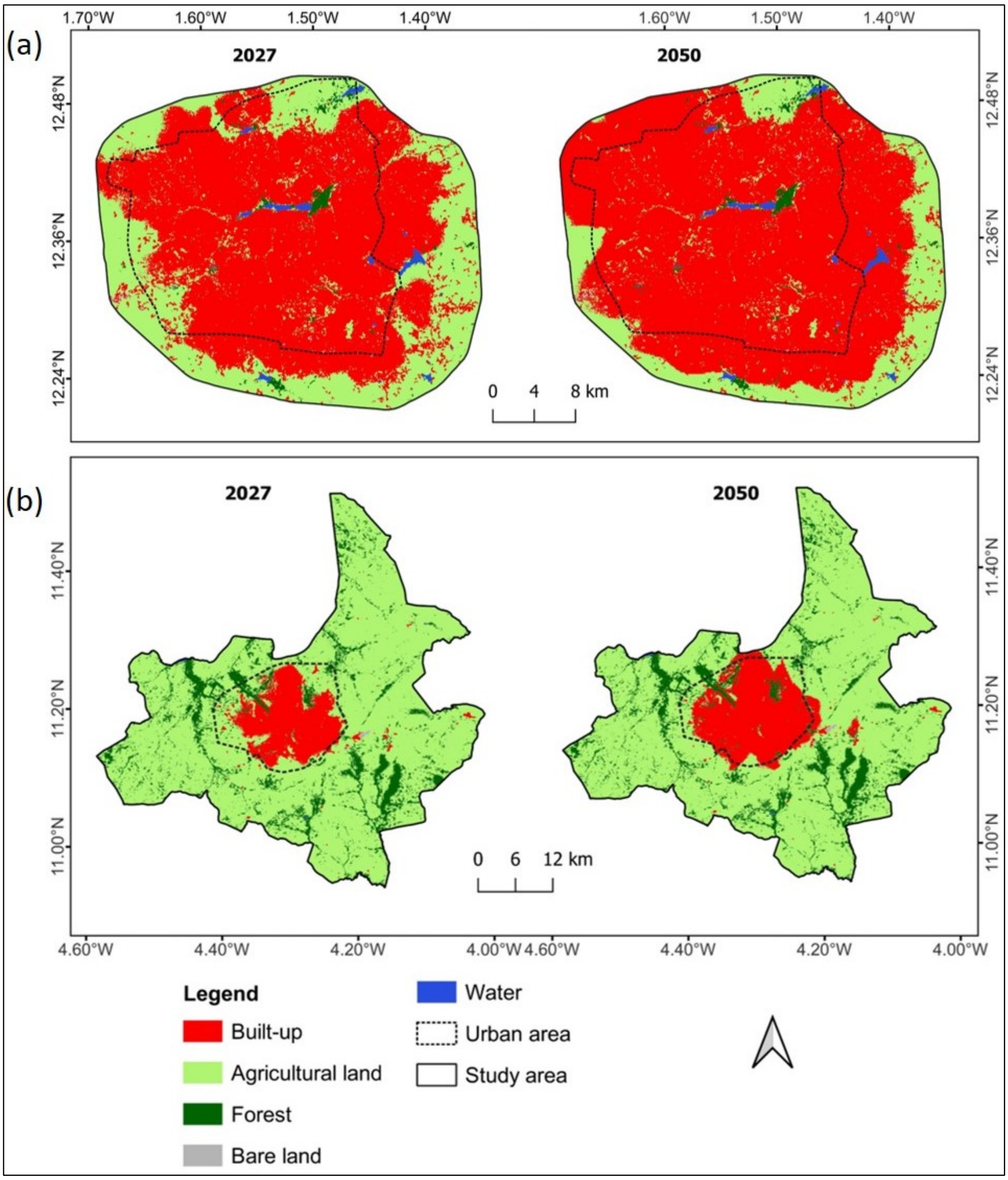

Figure 4.31: Predicted LULC for 2027 and 2050 Under BAU Scenario in Ouagadougou (a) and Bobo-Dioulasso (b)

The prediction of LULC based on the BAU scenario revealed that, in Ouagadougou, the landscape will be dominated by built-up class with 65.27 per cent of coverage in 2027 and 78.65 per cent in 2050 (Table 4.11). The increasing trend of built-up areas will be experienced at the expense of agricultural lands which will occupy only 19 per cent of the landscape in 2050. In Bobo-Dioulasso, the major future changes will concern the built-up class whose extent will increase and cover 9.56 per cent and 13.85 per cent of the area in 2027and 2050, respectively. As in Ouagadougou, agricultural class in Bobo-Dioulasso will decrease but remain the dominant class in 2050 with 73.74 per cent of coverage.

Table 4.11: Area Statistics of Predicted LULC of 2027 and 2050

LULC class	Ouagadougou			Bobo-Dioulasso		
	2027 (%)	**2050 (%)**	Δ %	**2027 (%)**	**2050 (%)**	Δ %
Built-up	65.27	78.65	13.38	9.56	13.85	4.29
Agricultural	32.45	19.09	-13.36	78.41	73.74	-4.67
Forest	1.22	1.22	0.00	11.89	12.27	0.38
Bare land	0.25	0.23	-0.01	0.07	0.07	0.00
Water	0.80	0.80	0.00	0.06	0.06	0.00

Source: Author's data analysis (2023)

4.1.7. Future LST patterns based on predicted LULC

Based on the predicted LULC for 2027 and 2050, the LST maps for the same years were generated using a multiple linear regression model. The regression models built based on the LST and LULC rate of the years 2003, 2009, 2015 and 2021 are presented in Equation (4.1) and Equation (4.2) respectively for Ouagadougou and Bobo-Dioulasso.

$$LST = 30.13 + 0.0073 \times built\_up - 0.0047 \times non\_built\_up + 0.68 \tag{4.1}$$

$$LST = 29.47 + 0.006 \times built\_up - 0.0014 \times non\_built\_up + 0.48 \tag{4.2}$$

The results of the LST prediction for 2027 and 2050 in the two cities are presented in Figure 4.32. The predicted LST showed an increase in 2027 and 2050 in both cities. The increase will be about 0.3°C and 0.14°C respectively for the periods 2021 – 2027 and

2027 – 2050 in Ouagadougou. In Bobo-Dioulasso, the increase was 0.32°C between 2021 and 2027 and 0.01°C for 2027 – 2050.

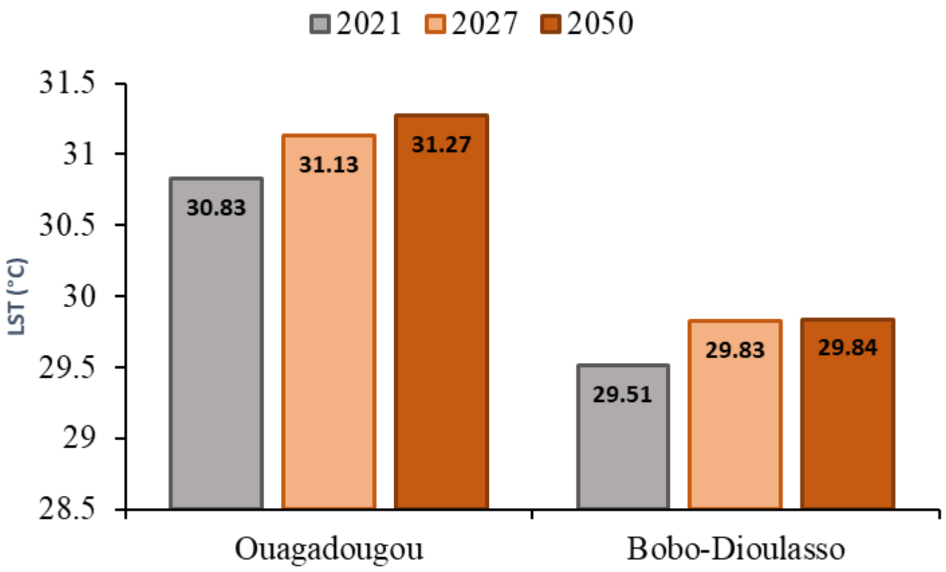

Figure 4.32: Trend in Mean LST for 2021, 2027 and 2050 Under the BAU Scenario in Ouagadougou and Bobo-Dioulasso

4.2. Discussions

4.2.1. LULC change in the study area

The analysis of LULC patterns revealed that the landscape experienced changes towards built-up area increase at the expense of agricultural lands (i.e., cultivated lands including seasonal, permanent crops and fallows, shrubland, grassland) and bare land in Ouagadougou and in Bobo-Dioulasso. These dynamics indicate ongoing urbanisation induced human footprint intensification in the areas.

The urbanisation process in the area is characterized by the horizontal expansion of the cities and an increasing population due to natural growth, rural-urban migration and smaller town to larger city migration. For example, it is estimated that in 2019, 45.1 per cent and 19.1 per cent of the country's total urban population lived in the Centre Region (with Ouagadougou as the biggest city) and the Haut-Bassins region (with Bobo-Dioulasso as biggest city), respectively (INSD, 2022a), with a net migration rate of 4 per cent per year in Ouagadougou (Sory, 2019). This rapid urban population growth could be one of the driving factors of the landscape changes, as rapid population increase causes high demand in land and consequently leads to LULC changes (Al Kafy *et al.,* 2019). The changes in LULC classes in favour of built-up areas were also recorded in other urban settings (Mahmoud *et al.,* 2016; Bhat *et al.,* 2017; Rimal *et al.,* 2018). Furthermore, the conversion of agricultural land to roads (a component in built-up class) causes the displacement of arborists with their trees to resettle along the road-faced walls of some administrations.

4.2.2. Built-up expansion in the study area

The city of Ouagadougou is experiencing a rapid settlement expansion (Figure 4. 33), while in Bobo-Dioulasso, the built-up area is rather increasing slowly (Figure 4.34). The cities have extended beyond their administrative boundaries into surrounding districts or villages, particularly in Ouagadougou. A similar situation was reported for Kumasi metropolitan city (Ghana), where urban development was found to have gone beyond its official boundaries (Hackman *et al.,* 2020). The expansion of built areas varies according to the district and is more and more pronounced towards the city outskirts. If the current situation remains unchanged, the built-up areas ‘expansion will continue towards the peripheral zones in 2027 and 2050. This result is in agreement with the study of Yangouliba *et al.* (2022) which concluded that built-up area will experience a continuous spatial growth up to 2050 under BAU scenario.

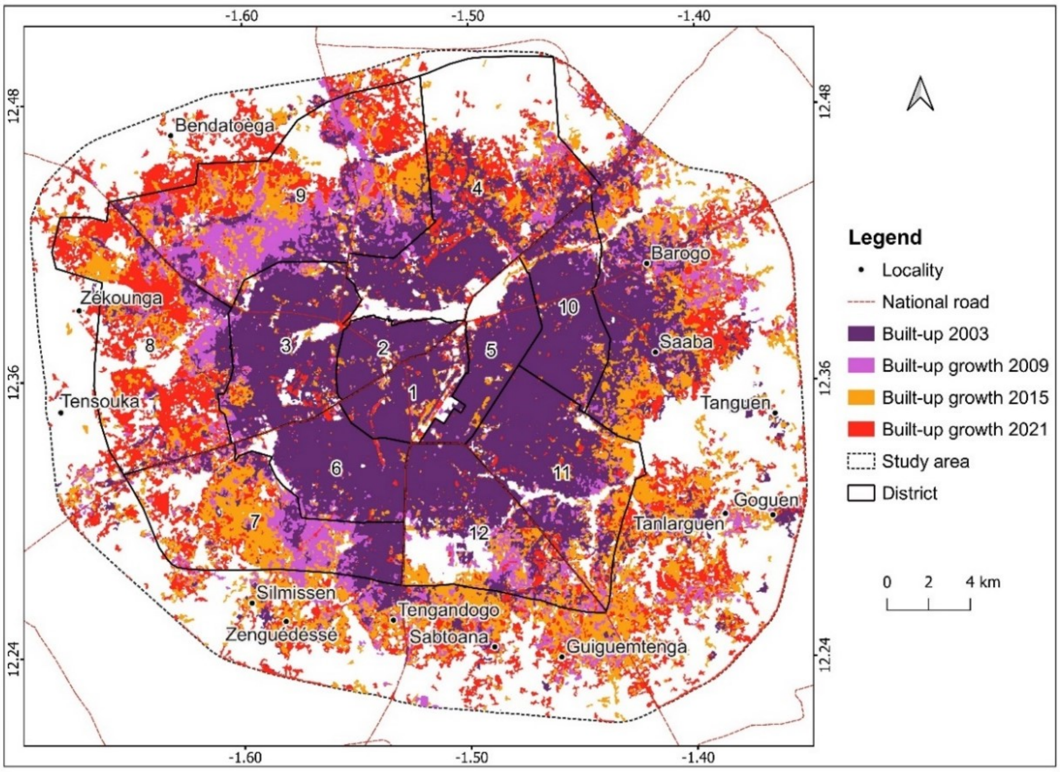

Figure 4.33: **Built-Up Expansion Between 2003 and 2021 in Ouagadougou**

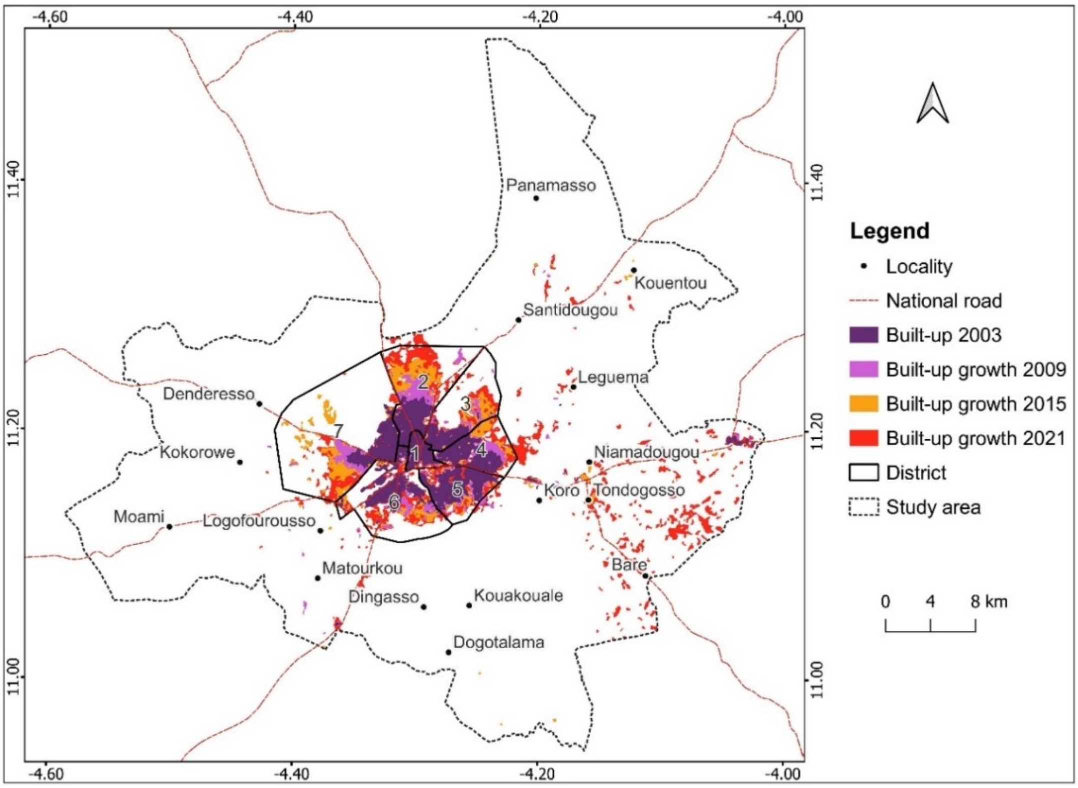

Figure 4.34: **Built-Up Expansion Between 2003 and 2021 in Bobo-Dioulasso**

Given the adverse effects of climate change, causing difficulties in finding alternative non-agricultural livelihood options, the rural population migrate to the cities to look for new sources of livelihood. Once in the city, not having resources to afford good housing, they settle in the peripheral slum' areas, making the city expand horizontally. Since new population is coming into the city, the number of inhabitants increased year by year. It is reported that Ouagadougou welcomes around 100,000 additional people per year (Boyer and Delaunay, 2009) and given the insufficient housing offer policy, most of the newcomers establish their houses in the peri-urban areas. This situation contributes to the development of informal neighbourhoods around the city.

Furthermore, since 2009 there is a land speculation process driven by private real estates companies. Indeed, with the authorizations from the government agencies, they buy land at low-cost prices from farmers in the peripheral areas, subdivide into plots and sell to individuals. From 2009 to 2019, a total of 275 land/real estate development approvals were issued to private companies (Sory, 2019). This context of high demand of land for construction linked to population growth leads to an increasing expansion of built-up areas (Niya *et al.,* 2019).

The rapid expansion of built- up areas has potential negative implications on urban agricultural production. This is because areas previously used for urban gardening, water pathways and urban green areas are being converted to concrete buildings. That conversion process also leads to an increase in impervious surfaces exposing the population to hazards such as flooding and Urban Heat Island (Gogoi *et al.,* 2019). In addition, the rapid urban settlement expansion has resulted in limited goods and services provision in the peripheral areas (Turok and McGranahan, 2013), highlighting the inadequacy between urban development and economic growth in most of the developing world's cities (Cohen, 2006). The World Bank revealed that in unplanned areas around cities, the quality of life is deteriorated due to the poor housing systems, insufficient road network, and inadequate water and sanitation supply (World Bank, 2002). This situation was also reported by the United Nations which stated that rapid urban growth and its inherent consequences are common phenomenon in many African cities because they are expected to record the highest growth rate in the coming 30 years (United Nations, 2018).

The LULC dynamics may have some uncertainties due to the low number of samples and the aggregation of some classes into one (as in the case of seasonal croplands, permanent croplands, fallow lands, shrublands and grasslands which were combined to form the agricultural land class). In this study, more samples were collected in Ouagadougou than Bobo-Dioulasso due to the limited availability of clear high-resolution historical images in Google Earth Pro. This situation may have affected the accuracy of the produced LULC maps, particularly for Bobo-Dioulasso, which showed low overall accuracies across the four years. In addition, the majority filtering bias is towards the classes labelled with least values (minimum values were returned in cases where there are no majority votes). However, the bias level is relatively low given the high accuracy values of the majority filtered images (> 80% in both sites), and the fact that the area is dominated by built-up (in Ouagadougou) and agricultural lands (in Bobo-Dioulasso).

Despite these limitations, this study is a valuable spatial decision tool in terms of LULC for regulating built-up expansion by promoting vertical building policy and preserving natural surfaces within urban areas. Given the increasing population growth in urban areas which increases the housing demand, a low-income housing policy could mitigate urban sprawl. The use of high spatial resolution images with more reference samples can improve the accuracies and allow more detailed LULC classification in the area.

4.2.3. LST and air temperature relationship in the study area

4.2.3.1. *Trends in LST and air temperature in the study area*

The rapid urbanisation occurring in the study leads to a modification of the thermal conditions of surface materials which causes an unbalanced energy budget over urban areas. Consequently, LST values are increasing, mainly in urban core where the surface is covered by impervious materials. The findings from this research showed that LST is continuously increasing in both cities. LST showed an increasing trend, which is naturally greater in Ouagadougou, the most urbanised area of the country, than Bobo-Dioulasso. The continuous increase of LST in the urban area was particularly persistent in the city centre where consistent heat island was formed because of the dominance of impervious surfaces. Conversely, the peripheral areas, mainly occupied by non-concrete surfaces including cultivated lands including seasonal, permanent crops and fallows, shrubland

and grassland, exhibited a relatively low LST values. Unsurprisingly, the positive trend of LST in both cities will continue as the LULC is changing towards the expansion and densification of built-up areas. The results of this study are in line with the global LST trend, which increased by 0.2°C per decade during the past 25 years (ESA, 2022). They are in agreement with the studies of Tafesse and Suryabhagavan, (2019) and Singh *et al.* (2017) which showed that the development of impervious surfaces at the expense of vegetation due to urbanisation leads to increases in LST in the urban core. These findings are also in line with results from similar studies on urban LST patterns in Nigeria (Fashae *et al.,* 2020) and in Ghana (Stemn and Kumi-Boateng, 2020) which highlighted that LST in the urban core is higher than the peripheral areas. Moreover, these results also confirm the findings of Di Leo *et al.* (2016) who concluded that LST values are lower in vegetated areas than adjacent impervious lands.

The seasonal patterns showed that the global increase of LST throughout the study period is driven by the March-April-May (MAM) season. This is because the MAM season corresponds to the dry and hot periods in the region where the net radiation is greater in the inner city, because of general clear sky conditions, and particularly the low surface reflectance due to the predominance of high heat storage materials (Offerle *et al.,* 2005).

Like the LST, the 2 meters above ground temperature also experienced an increasing trend between 2003 and 2021 in both study sites. The increasing air temperature in both sites is in agreement with regional and global studies, which showed rising average temperatures in the area (Ilori and Ajayi, 2020; IPCC, 2021). The inherent consequences of urbanisation such as population growth and LULC changes towards built-up surfaces, caused an increase of Greenhouse gas emission in the atmosphere. In fact, the use of fossil fuel (for energy production, transportation, factories), the production of waste, and domestic heating contribute to increase the urban environmental temperature, as found by Rimal *et al.* (2017).

4.2.3.2. *Trends in SUHI in the study area*

The high increase of LST in urban core compared to the surrounding areas causes an intensification of SUHI. The results of this research showed that SUHI intensity values increased towards the inner cities. This situation could be explained by the presence of administrative, business and habitation areas, which operate mainly on concrete and water-resistant surfaces. This finding agrees with that of Simwanda *et al.* (2019) who concluded that in growing cities in Africa , the CBDs exhibit high SUHI intensities. In the CBD area, large high thermal capacity surfaces are exposed to solar heating because of the vertical structure of buildings, while the peripheral rural areas heat rapidly with a limited heat storage due to low heat capacity as showed by Offerle *et al.* (2005).

Similar results were found by Dewan *et al.* (2021) who demonstrated that the major drivers of SUHI increase in the urban core included insufficiency of vegetation and expanded built-up cover. At night-time, the water bodies and wetlands showed high SUHI, while vegetated areas presented a low SUHI, because of the high heat capacity of water, which takes long time to absorb the heat and releases it back slowly in the atmosphere. These findings agrees with the result of Lindén (2011), which concluded that open water contributes to daytime cooling, while evapotranspiration from vegetation is responsible for night time cooling. Furthermore, Mirzaei *et al.* (2020) showed that water bodies and vegetation contribute to regulating the surface temperature and consequently the air temperature in urban settings.

Urban areas comprise complex landscapes of different size materials which record different LST values. A limitation of the study is related to the coarse spatial resolution of MODIS data (1000 m) used which did not allow a detailed mapping to extract the LST values of smaller urban surface units.

Nevertheless, this research showed the areas where LST is high and those with low values in the study area and in urban settings in general. Like air temperature, LST and SUHI increase constitute a threat to urban environment and inhabitants. Then, LST and SUHI mitigation strategies should be developed through the development of non-concrete surfaces in urban core areas mainly, to reduce the LST differences with the surroundings.

4.2.3.3. *Correlation between LST and air temperature*

In the study area, LST was higher than 2 m above ground air temperature, and the 2 variables had a strong positive correlation, meaning that when LST increases, air temperature also increases. It is found in literature that LST is often higher than the ambient air temperature measured by weather stations and felt by humans (Heat and Protocol, 2015), but the two variables vary at the same direction and have a positive correlation (Guha *et al.,* 2020). The average difference between the LST and air temperature (Δ) is relatively higher in Ouagadougou (1.42°C) than Bobo-Dioulasso (1.38°C). Δ is driven by shortwave incoming solar radiation, soil moisture, vegetation cover and therefore the partitioning of energy into Latent Heat Flux (LHF) and Sensible Heat Flux (SHF) (Forzieri *et al.,* 2018). Thus, the lower the average SHF, the lower the LST and consequently Δ. The cities are located in low latitudes and are all constantly exposed to quasi-vertical incidence of solar radiation throughout the year, which implies high average LST and air temperature as showed by Gogoi *et al.* (2019). In addition, the quasi-similarity of Δ in the two cities could be explained by the fact that both experience the same climatic conditions, except that Bobo-Dioulasso has less built-up cover indicating a higher LHF than Ouagadougou (Figure 4.35).

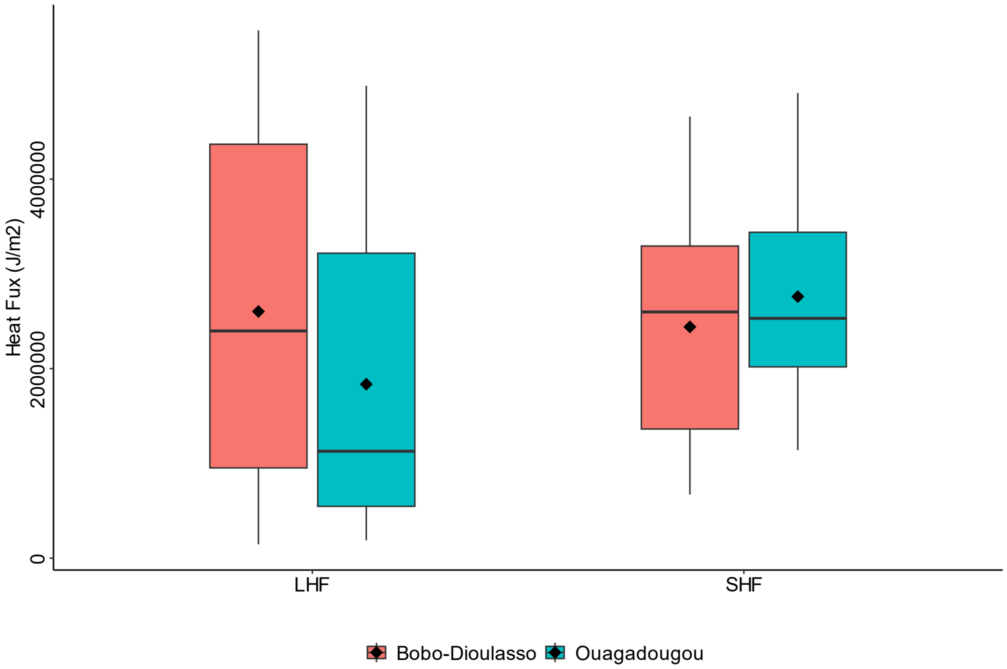

Figure 4.35: Partition of Energy in Latent and Sensible Heat Fluxes in the Study Area

Air temperature gets more and more warmer due to Greenhouse gases accumulation in the atmosphere. The positive correlation found between LST and 2 m above ground air temperature shows that the surface thermal conditions can contribute to increase air temperature. This finding is then a key information for policy implementation towards LST mitigation to avoid urban atmospheric warming intensification.

4.2.4. Relationship between LULC rate and LST

LULC changes influence LST so that concrete surfaces exhibit high values compared to naturally undisturbed areas. Therefore, areas where the human footprint is high in terms of built-up surfaces, record high LST values while zones with natural cover show low LST. The findings from this study showed that the patterns of LST in both cities is mainly dependent on the LULC types and dynamics, which modify the surface thermal properties through the increase of built-up areas. LST increased while the proportion of built-up increased in a pixel. This could be explained by the increasing of low albedo materials (for instance, building, pavement, asphalt for tarred roads) at the surface, implying low reflection of incident radiation as confirmed by Andrés-Anaya *et al.* (2021). Indeed, between 2017 and 2020, 130 km and 8 km of tarred roads were planned to be built in Ouagadougou and Bobo-Dioulasso respectively (PNDES, 2016). These results corroborate that of Simwanda *et al.* (2019), who found in Lagos (Nigeria), Lusaka (Zambia), Nairobi (Kenya) and Addis Ababa (Ethiopia) that cities having high proportion of impervious surfaces such as built-up were the warmest. In addition, other variables such as decrease of vegetation cover and soil moisture (reduction of water body, increased runoff) have the potential to reduce the LHF and consequently increase the SHF resulting in an increase of LST (Mitchell, 2011; Kandel, 2015; Jiang *et al.,* 2015).

Built-up surfaces were positively correlated with LST for Ouagadougou and Bobo-Dioulasso. Previous studies which assessed the link between LST and NDBI also found a positive correlation (Pal and Ziaul, 2017; Imran *et al.,* 2021). The correlation coefficient value decreased from 2003 to 2021 in Ouagadougou and Bobo-Dioulasso, meanwhile the LST values increased. This could be explained by the fact that there is an expansion of built-up area towards the city's outskirts and these surfaces are mixed with natural landscape having less heat capacity. Then, although considered as built-up areas in the classification given the pixel size, they have low LST values because the LST is the average skin temperature of the different LULC units at the pixel level (built-up fraction is low at the periphery of the city). This result is in line with that of Dissanayake *et al.* (2019) who found that impervious surfaces are key contributors to LST increase and its fraction declines from the city centre to the surrounding areas. On the contrary, non-built-up areas showed a negative correlation with LST during the study period. This result is in agreement with other studies which related LST and LULC using spectral indices such as NDVI and NDWI, and found a negative correlation (Guha *et al.,* 2020; Imran *et al.,* 2021; Shi *et al.,* 2021).

In both study sites, the correlation strength between non-built-up rate and LST decreased as in the case of built-up areas. This situation could be explained by the influence of surrounding built-up surfaces on the non-built-up areas' LST. Indeed, the non-built landscape mainly occupied by agricultural, forest and water bodies are affected by the neighbouring built-up areas which absorb and reemit huge amounts of heat in the atmosphere. This findings agree with that of Alavipanah *et al.* (2015) who noted that the LST within urban vegetation areas is influenced by LST in the surrounding built-up areas.

In terms of cooling effect, the non-built-up classes' contribution was significant during the study time span. The contribution to urban cooling of non-built-up areas was non-linear in Bobo-Dioulasso, unlike Ouagadougou. Nevertheless, an increase in cooling was produced while the non-built-up cover rate within a pixel increased. This is in line with the studies of Di Leo *et al.* (2016) and Shi *et al.* (2021) which showed that non-built-up classes such as vegetation can attenuate the warming effects of built-up surfaces. In Germany, Alavipanah *et al.* (2015) also demonstrated that strong cooling effect was observed in areas with more vegetation coverage.

These findings clearly show that built-up expansion is the main driver of LST increase in the study area. This is one more raison of the negative influence of urban sprawl on the environment. It can be used to promote LULC policy which integrates non-built-up surfaces development or restauration, particularly in the urban core where built-up proportions are the highest.

4.2.5. Correlation between LST and selected public diseases

LST increase and its inherent SUHI deteriorate urban dwellers thermal comfort and create a suitable environment for temperature-related diseases prevalence. This research found that the peak occurrence of malaria and dengue corresponds to the dry season, immediately after the rainy season. In the urban area, malaria occurs at any time during the year, because of the persistence of SUHI, which keeps the surface warm enough to favour the development of the diseases-carrying vector. For example, the malaria vector can survive and evolve under temperatures between 20 to 25°C (Chastel, 2006). A similar situation is applicable to dengue that has a rapid development when the temperature is between 30 to 35°C. Despite the absence of established direct relationship between the temperature rise and diseases prevalence such as malaria and dengue, the increase of urbanisation trend associated with the intensification of extreme weather events such as drought and floods could increase these diseases in Africa and Asia (Githeko *et al.,* 2000).

As for meningitis, the positive correlation with LST indicates that when the LST increases, the number of reported cases also increase, particularly during the dry season (February, March, April, October). This is in line with the pattern of meningitis regarding air temperature, as shown by Chen *et al.* (2022). Considering that the LST influences the air temperature by contributing to its increase, LST could also contribute to intensify meningitis outbreak. The impact of LST on public health can be summarized as follow: the emission of heat after sunset creates a suitable ecological environment for the vectors of certain diseases to develop. For example, the malaria vector likes a warm environment because when the heat emitted by the surface heats the water spots, it creates a liveable environment for the vector. That situation leads to extension in the lifespan of the vector in the year, since the urban surface is getting much warmer and Greenhouse effect is increasing. On the horizon 2050, LST values will continue to increase and then have a consequent influence on diseases prevalence in the study area.

A limitation of this assessment of the correlation between LST and diseases is the use of district level aggregated data instead of patient based. Although that limitation, the findings show a strong correlation between LST and meningitis prevalence in Bobo-Dioulasso. This result can serve as guide to the Ministry of Health to investigate in detail the link between LST and meningitis.

4.3. Summary of Key Findings

From the foregoing discussions, the following were observed:

i. The dominant LULC class in Ouagadougou is built-up areas, indicating an expansion of residential areas. In Bobo-Dioulasso, conversely, agricultural areas were dominant, even if they experienced a non-steady trend during the study period. The intensity analysis showed that Ouagadougou experienced a fast annual change intensity between 2015 and 2021, whereas in Bobo-Dioulasso, a fast change in intensity was recorded during the period 2009 – 2015. The main transitions were towards built-up surfaces at the expense of agricultural and bare lands in both sites.

ii. The future projection results showed that, under BAU scenario in both cities, the built-up areas will continue to expand towards the peripheral zones at the expense of agricultural and forest areas in 2050.

iii. The comparative trend analysis of LST and air temperature showed an increasing trend of both variables in the two cities. The global increase is driven by the March – April – May season, which presented a significant increase in Ouagadougou. So, this season is suitable for LST trend analysis in the region.

iv. The relationship analysis carried out revealed a stronger positive correlation between the LST and ambient temperature in Bobo-Dioulasso than Ouagadougou. The study also found that the SUHI presented high intensities in the urban core in both cities with higher night-time values in Ouagadougou. This tendency will continue in the future if the current LULC changes trend under the BAU persists in the area.

v. The correlation analysis between LULC changes and LST, revealed a positive correlation between LST and built-up areas, while non-built-up surfaces presented a negative correlation with LST in the study area. The non-built-up surfaces contribute to environmental cooling with a greater effect in Ouagadougou than Bobo-Dioulasso.

vi. The assessment of the link between LST and diseases showed that *Plasmodium falciparum* malaria and dengue cases have a weak correlation with LST in both cities. However, meningitis exhibited a moderate to strong positive correlation with LST, particularly in Bobo-Dioulasso. The increase in LST lead to an increase in meningitis prevalence. Thus, an increase in meningitis cases is expected in the future as the current trend of LST continues in both cities.

CHAPTER FIVE

5.0. CONCLUSION AND RECOMMENDATIONS

5.1. Conclusion

The research combined remote sensing, GIS and statistical data and analyses techniques to investigate the impacts of urbanisation induced LST in Ouagadougou and Bobo-Dioulasso, Burkina Faso.

The results showed that LULC changes during the study period was characterized by an expansion of built-up area, bare land, forest and water body, against a reduction of agricultural lands in Ouagadougou. In Bobo-Dioulasso, the built-up area, agricultural lands and bare land increased, while forest and water body decreased. In Ouagadougou, the increase in built-up area (78.13 per cent and bare land combined with the reduction of agricultural lands (42.25 per cent) indicated the advanced state of imperviousness of the area. In Bobo-Dioulasso also, in addition to an increase in built-up area (140.7 per cent), the degradation of forested areas is evidence of human footprint expansion in the area. Under the BAU scenario, built-up areas will continue to expand and cover about 78 per cent and 13 per cent of the landscape in 2050 respectively in Ouagadougou and Bobo-Dioulasso. The intensity analysis showed that Ouagadougou experienced greater annual change intensity, which peaked in the 2015-2021 period with 3.61 per cent of landscape area change per year. In Bobo-Dioulasso the maximum change intensity was recorded in 2009-2015 with 2.22 per cent of area change per year. The transition of changes was towards built-up surfaces, at the expense of bare and agricultural lands in both cities.

The assessment of LST patterns indicated an increasing trend with a persistent heat island in Ouagadougou and Bobo-Dioulasso from 2003 to 2021. The seasonal analysis showed an increase of LST in the MAM and SON seasons, while the DJF and JJA seasons saw a decrease in LST in both cities during the study period. The yearly LST increase during the period was driven by the MAM season, which showed a statistically significant trend in Ouagadougou against a non-significant trend in Bobo-Dioulasso. Strong UHI intensity was noted in the inner city, mainly during night-time in Ouagadougou. Meanwhile, the LST values were strongly correlated with the air temperature values throughout the study time span with a greater correlation coefficient in Bobo-Dioulasso (R=0.83) than Ouagadougou (R=0.76). Concretely, LST and air temperature increased in the area, while LST contributed positively to the air temperature trend.

The relationship between the LULC change and LST in the two cities, at pixel scale, showed a moderate to high positive correlation with built-up proportion, while the non-built-up class rate was negatively correlated. The difference in LST between a fully built-up pixel and a fully non-built-up pixel varied between 1.47°C and 1.87°C in Ouagadougou against 1.02°C and 1.27°C in Bobo-Dioulasso. This difference in values experienced gradual decreases from 2003 to 2021 in both cities, showing that LST in all LULC classes increased. In terms of cooling effects, the non-built classes contribution varied according to the sites during the four years (2003, 2009, 2015 and 2021). It was lower in Bobo-Dioulasso (0.29 - 1.39°C) than in Ouagadougou (0.74 - 1.94°C). The highest contribution of non-built class to cooling was recorded in 2009 in Ouagadougou and in 2003 in Bobo-Dioulasso.

The analysis of the correlation between *Plasmodium falciparum* malaria, dengue and meningitis cases and LST showed strong to negligible correlation according to the disease. *Plasmodium falciparum* malaria and dengue had a weak to negligible correlation with LST in the two cities. For meningitis, the correlation was moderate in the districts of Dafra and Konsa (Bobo-Dioulasso) and Sig-Noghin (Ouagadougou). Only the district of Do in Bobo-Dioulasso presented a strong correlation with the LST. With LST predicted to continue increasing into the future, the prevalence of these diseases (especially meningitis) may increase.

5.2. Recommendations

Based on the findings of the study, the following recommendations are suggested. They are made for policy improvement, performance improvement, and for further research.

The LULC changes were dominated by built-up gain at the expense of naturally undisturbed areas, with higher change intensity in Ouagadougou than Bobo-Dioulasso. The same tendency of change will continue in 2027 and 2050 if the current situation persists under the business-as-usual scenario. This LULC change profile causes the multiplication of water resistant and high solar radiation absorbers materials in the area, leading to an increase in LST. The LULC maps produced for Ouagadougou and Bobo-Dioulasso should serve as decision making tools that would inform the urban planners in both cities of the rate at which land conversion into built-up surfaces occur. Consequently, the Ministry in charge of Urban Planning can use these findings to improve the housing policy in Burkina Faso. Rather than allowing individual housing, which contribute to urban sprawl, LST increase and are not affordable for low-income people, the Ministry can promote and implement collective low-income green housing developments. This policy will allow more people to afford houses and will contribute to mitigate urban sprawl and LST.

The SUHI exhibited strong intensity values in the urban core, from 1 to 6 km and 1 to 3 km from the centre respectively in Ouagadougou and Bobo-Dioulasso. The difference in LST between a pixel fully covered by built-up and a pixel covered by non-built-up area decreased, indicating an increase in all LULC classes. In addition, LST increase lead to air temperature increase in the two cities. These findings can inform the Ministry in charge of Urban Planning to integrate non-urban landscape development in real estate project implementations to mitigate LST. The Ministry of Environment should ensure that real estates development agencies incorporate green areas such as street trees and house trees to increase non-built-up surfaces cover in urban settings. Moreover, afforestation activities should be conducted in urban areas, instead of rural areas only, mainly along tarred road to cut off solar radiation with the hope of reducing the current and future LST in the two cities. These green activities will contribute to reduce the rate of built-up coverage per surface unit for LST and consequently air temperature mitigation, towards achieving sustainable cities.

Further research should be conducted on urban LST trend using longer historical datasets to be able to relate it to climate change. Future investigation could assess the long-term correlation between LST and air temperature for LST-air temperature complementation modelling. This study also suggests the use of detailed datasets on public diseases, in particular meningitis (data on each patient location) for a modelling of population vulnerability to LST.

5.3. Contribution to Knowledge

The study revealed that Ouagadougou experienced more rapid changes in LULC than Bobo-Dioulasso, with a maximum annual change intensity of 3.61 percent recorded between 2015 and 2021 as against 2.22 per cent in Bobo-Dioulasso for the period 2009 – 2015. The transition of changes was towards built-up areas, which gains targeted bare land and agricultural lands in both cities. This situation has led to the increase of built-up surface in Ouagadougou by 78.12 per cent, while 42.24 per cent of the agricultural land area was lost. However, in Bobo-Dioulasso, the built-up area has increased far more by 140.67 percent and the agricultural land areas experienced a gain of 1.38 per cent compared with the 2003 baseline.

Both cities experienced an increasing trend in LST and air temperature (z value >0) with a greater increase in Ouagadougou than Bobo-Dioulasso, due to urbanisation. The global yearly trend was supported by the March-April-May (MAM) season, which shows a statistically significant trend in Ouagadougou (p-value=0.009). The LST and air temperature exhibited a stronger correlation in Bobo-Dioulasso (R=0.83) than in Ouagadougou (R=0.76). In the study area, at the pixel level, the built-up proportion showed a moderate positive correlation with the LST ($0.44 \leq R \leq 0.64$ in Ouagadougou, $0.49 \leq R \leq 0.61$ in Bobo-Dioulasso), while the non-built-up proportion was negatively correlated with LST ($-0.41 \leq R \leq -0.6$ in Ouagadougou, $-0.49 \leq R \leq -0.59$).

The difference in LST between a fully built-up pixel and a fully non-built-up pixel decreased from 2003 to 2021 in both cities indicating that the LST increased in all LULC types throughout the study period. The contribution of the non-built-up class to urban cooling was lower in Bobo-Dioulasso (between 0.29°C and 1.39°C) than in Ouagadougou (between 0.74°C and 1.94°C). The research also found that malaria and dengue fever had a weak correlation with LST (R<0.4), while meningitis presented a moderate correlation in the districts of Dafra (R=0.56) and Konsa (R=0.49) in Bobo-Dioulasso) and Sig-Noghin (0.66) in Ouagadougou. Only the district of Do in Bobo-Dioulasso showed a strong correlation (R=0.86) with the LST. With projected increases in LST under the business-as-usual scenario, the prevalence of temperature-related diseases may increase.

In summary, the study area experienced an increase in human footprint, which contributed to the intensification the LST which is an environmental threat to urban dwellers. These findings constitute a useful decision support for sustainable urban planning. It is therefore recommended that afforestation should be vigorously pursued at all governmental levels to step down the LST in the two cities. While sponsored research should be carried out to deepen the knowledge on LST and epidemic in the nation.

REFERENCES

Abu, I. O., Szantoi, Z., Brink, A., Robuchon, M., & Thiel, M. (2021). Detecting cocoa plantations in Côte d'Ivoire and Ghana and their implications on protected areas. *Ecological Indicators*, *129*(September 2020), 107863. https://doi.org/10.1016/j.ecolind.2021.107863

Al Kafy, A., Al-Faisal, A., Mahmudul Hasan, M., Sikdar, M. S., Hasan Khan, M. H., Rahman, M., & Islam, R. (2019). Impact of LULC changes on LST in Rajshahi district of Bangladesh: A Remote Sensing approach. *Journal of Geographical Studies*, *3*(1), 11–23. https://doi.org/10.21523/gcj5.19030102

Alavipanah, S., Wegmann, M., Qureshi, S., Weng, Q., & Koellner, T. (2015). The role of vegetation in mitigating urban land surface temperatures: A case study of Munich, Germany during the warm season. *Sustainability (Switzerland)*, *7*(4), 4689–4706. https://doi.org/10.3390/su7044689

Aldwaik, S. Z., & Pontius, R. G. (2012). Intensity analysis to unify measurements of size and stationarity of land changes by interval, category, and transition. *Landscape and Urban Planning*, *106*(1), 103–114. https://doi.org/10.1016/j.landurbplan.2012.02.010

Ali, S. B., Patnaik, S., & Madguni, O. (2017). Microclimate land surface temperatures across urban land use/ land cover forms. *Global Journal of Environmental Science and Management*, *3*(3), 231–242. https://doi.org/10.22034/gjesm.2017.03.03.001

ANAM (2021). Rainfall and temperature data of Ouagadougou and Bobo-Dioulasso, from 1980 to 2021, Ouagadougou, Burkina Faso

Anderson, C. I., & Gough, W. A. (2018). Accounting for missing data in monthly temperature series: Testing rule-of-thumb omission of months with missing values. *International Journal of Climatology*, *38*(13), 4990–5002. https://doi.org/10.1002/joc.5801

Andrés-Anaya, P., Sánchez-Aparicio, M., del Pozo, S., & Lagüela, S. (2021). *Correlation of land surface temperature with IR albedo for the analysis of urban heat island*. 9. https://doi.org/10.3390/engproc2021008009

Appiah, D. O. (2016). *Geoinformation modelling of peri-urban land use and land cover dynamics for climate variability and climate change in the Bosomtwe district, Ghana*.

Asare, Y. M., Forkuo, E. K., Forkuor, G., & Thiel, M. (2020). Evaluation of gap-filling methods for Landsat 7 ETM+ SLC-off image for LULC classification in a heterogeneous landscape of West Africa. *International Journal of Remote Sensing*, *41*(7), 2544–2564. https://doi.org/10.1080/01431161.2019.1693076

Asgarian, A., Amiri, B. J., & Sakieh, Y. (2015). Assessing the effect of green cover spatial patterns on urban land surface temperature using landscape metrics approach. *Urban Ecosystems*, *18*(1), 209–222. https://doi.org/10.1007/s11252-014-0387-7

Badugu, A., Arunab, K. S., Mathew, A., & Sarwesh, P. (2022). Spatial and temporal analysis of urban heat island effect over Tiruchirappalli city using geospatial techniques. *Geodesy and Geodynamics*, *14*(3), 275–291.

https://doi.org/10.1016/j.geog.2022.10.004

Barbierato, E., Bernetti, I., Capecchi, I., & Saragosa, C. (2019). Quantifying the impact of trees on land surface temperature: A downscaling algorithm at city-scale. *European Journal of Remote Sensing*, *52*(sup4), 74–83. https://doi.org/10.1080/22797254.2019.1646104

Bartkowiak, P., Castelli, M., & Notarnicola, C. (2019). Downscaling land surface temperature from MODIS dataset with random forest approach over alpine vegetated areas. *Remote Sensing*, *11*(11), 1–19. https://doi.org/10.3390/rs11111319

Becker, F., & Zhao-Liang Li. (1995). Surface temperature and emissivity at various scales: Definition, measurement and related problems. *Remote Sensing Reviews*, *12*(3–4), 225–253. https://doi.org/10.1080/02757259509532286

Beucher, F. (2010). *Météorologie tropicale: Des alizés au cyclone*. 847 pp. Retrieved from http://preprod-sim-portail.meteo-h2.aw.atosorigin.com/content/2011/1/24826-48.pdf

Bhat, P. A., Shafiq, M. ul, Mir, A. A., & Ahmed, P. (2017). Urban sprawl and its impact on land use/land cover dynamics of Dehradun city, India. *International Journal of Sustainable Built Environment*, *6*(2), 513–521. https://doi.org/10.1016/j.ijsbe.2017.10.003

Bocquier, P. (2005). World urbanization prospects. *Demographic Research*, *12*, 197–236. https://doi.org/10.4054/DemRes.2005.12.9

Boori, M. S., Vozenílek, V., Balzter, H., & Choudhary, K. (2015). *Land surface temperature with land cover classes in ASTER and Landsat data. Journal of Remote Sensing & GIS*. *4*(1), 2–4. https://doi.org/10.4172/2169-0049.1000138

Boyer, F., & Delaunay, D. (2009). *« OUAGA. 2009 » Peuplement de Ouagadougou et développement urbain. Rapport provisoire*.

BREIMAN, L. (2001). Random Forests. *Machine Learning*, *45*(1), 5–32. https://doi.org/doi.org/10.1023/A:1010933404324

Byrne, M. P., Pendergrass, A. G., Rapp, A. D., & Wodzicki, K. R. (2018). Response of the intertropical convergence zone to climate change: Location, width, and strength. *Current Climate Change Reports*, *4*(4), 355–370. https://doi.org/10.1007/s40641-018-0110-5

Chang, T., Xiong, X., & Angal, A. (2018). *Terra and Aqua MODIS inter-comparison using LEO-GEO double difference method. September 2018*, 51. https://doi.org/10.1117/12.2325375

Chastel, C. (2006). Changements climatiques et maladies infectieuses - Climate change and infectious diseases. *La Lettre de l'Infectiologie*, *3*, 258–261.

Chen, J., Jiao, Z., Liang, Z., Ma, J., Xu, M., Biswal, S., Ramanathan, M., Sun, S., & Zhang, Z. (2022). Association between temperature variability and global meningitis incidence. *Environment International*, *171*(August 2022), 107649. https://doi.org/10.1016/j.envint.2022.107649

Cohen, B. (2006). Urbanization in developing countries: Current trends, future projections, and key challenges for sustainability. *Technology in Society*, *28*(1–2), 63–80. https://doi.org/10.1016/j.techsoc.2005.10.005

Congalton, R. G. (2015). Remote sensing and image interpretation. 7th Edition. *Photogrammetric Engineering & Remote Sensing*, *81*(8), 615–616. https://doi.org/10.14358/PERS.81.8.615

Cracknell, M. J., & Reading, A. M. (2014). Geological mapping using remote sensing data: A comparison of five machine learning algorithms, their response to variations in the spatial distribution of training data and the use of explicit spatial information. *Computers and Geosciences*, *63*, 22–33. https://doi.org/10.1016/j.cageo.2013.10.008

Dadhich, P. N., & Hanaoka, S. (2011). Spatio-temporal urban growth modeling of Jaipur, India. *Journal of Urban Technology*, *18*(3), 45–65. https://doi.org/10.1080/10630732.2011.615567

Dash, P., Göttsche, F. M., Olesen, F. S., & Fischer, H. (2002). Land surface temperature and emissivity estimation from passive sensor data: Theory and practice-current trends. *International Journal of Remote Sensing*, *23*(13), 2563–2594. https://doi.org/10.1080/01431160110115041

Deng, Y., Wang, S., Bai, X., Tian, Y., Wu, L., Xiao, J., Chen, F., & Qian, Q. (2018). Relationship among land surface temperature and LUCC, NDVI in typical karst Area. *Scientific Reports*, *8*(1), 1–12. https://doi.org/10.1038/s41598-017-19088-x

Deng, Z., & Quan, B. (2022). Intensity characteristics and multi-scenario projection of land use and land cover change in Hengyang, China. *International Journal of Environmental Research and Public Health*, *19*(14). https://doi.org/10.3390/ijerph19148491

Dewan, A., Kiselev, G., Botje, D., Mahmud, G. I., Bhuian, M. H., & Hassan, Q. K. (2021). Surface urban heat island intensity in five major cities of Bangladesh: Patterns, drivers and trends. *Sustainable Cities and Society*, *71*(April), 102926. https://doi.org/10.1016/j.scs.2021.102926

Di Gregorio, A., Jansen, L. J. M., & Di Gregorio, A., and Jansen, L. J. M. (2000). Land Cover Classification System (LCCS): Classification concepts and user manual. *FAO*, *53*(May), 179.

Di Leo, N., Escobedo, F. J., & Dubbeling, M. (2016). The role of urban green infrastructure in mitigating land surface temperature in Bobo-Dioulasso, Burkina Faso. *Environment, Development and Sustainability*, *18*(2), 373–392. https://doi.org/10.1007/s10668-015-9653-y

Dissanayake, D., Morimoto, T., Murayama, Y., Ranagalage, M., & Handayani, H. H. (2019a). Impact of urban surface characteristics and socio-economic variables on the spatial variation of land surface temperature in Lagos city, Nigeria. *Sustainability (Switzerland)*, *11*(1), 1–23. https://doi.org/10.3390/su11010025

Dissanayake, D., Morimoto, T., Murayama, Y., & Ranagalage, M. (2019b). Impact of landscape structure on the variation of land surface temperature in Sub-Saharan region: A case study of Addis Ababa using Landsat data (1986-2016). *Sustainability (Switzerland)*, *11*(8). https://doi.org/10.3390/su11082257

Eastman, J. R. (2020a). *TerrSet 2020 Geospatial monitoring and modeling system, tutorial*. Clark University, Worcester, MA, USA. Retrieved from www.clarklabs.org clarklabs@clarku.edu

Eastman, J. R. (2020b). *TerrSet geospatial monitoring and modeling system, manual version 2020v.19.0*. Clark University, Worcester, MA, USA. Retrieved from www.clarklabs.org clarklabs@clarku.edu

Elliott, A., & Woodward, W. (2007). Statistical analysis quick reference guidebook. In *Statistical Analysis Quick Reference Guidebook*. https://doi.org/10.4135/9781412985949

Eresanya, E. O., Daramola, M. T., Durowoju, O. S., & Awoyele, P. (2019). Investigation of the changing patterns of the land use land cover over Osogbo and its environs. *Royal Society Open Science*, *6*(12). https://doi.org/10.1098/rsos.191021

ESA. (2022). *Increases in land surface temperature and water vapour analysed in new satellite data*. Retrieved from https://www.climatechangenews.com/2022/05/26/increases-in-land-surface-temperature-and-water-vapour-analysed-in-new-satellite-data/

Estoque, R. C., & Murayama, Y. (2017). Monitoring surface urban heat island formation in a tropical mountain city using Landsat data (1987–2015). *ISPRS Journal of Photogrammetry and Remote Sensing*, *133*, 18–29. https://doi.org/10.1016/j.isprsjprs.2017.09.008

Estoque, R. C., Ooba, M., Seposo, X. T., Togawa, T., Hijioka, Y., Takahashi, K., & Nakamura, S. (2020). Heat health risk assessment in Philippine cities using remotely sensed data and social-ecological indicators. *Nature Communications*, *11*(1), 1–12. https://doi.org/10.1038/s41467-020-15218-8

Exavier, R., & Zeilhofer, P. (2020). OpenLand: Software for quantitative analysis and visualization of land use and cover change. *R Journal*, *12* (December), 1–16. https://doi.org/10.32614/rj-2021-021

Faichia, C., Tong, Z., Zhang, J., & Liu, X. (2020). *Using RS data-based CA – Markov model for dynamic simulation of historical and future LUCC in Vientiane , Laos*. 1–20. https://doi.org/10.3390/su12208410

Farina, A. (2012). Exploring the relationship between land surface temperature and vegetation abundance for urban heat island mitigation in Seville, Spain. *LUMA-GIS Thesis Nr*, *15*, 50. Retrieved from http://lup.lub.lu.se/luur/download?func=downloadFile&recordOId=3460284&fileOId=3460402

Farr, T. G., Rosen, P. A., Caro, E., Crippen, R., Duren, R., Hensley, S., Kobrick, M., Paller, M., Rodriguez, E., Roth, L., Seal, D., Shaffer, S., Shimada, J., Umland, J., Werner, M., Oskin, M., Burbank, D., & Alsdorf, D. (2007). The Shuttle radar topography mission. *Reviews of Geophysics*, *45*(2), RG2004. https://doi.org/10.1029/2005RG000183

Fashae, O. A., Adagbasa, E. G., Olusola, A. O., & Obateru, R. O. (2020). Land use/land cover change and land surface temperature of Ibadan and environs, Nigeria. *Environmental Monitoring and Assessment*, *192*(2). https://doi.org/10.1007/s10661-019-8054-3

Fonseka, H. P. U., Zhang, H., Sun, Y., Su, H., Lin, H., & Lin, Y. (2019). Urbanization and its impacts on land surface temperature in Colombo Metropolitan area, Sri Lanka, from 1988 to 2016. *Remote Sensing*, *11*(8), 1–18. https://doi.org/10.3390/rs11080926

Forkuor, G., Conrad, C., Thiel, M., Landmann, T., & Barry, B. (2015). Evaluating the sequential masking classification approach for improving crop discrimination in the sudanian savanna of West Africa. *Computers and Electronics in Agriculture*, *118*(July 2018), 380–389. https://doi.org/10.1016/j.compag.2015.09.020

Forkuor, G., Dimobe, K., Serme, I., & Tondoh, J. E. (2018). Landsat-8 vs Sentinel-2: Examining the added value of Sentinel-2's red-edge bands to land-use and land-cover mapping in Burkina Faso. *GIScience and Remote Sensing*, *55*(3), 331–354. https://doi.org/10.1080/15481603.2017.1370169

Forkuor, G., & Maathuis, B. (2012). Comparison of SRTM and ASTER derived digital elevation models over two regions in Ghana - Implications for hydrological and environmental modeling. *Studies on Environmental and Applied Geomorphology*, *March*. https://doi.org/10.5772/28951

Forzieri, G., Alkama, R., Miralles, D. G., & Cescatti, A. (2018). Response to comment on "satellites reveal contrasting responses of regional climate to the widespread greening of Earth." *Science*, *360*(6394), 1180–1184. https://doi.org/10.1126/science.aap9664

Fourchard, L. (2003). Propriétaires et commerçants africains à Ouagadougou et à Bobo-Dioulasso (Haute- Volta), fin 19ème siècle–1960. *Journal of African History*, *44*(3), 433–461. https://doi.org/10.1017/S0021853703008466

Fu, P., & Weng, Q. (2016). A time series analysis of urbanization induced land use and land cover change and its impact on land surface temperature with Landsat imagery. *Remote Sensing of Environment*, *175*, 205–214. doi.org/10.1016/j.rse.2015.12.040

Gething, P. W., Smith, D. L., Patil, A. P., Tatem, A. J., Snow, R. W., & Hay, S. I. (2010). Climate change and the global malaria recession. *Nature*, *465*(7296), 342–345. https://doi.org/10.1038/nature09098

Ghasemi, A., & Zahediasl, S. (2012). *Normality tests for statistical analysis: A guide for non-statisticians*.

Gholamy, A., Kreinovich, V., & Kosheleva, O. (2018). Why 70/30 or 80/20 relation between training and testing sets : A pedagogical explanation. *Departmental Technical Reports (CS)*, *1209*, 1–6.

Giri, C. P. (2012). *Remote sensing of land use and land cover: Principles and applications* (Taylor & F).

Girma, R., Fürst, C., & Moges, A. (2022). Land use land cover change modeling by integrating artificial neural network with cellular automata-Markov Chain model in

Gidabo river basin, main Ethiopian rift. *Environmental Challenges*, *6*(December), 100419. https://doi.org/10.1016/j.envc.2021.100419

Githeko, A. K., Lindsay, S. W., Confalonieri, U. E., & Patz, J. A. (2000). Climate change and vector-borne diseases: A regional analysis. *Bulletin of the World Health Organization*, *78*(9), 1136–1147.

Gogoi, P. P., Vinoj, V., Swain, D., Roberts, G., Dash, J., & Tripathy, S. (2019). Land use and land cover change effect on surface temperature over Eastern India. *Scientific Reports*, *9*(1), 1–10. https://doi.org/10.1038/s41598-019-45213-z

Good, E. J. (2016). An in situ-based analysis of the relationship between land surface “skin” and screen-level air temperatures. *Nature*, *175*(4449), 238–238. https://doi.org/10.1038/175238c0

Gorelick, N., Hancher, M., Dixon, M., Ilyushchenko, S., Thau, D., & Moore, R. (2017). Google earth engine: Planetary-scale geospatial analysis for everyone. *Remote Sensing of Environment*, *202*(2016), 18–27. doi.org/10.1016/j.rse.2017.06.031

Guha, S., Govil, H., Gill, N., & Dey, A. (2020). Analytical study on the relationship between land surface temperature and land use/land cover indices. *Annals of GIS*, *26*(2), 201–216. https://doi.org/10.1080/19475683.2020.1754291

Güneralp, B., Lwasa, S., Masundire, H., Parnell, S., & Seto, K. C. (2017). Urbanization in Africa: Challenges and opportunities for conservation. *Environmental Research Letters*, *13*(1). https://doi.org/10.1088/1748-9326/aa94fe

Hackman, K. O., Li, X., Asenso-Gyambibi, D., Asamoah, E. A., & Nelson, I. D. (2020). Analysis of geo-spatiotemporal data using machine learning algorithms and reliability enhancement for urbanization decision support. *International Journal of Digital Earth*, *13*(12), 1717–1732. https://doi.org/10.1080/17538947.2020.1805036

Hamad, R., Balzter, H., & Kolo, K. (2018). Predicting land use/land cover changes using a CA-Markov model under two different scenarios. *Sustainability (Switzerland)*, *10*(10), 1–23. https://doi.org/10.3390/su10103421

Hauer, J., Østergaard Nielsen, J., & Niewöhner, J. (2018). Landscapes of hoping – urban expansion and emerging futures in Ouagadougou, Burkina Faso. *Anthropological Theory*, *18*(1), 59–80. https://doi.org/10.1177/1463499617747176

Heat, U., & Protocol, I. (2015). *Appendix D urban heat island protocol for mapping temperature projections*. *November*.

Huang, K., Li, X., Liu, X., & Seto, K. C. (2019a). *Projecting global urban land expansion and heat island intensification through 2050*. *14*.

Huang, K., Li, X., Liu, X., & Seto, K. C. (2019b). Projecting global urban land expansion and heat island intensification through 2050. *Environmental Research Letters*, *14*(11). https://doi.org/10.1088/1748-9326/ab4b71

Iacobellis, S. F., Norris, J. R., Kanamitsu, M., Tyree, M., & Cayan, D. C. (2009). *Climate variability and california low-level temperature inversions*. *August 2009*, 62. Retrieved from http://www.energy.ca.gov/2009publications/CEC-500-2009-020/CEC-500-2009-020-F.PDF

Indian Institute of Remote Sensing (2016). Land surface temperature studies in urban areas, Dehradun, India

Ilori, O. W., & Ajayi, V. O. (2020). Change detection and trend analysis of future temperature and rainfall over West Africa. *Earth Systems and Environment*, *4*(3), 493–512. https://doi.org/10.1007/s41748-020-00174-6

Imran, H. M., Hossain, A., Islam, A. K. M. S., Rahman, A., Bhuiyan, M. A. E., Paul, S., & Alam, A. (2021). Impact of land cover changes on land surface temperature and human thermal comfort in Dhaka city of Bangladesh. *Earth Systems and Environment*, *5*(3), 667–693. https://doi.org/10.1007/s41748-021-00243-4

INSD. (2006). *Theme 09: La croissance urbaine au Burkina Faso*.

INSD. (2022a). *Cinquième recensement général de la population et de l'habitation du Burkina Faso*.

INSD. (2022b). *Monographie de la commune de Bobo Dioulasso*.

INSD. (2022c). *Monographie de la commune de Ouagadougou*.

IPCC. (2013a). Climate change 2013: The physical science basis. Contribution of working group I to the fifth assessment report of the Intergovernmental panel on climate change. In *Cambridge University Press*.

IPCC. (2013b). *IPCC factsheet : What is the IPCC ?*

IPCC. (2014). *Climate change 2014:Impacts, adaptation and vulnerability: Part B: Regional aspects (Field, Christopher B. Barros, Vicente R. Dokken, David Jon Mach, Katharine J. Mastrandrea, Michael D. Bilir, T. Eren Chatterjee, Monalisa Ebi, Kristie L. Estrada, Yuka O.*

IPCC. (2019). Global warming of 1.5°C. An IPCC special report on the impacts of global warming of 1.5°C above pre-industrial levels and related global greenhouse gas emission pathways, in the context of strengthening the global response to the threat of climate change,. In *Nature* (Vol. 291, Issue 5813). doi.org/10.1038/291285a0

IPCC. (2021). Climate change 2021: The physical science basis. Contribution of working group I to the sixth assessment report of the Intergovernmental panel on climate change [Masson-Delmotte, V., P. Zhai, A. Pirani, S.L. Connors, C. Péan, S. Berger, N. Caud, Y. Chen, . In *Cambridge University Press* (Vol. 34, Issue 2). https://doi.org/10.1017/9781009157896

IPCC. (2023). Synthesis report. Contribution of working groups I, II and III to the sixth assessment report of the Intergovernmental panel on climate change. In *IPCC*. https://doi.org/doi: 10.59327/IPCC/AR6-9789291691647.

Jain, S., Sannigrahi, S., Sen, S., Bhatt, S., Chakraborti, S., & Rahmat, S. (2019). Urban heat island intensity and its mitigation strategies in the fast-growing urban area. *Journal of Urban Management*, *9*(1), 54–66. doi.org/10.1016/j.jum.2019.09.004

Jaiye, D. (2020). Climate change and smart city development: The challenge of non-implementation of Abuja-Nigeria light rail project. *Journal of Geography and Regional Planning*, *13*(1), 19–29. https://doi.org/10.5897/jgrp2020.0763

Jakubauskas, M. E., & Legates, D. R. (2000). Harmonic analysis of time-series AVHRR NDVI data for characterizing US great plains land use/land cover. *International Archives of Photogrammetry and Remote Sensing*, *33*(B4), 384–389.

Jiang, J., & Tian, G. (2010). Analysis of the impact of land use/land cover change on land surface temperature with remote sensing. *Procedia Environmental Sciences*, *2*, 571–575. https://doi.org/10.1016/j.proenv.2010.10.062

Jiang, Y., Fu, P., & Weng, Q. (2015). Assessing the impacts of urbanization-associated land use/cover change on land surface temperature and surface moisture: A case study in the midwestern United States. *Remote Sensing*, *7*(4), 4880–4898. https://doi.org/10.3390/rs70404880

Jin, M., & Dickinson, R. E. (2000). A generalized algorithm for retrieving cloudy sky skin temperature from satellite thermal infrared radiances. *Journal of Geophysical Research Atmospheres*, *105*(D22), 27037–27047. https://doi.org/10.1029/2000JD900318

Johnson, C., Affolter, M. D., Inkenbrandt, P., & Mosher, C. (2017). An introduction to geology. In *LibreTexts* (Vol. 13, Issue 5). https://doi.org/10.2307/2420180

Kafy, A. Al, Rahman, M. S., Faisal, A. Al, Hasan, M. M., & Islam, M. (2020). Modelling future land use land cover changes and their impacts on land surface temperatures in Rajshahi, Bangladesh. *Remote Sensing Applications: Society and Environment*, *18*(February), 100314. https://doi.org/10.1016/j.rsase.2020.100314

Kandel, H. (2015). Land use /land cover driven surface energy balance and convective rainfall change in South Florida. *FIU Electronic Theses and Dissertations*. https://doi.org/10.25148/etd.FIDC000102

Kayet, N., Pathak, K., Chakrabarty, A., & Sahoo, S. (2016). Spatial impact of land use/land cover change on surface temperature distribution in Saranda forest, Jharkhand. *Modeling Earth Systems and Environment*, *2*(3), 1–10. https://doi.org/10.1007/s40808-016-0159-x

Kloog, I., Nordio, F., Coull, B. A., & Schwartz, J. (2014). Predicting spatiotemporal mean air temperature using MODIS satellite surface temperature measurements across the northeastern USA. *Remote Sensing of Environment*, *150*, 132–139. https://doi.org/10.1016/j.rse.2014.04.024

Kotharkar, R., & Surawar, M. (2016). Land use, land cover, and population density impact on the formation of canopy urban heat islands through traverse survey in the Nagpur urban area, India. *Journal of Urban Planning and Development*, *142*(1), 04015003. https://doi.org/10.1061/(asce)up.1943-5444.0000277

Kou, X., Jiang, L., Bo, Y., Yan, S., & Chai, L. (2016). Estimation of land surface temperature through blending MODIS and AMSR-E data with the bayesian maximum entropy method. *Remote Sensing*, *8*(2). https://doi.org/10.3390/rs8020105

Kuddus, M. A., Tynan, E., & McBryde, E. (2020). Urbanization: A problem for the rich and the poor? *Public Health Reviews*, *41*(1), 1–4. https://doi.org/10.1186/s40985-019-0116-0

Kumar, K. S., Bhaskar, P. U., & Padmakumari, K. (2012). Estimation of land surface temperature to study urban heat island effect using Landsat ETM+ images. *International Journal of Engineering Science and Technology*, *4*(02), 771–778.

Kundu, S., & Kumar, N. (2016). Unit commitment problem by using jayaDE optimization algorithm. *2016 7th India International Conference on Power Electronics (IICPE)*, *2016-Novem*, 1–6. https://doi.org/10.1109/IICPE.2016.8079546

Leta, M. K., Demissie, T. A., & Tränckner, J. (2021). Modeling and prediction of land use land cover change dynamics based on Land change modeler (LCM) in Nashe watershed, upper blue Nile basin, Ethiopia. *Sustainability (Switzerland)*, *13*(7). https://doi.org/10.3390/su13073740

Li, H., Zhou, Y., Li, X., Meng, L., Wang, X., Wu, S., & Sodoudi, S. (2018). A new method to quantify surface urban heat island intensity. *Science of the Total Environment*, *624*, 262–272. https://doi.org/10.1016/j.scitotenv.2017.11.360

Li, X., Zhou, Y., Asrar, G. R., Imhoff, M., & Li, X. (2017). The surface urban heat island response to urban expansion: A panel analysis for the conterminous United States. *Science of the Total Environment*, *605–606*, 426–435. https://doi.org/10.1016/j.scitotenv.2017.06.229

Li, Z. L., Tang, B. H., Wu, H., Ren, H., Yan, G., Wan, Z., Trigo, I. F., & Sobrino, J. A. (2013). Satellite-derived land surface temperature: Current status and perspectives. *Remote Sensing of Environment*, *131*, 14–37. https://doi.org/10.1016/j.rse.2012.12.008

Lindén, J. (2011). Nocturnal cool island in the sahelian city of Ouagadougou, Burkina Faso. *International Journal of Climatology*, *31*(4), 605–620. https://doi.org/10.1002/joc.2069

Liu, L., & Zhang, Y. (2011). Urban heat island analysis using the Landsat TM data and ASTER data: A case study in Hong Kong. *Remote Sensing*, *3*(7), 1535–1552. https://doi.org/10.3390/rs3071535

Loosvelt, L., Peters, J., Skriver, H., Lievens, H., Van Coillie, F. M. B., De Baets, B., & Verhoest, N. E. C. (2012). Random forests as a tool for estimating uncertainty at pixel-level in SAR image classification. *International Journal of Applied Earth Observation and Geoinformation*, *19*(1), 173–184. https://doi.org/10.1016/j.jag.2012.05.011

Lukas, P., Melesse, A. M., & Kenea, T. T. (2023). Prediction of future land use/land cover changes using a coupled CA-ANN model in the upper Omo–Gibe river basin, Ethiopia. *Remote Sensing*, *15*(4). https://doi.org/10.3390/rs15041148

Mahmoud, M. I., Duker, A., Conrad, C., Thiel, M., & Ahmad, H. S. (2016). Analysis of settlement expansion and urban growth modelling using geoinformation for assessing potential impacts of urbanization on climate in Abuja city, Nigeria. *Remote Sensing*, *8*(3). https://doi.org/10.3390/rs8030220

Malamiri, H. R. G., Rousta, I., Olafsson, H., Zare, H., & Zhang, H. (2018). Gap-filling of MODIS time series Land surface temperature (LST) products using Singular spectrum analysis (SSA). *Atmosphere*, *9*(9). https://doi.org/10.3390/atmos9090334

Mas, J.-F., Pérez-Vega, A., Ghilardi, A., Martínez, S., Loya-Carrillo, J. O., & Vega, E.

(2014). A suite of tools for assessing thematic map accuracy. *Geography Journal*, *2014*, 1–10. https://doi.org/10.1155/2014/372349

McCarthy, M. P., Best, M. J., & Betts, R. A. (2010). Climate change in cities due to global warming and urban effects. *Geophysical Research Letters*, *37*(9), 1–5. https://doi.org/10.1029/2010GL042845

Mccartney, S., & Mehta, A. (2020). Satellite remote sensing for urban heat islands. *National Aeronautics and Space Administration Satellite Remote Sensing for Urban Heat Islands*.

Meyer, W. B., & Turner II, B. L. (1996). *Land-use/land-cover change: Challenges for geographers*.

Millogo, A. A., Yameogo, L., Kassié, D., Ouedraogo, F. D. C., Guissou, C., & Diabate, A. (2022). Spatial modelling of malaria prevalence associated with geographical factors in Houet province of Burkina. *GeoJournal*, *0123456789*. https://doi.org/10.1007/s10708-022-10692-7

Ministère de la santé. (2012). *Guide technique pour la surveillance intégrée de la maladie et la riposte au Burkina Faso*.

Mirzaei, M., Verrelst, J., Arbabi, M., Shaklabadi, Z., & Lotfizadeh, M. (2020). Urban heat island monitoring and impacts on citizen' s general health status in Isfahan metropolis : A remote sensing and field survey approach. *Remote Sensing*, *12*(8), 1–17.

Mitchell, B. C. (2011). Urbanization and land surface temperature in Pinellas county, Florida. *Udf*, 155.

Moulds, S., Buytaert, W., & Mijic, A. (2015). An open and extensible framework for spatially explicit land use change modelling: The LULC R package. *Geoscientific Model Development*, *8*(10), 3215–3229. https://doi.org/10.5194/gmd-8-3215-2015

Mungai, L. M., Messina, J. P., Zulu, L. C., Qi, J., & Snapp, S. (2022). Modeling spatiotemporal patterns of land use/land cover change in central Malawi using a neural network model. *Remote Sensing*, *14*(14). https://doi.org/10.3390/rs14143477

Mustafa, E. K., Co, Y., Liu, G., Kaloop, M. R., Beshr, A. A., Zarzoura, F., & Sadek, M. (2020). Study for predicting Land surface temperature (LST) using Landsat data: A comparison of four algorithms. *Advances in Civil Engineering*, *2020*. https://doi.org/10.1155/2020/7363546

Naboureh, A., Ebrahimy, H., Azadbakht, M., Bian, J., & Amani, M. (2020). RUESVMs: An ensemble method to handle the class imbalance problem in land cover mapping using google earth engine. *Remote Sensing*, *12*(21), 1–16. https://doi.org/10.3390/rs12213484

NASA. (2000). *Shuttle radar topography mission (SRTM)*. *0*, 1–4.

Ndossi, M. I., & Avdan, U. (2016). Inversion of Land surface temperature (LST) using Terra Aster data: A comparison of three algorithms. *Remote Sensing*, *8*(12). https://doi.org/10.3390/rs8120993

Nejad, M. T., Ghalehteimouri, K. J., Talkhabi, H., & Dolatshahi, Z. (2023). The relationship between atmospheric temperature inversion and urban air pollution characteristics: A case study of Tehran, Iran. *Discover Environment*, *1*(1). https://doi.org/10.1007/s44274-023-00018-w

Nery, T., Sadler, R., Solis-Aulestia, M., White, B., Polyakov, M., & Chalak, M. (2016). Comparing supervised algorithms in land use and land cover classification of a Landsat time-series. *International Geoscience and Remote Sensing Symposium (IGARSS)*, *2016-Novem*(July), 5165–5168. https://doi.org/10.1109/IGARSS.2016.7730346

Niya, A. K., Huang, J., Karimi, H., Keshtkar, H., & Naimi, B. (2019). Use of intensity analysis to characterize land use/cover change in the biggest island of Persian gulf, Qeshm island, Iran. *Sustainability (Switzerland)*, *11*(16). https://doi.org/10.3390/su11164396

NOAA. (2021). *NOAA daily Mauna Loa CO2*. NOAA.

Offerle, B., Jonsson, P., Eliasson, I., & Grimmond, C. S. B. (2005). Urban modification of the surface energy balance in the West African Sahel: Ouagadougou, Burkina Faso. *Journal of Climate*, *18*(19), 3983–3995. https://doi.org/10.1175/JCLI3520.1

Ogunjobi, K. O., Adamu, Y., Akinsanola, A. A., & Orimoloye, I. R. (2018). Spatio-temporal analysis of land use dynamics and its potential indications on land surface temperature in Sokoto metropolis, Nigeria. *Royal Society Open Science*, *5*(12). https://doi.org/10.1098/rsos.180661

Ouedraogo, V., Hackman, K. O., Thiel, M., & Dukiya, J. (2023). Intensity analysis for urban land use/land cover dynamics characterization of Ouagadougou and Bobo-Dioulasso in Burkina Faso. *Land*, *12*(5), 1063. https://doi.org/10.3390/land12051063

Ouellette, F. (2008). Reaching for equilibrium: An alternative view of the unbalanced carbon cycle. *Arxiv Preprint ArXiv:0802.3130*, 1–17. Retrieved from http://arxiv.org/pdf/0802.3130

Pal, S., & Ziaul, S. (2017). Detection of land use and land cover change and land surface temperature in English Bazar urban centre. *Egyptian Journal of Remote Sensing and Space Science*, *20*(1), 125–145. https://doi.org/10.1016/j.ejrs.2016.11.003

Parastatidis, D., Mitraka, Z., Chrysoulakis, N., & Abrams, M. (2017). Online global land surface temperature estimation from Landsat. *Remote Sensing*, *9*(12), 1–16. https://doi.org/10.3390/rs9121208

Patakamuri, S. K., & O'Brien, N. (2021). *Package 'modifiedmk'*. https://doi.org/10.1023/B

Patra, S., Sahoo, S., Mishra, P., & Mahapatra, S. C. (2018). Impacts of urbanization on land use /cover changes and its probable implications on local climate and groundwater level. *Journal of Urban Management*, *7*(2), 70–84. https://doi.org/10.1016/j.jum.2018.04.006

Peng, X., Wu, W., Zheng, Y., Sun, J., Hu, T., & Wang, P. (2020). Correlation analysis of land surface temperature and topographic elements in Hangzhou, China. *Scientific*

Reports, *10*(1), 1–16. https://doi.org/10.1038/s41598-020-67423-6

PNDES. (2016). *Infrastructures routières, de communication et d'habitat*.

Polykretis, C., Grillakis, M. G., & Alexakis, D. D. (2020). Exploring the impact of various spectral indices on land cover change detection using change vector analysis: A case study of Crete island, Greece. *Remote Sensing*, *12*(2). https://doi.org/10.3390/rs12020319

Pontius, R. G., Gao, Y., Giner, N. M., Kohyama, T., Osaki, M., & Hirose, K. (2013). Design and interpretation of intensity analysis illustrated by land change in central Kalimantan, Indonesia. *Land*, 351–369. https://doi.org/10.3390/land2030351

Porson, A., Clark, P. A., Harman, I. N., Best, M. J., & Belcher, S. E. (2010). Implementation of a new urban energy budget scheme in the MetUM. Part I: Description and idealized simulations. *Quarterly Journal of the Royal Meteorological Society*, *136*(651), 1514–1529. https://doi.org/https://doi.org/10.1002/qj.668

Powell, J. (2017). Scientists reach 100% consensus on anthropogenic global warming. *Bulletin of Science, Technology and Society*, *37*(4), 183–184. https://doi.org/10.1177/0270467619886266

Prakash, A. (2000). Thermal remote sensing: Concepts, issues and applications. ... *Archives of Photogrammetry and Remote Sensing*, *XXXIII*, 239–243. Retrievd from http://www.isprs.org/proceedings/XXXIII/congress/part1/239_XXXIII-part1.pdf

Prata, A. J., V. Casellescoll, C., Sobrino, J. A., & Ottle, C. (1995). Thermal remote sensing of land surface temperature from satellites: Current status and future prospects. *Remote Sensing Reviews*, *12*(3–4), 175–224. https://doi.org/10.1080/02757259509532285

Qiao, Z., Liu, L., Qin, Y., Xu, X., Wang, B., & Liu, Z. (2020). The impact of urban renewal on land surface temperature changes: A case study in the main city of Guangzhou, China. *Remote Sensing*, *12*(5), 1–15. https://doi.org/10.3390/rs12050794

Quan, B., Pontius, R. G., & Song, H. (2019). Intensity analysis to communicate land change during three time intervals in two regions of Quanzhou city, China. *GIScience and Remote Sensing*, *57*(1), 21–36. https://doi.org/10.1080/15481603.2019.1658420

Ramaiah, M., Avtar, R., & Rahman, M. M. (2020). Land cover influences on LST in two proposed smart cities of India: Comparative analysis using spectral indices. *Land*, *9*(9). https://doi.org/10.3390/LAND9090292

Rasul, A., Balzter, H., Ibrahim, G. R. F., Hameed, H. M., Wheeler, J., Adamu, B., Ibrahim, S., & Najmaddin, P. M. (2018). Applying built-up and bare-soil indices from Landsat 8 to cities in dry climates. *Land*, *7*(3). https://doi.org/10.3390/land7030081

Reese, H. (2011). Classification of Sweden' s forest and alpine vegetation using optical satellite and inventory data. In *Habitat*. retrieved from http://pub.epsilon.slu.se/8349/

Rimal, B., Zhang, L., Keshtkar, H., Haack, B. N., Rijal, S., & Zhang, P. (2018). Land use/land cover dynamics and modeling of urban land expansion by the integration of cellular automata and Markov Chain. *ISPRS International Journal of Geo-Information*, *7*(4). https://doi.org/10.3390/ijgi7040154

Rimal, B., Zhang, L., Keshtkar, H., Wang, N., & Lin, Y. (2017). Monitoring and modeling of spatiotemporal urban expansion and land-use/land-cover change using integrated Markov Chain cellular automata model. *ISPRS International Journal of Geo-Information*, *6*(9). https://doi.org/10.3390/ijgi6090288

Sakieh, Y., Amiri, B. J., Danekar, A., Feghhi, J., & Dezhkam, S. (2015). Simulating urban expansion and scenario prediction using a cellular automata urban growth model, SLEUTH, through a case study of Karaj city, Iran. *Journal of Housing and the Built Environment*, *30*(4), 591–611. https://doi.org/10.1007/s10901-014-9432-3

Sannigrahi, S., Bhatt, S., Rahmat, S., Uniyal, B., Banerjee, S., Chakraborti, S., Jha, S., Lahiri, S., Santra, K., & Bhatt, A. (2017). Analyzing the role of biophysical compositions in minimizing urban land surface temperature and urban heating. *Urban Climate*, *24*(July), 803–819. https://doi.org/10.1016/j.uclim.2017.10.002

Schmittner, A. (2018). *Introduction to climate science*. 239.

Schober, P., & Schwarte, L. A. (2018). Correlation coefficients: Appropriate use and interpretation. *Anesthesia and Analgesia*, *126*(5), 1763–1768. https://doi.org/10.1213/ANE.0000000000002864

Schug, F., Okujeni, A., Hauer, J., Hostert, P., Nielsen, J., & van der Linden, S. (2018). Mapping patterns of urban development in Ouagadougou, Burkina Faso, using machine learning regression modeling with bi-seasonal Landsat time series. *Remote Sensing of Environment*, *210*(June), 217–228. https://doi.org/10.1016/j.rse.2018.03.022

Sekertekin, A., & Bonafoni, S. (2020). Land surface temperature retrieval from Landsat 5, 7, and 8 over rural areas: Assessment of different retrieval algorithms and emissivity models and toolbox implementation. *Remote Sensing*, *12*(2). https://doi.org/10.3390/rs12020294

Sekertekin, A., & Zadbagher, E. (2021). Simulation of future land surface temperature distribution and evaluating surface urban heat island based on impervious surface area. *Ecological Indicators*, *122*(May 2019), 107230. https://doi.org/10.1016/j.ecolind.2020.107230

Selin, H., & Mann, M. E. (2021). Global warming. In *Britannica* (p. 54). Encyclopaedia Britannica, Inc.

Shi, Y., Liu, S., Yan, W., Zhao, S., Ning, Y., Peng, X., Chen, W., Chen, L., Hu, X., Fu, B., Kennedy, R., Lv, Y., Liao, J., Peng, C., Rosa, I. M. D., Roy, D., Shen, S., Smith, A., Wang, C., … Zhu, Y. (2021). Influence of landscape features on urban land surface temperature: Scale and neighborhood effects. *Science of the Total Environment*, *771*, 145381. https://doi.org/10.1016/j.scitotenv.2021.145381

Shiff, S., Helman, D., & Lensky, I. M. (2021). Worldwide continuous gap-filled MODIS land surface temperature dataset. *Scientific Data*, *8*(1), 1–10.

https://doi.org/10.1038/s41597-021-00861-7

Sibanda, S., & Ahmed, F. (2020). Modelling historic and future land use/land cover changes and their impact on wetland area in Shashe sub-catchment, Zimbabwe. *Modeling Earth Systems and Environment*, *7*(1), 57–70. https://doi.org/10.1007/s40808-020-00963-y

Simwanda, M., Ranagalage, M., Estoque, R. C., & Murayama, Y. (2019). Spatial analysis of surface urban heat islands in four rapidly growing african cities. *Remote Sensing*, *11*(14), 1–20. https://doi.org/10.3390/rs11141645

Singh, P., Kikon, N., & Verma, P. (2017). Impact of land use change and urbanization on urban heat island in Lucknow city, central India. A remote sensing based estimate. *Sustainable Cities and Society*, *32*, 100–114. https://doi.org/10.1016/j.scs.2017.02.018

Singh, R., & Prasad, P. R. C. (2015). Interpolation of data gaps of SLC-off Landsat ETM+ images using algorithm based on the differential operators. *JACSM*, *6*(2), 93–100.

Soesbergen, A. van. (2016). *A review of land- use change models*.

Soma, A. (2015). *Vulnérabilité et résilience urbaines: Perception et gestion territoriale des risques d'inondation dans la ville de Ouagadougou*. PhD thesis, Université Joseph Ki-Zerbo, Ouagadougou, Burkina Faso

Son, J., Jung, I., Park, K., & Han, B. (2015). Tracking-by-segmentation with online gradient boosting decision tree. *Proceedings of the IEEE International Conference on Computer Vision*, *2015 Inter*, 3056–3064. https://doi.org/10.1109/ICCV.2015.350

Sory, I. (2013). *« OUAGA LA BELLE ! » Gestion des déchets solides à Ouagadougou : Enjeux politiques, jeux d'acteurs et inégalités environnementales*.

Sory, I. (2019). *Public land policies at an impasse in Ouagadougou (Burkina Faso)*. *269*(1).

Sparkes, G., Kerr, A., Rafuse, H., Sparkes, G., Hinchey, J., & Sandeman, H. (2011). Geology of the Bonavista Peninsula view project labrador Visible/infrared spectroscopy (VIRS) as a research tool in economic geology: Background and pilot studies from new found land and labrador. *Current Research*, *March*, 145–166. Retrieved from https://www.researchgate.net/publication/288899855

Stallinga, P., & Khmelinskii, I. (2016). The perception of anthropogenic global warming modeled by game theory decision tables. *European Scientific Journal, ESJ*, *12*(29), 427. https://doi.org/10.19044/esj.2016.v12n29p427

Stemn, E., & Kumi-Boateng, B. (2020). Modelling of land surface temperature changes as determinant of urban heat island and risk of heat-related conditions in the Wassa west mining area of Ghana. *Modeling Earth Systems and Environment*, *6*(3), 1727–1740. https://doi.org/10.1007/s40808-020-00786-x

Stroppiana, D., Antoninetti, M., & Brivio, P. A. (2014). Seasonality of MODIS LST over southern Italy and correlation with land cover, topography and solar radiation. *European Journal of Remote Sensing*, *47*(1), 133–152.

https://doi.org/10.5721/EuJRS20144709

Tafesse, B., & Suryabhagavan, K. V. (2019). Systematic modeling of impacts of land-use and land-cover changes on land surface temperature in Adama Zuria district, Ethiopia. *Modeling Earth Systems and Environment*, *5*(3), 805–817. https://doi.org/10.1007/s40808-018-0567-1

Tariq, A., & Shu, H. (2020). CA-Markov Chain analysis of seasonal land surface temperature and land use land cover change using optical multi-temporal satellite data of Faisalabad, Pakistan. *Remote Sensing*, *12*(20), 1–23. https://doi.org/10.3390/rs12203402

Tassi, A., & Vizzari, M. (2020). Object-oriented LULC classification in Google earth engine combining SNIC, GLCM, and machine learning algorithms. *Remote Sensing*, *12*(22), 1–17. https://doi.org/10.3390/rs12223776

Tempfli, K., Kerle, N., Huurneman, G. C., Janssen, L. L. F., Bakker, W. H., Feringa, W., Gieske, A. S. M., Gorte, B. G. H., Grabmaier, K. A., Hecker, C. A., Horn, J. A., Huurneman, G. C., Janssen, L. L. F., Kerle, N., Meer, F. D. Van Der, Parodi, G. N., Pohl, C., Reeves, C. V, Ruitenbeek, F. J. Van, … Woldai, T. (2009). Principles of remote sensing. In K. Tempfli, N. Kerle, G. C. Huurneman, & L. L. F. Janssen (Eds.), *The International Institute for Geo-Information Science and Earth Observation (ITC)* (Fourth edi). The International Institute for Geo-Information Science and Earth Observation (ITC).

Turok, I., & McGranahan, G. (2013). Urbanization and economic growth: The arguments and evidence for Africa and Asia. *Environment and Urbanization*, *25*(2), 465–482. https://doi.org/10.1177/0956247813490908

United Nations. (2018). World urbanization prospects. In *Demographic Research* (Vol. 12). Retrieved from https://population.un.org/wup/Publications/Files/WUP2018-Report.pdf

United Nations. (2019). World population prospects 2019. In *Department of Economic and Social Affairs, Population Division* (Issue 141). Retrieved from https://www.un.org/development/desa/pd/news/world-population-prospects-2019-0

USGS. (2004). *SLC-off gap-filled products, gap-Fill algorithm methodology background*.

USGS. (2019). Landsat 8 data users handbook. *Nasa*, *8* (November), 114. Retrieved from https://landsat.usgs.gov/documents/Landsat8DataUsersHandbook.pdf

USGS. (2020). *Landsat collection 1 vs. Collection 2 Summary*. .

Wan, Z., Zhang, Y., Zhang, Q., & Li, Z. L. (2004). Quality assessment and validation of the MODIS global land surface temperature. *International Journal of Remote Sensing*, *25*(1), 261–274. https://doi.org/10.1080/0143116031000116417

White-newsome, J. L., Brines, S. J., Brown, D. G., Dvonch, J. T., Gronlund, C. J., Zhang, K., Oswald, E. M., & Neill, M. S. O. (2013). Validating satellite-derived land surface temperature with in situ measurements : A public health perspective. *Environmental Health Perspectives*, *121*(8), 925–931. https://doi.org/https://doi.org/10.1289/ehp.1206176

World Bank. (2002). *Burkina Faso: Upgrading of low-income settlements. Country assessment report*.

Xia, L., Mitra, C., Dong, L., & Yang, Q. (2017). Understanding land use change impacts on microclimate using Weather research and forecasting (WRF) model. *Physics and Chemistry of the Earth*, *103*, 115–126. https://doi.org/10.1016/j.pce.2017.01.017

Xiong, X., Che, N., Barnes, W., Xie, Y., Wang, L., & Qu, J. (2006). Status of Aqua MODIS spatial characterization and performance. *Sensors, Systems, and Next-Generation Satellites X*, *6361*, 63610T. https://doi.org/10.1117/12.687162

Xu, L. Y., Xie, X. D., & Li, S. (2013). Correlation analysis of the urban heat island effect and the spatial and temporal distribution of atmospheric particulates using TM images in Beijing. *Environmental Pollution*, *178*, 102–114. https://doi.org/10.1016/j.envpol.2013.03.006

Yadav, R., Tripathi, S. K., Pranuthi, G., & Dubey, S. K. (2014). Trend analysis by Mann-Kendall test for precipitation and temperature for thirteen districts of Uttarakhand. *Journal of Agrometeorology*, *16*(2), 164–171. https://doi.org/10.54386/jam.v16i2.1507

Yan, Y., Mao, K., Shi, J., Piao, S., Shen, X., Dozier, J., Liu, Y., Ren, H. li, & Bao, Q. (2020). Driving forces of land surface temperature anomalous changes in north America in 2002–2018. *Scientific Reports*, *10*(1), 1–13. https://doi.org/10.1038/s41598-020-63701-5

Yangouliba, G. I., Zoungrana, B. J. B., Hackman, K. O., Koch, H., Liersch, S., Sintondji, L. O., Dipama, J. M., Kwawuvi, D., Ouedraogo, V., Yabré, S., Bonkoungou, B., Sougué, M., Gadiaga, A., & Koffi, B. (2022). Modelling past and future land use and land cover dynamics in the Nakambe river basin, West Africa. *Modeling Earth Systems and Environment*, *0123456789*. doi.org/10.1007/s40808-022-01569-2

Yin, G., Mariethoz, G., & McCabe, M. F. (2017). Gap-filling of Landsat 7 imagery using the direct sampling method. *Remote Sensing*, *9*(1), 1–20. https://doi.org/10.3390/rs9010012

Yuen, B., & Kumssa, A. (2011). *Climate change and sustainable urban development. In Africa and Asia Editors*. https://doi.org/10.1007/978-90-481-9867-2

Zhang, W., Li, Y., Li, Z., Wei, X., Ren, T., Liu, J., & Zhu, Y. (2020). *Impacts of climate change , population growth , and urbanization on future population exposure to long-term temperature change during the warm season in China*.

Zoungrana, B. J., Conrad, C., Amekudzi, L. K., Thiel, M., & Da, E. D. (2014). *Land use/cover response to rainfall variability: A comparing analysis between NDVI and EVI in the southwest of Burkina Faso*. 63–77. https://doi.org/10.3390/cli3010063

Zoungrana, B. J., Conrad, C., Amekudzi, L., Thiel, M., Da, E., Forkuor, G., & Löw, F. (2015). Multi-temporal Landsat images and ancillary data for Land use/cover change (LULCC) detection in the southwest of Burkina Faso, West Africa. *Remote Sensing*, *7*(9), 12076–12102. https://doi.org/10.3390/rs70912076

APPENDICES

APPENDIX A: LULC intensity analysis / Category level metrics in Ouagadougou

	Gross Loss	**Gross Gain**	**Loss Intensity**	**Gain Intensity**	**Uniform Category Intensity**	**Loss Behaviour**	**Gain Behaviour**
Category level Intensity Analysis for interval: 2003 - 2009							
Built-up	9813.667	15551.833	0.028	0.040	0.026	Active	Active
Agricultural land	17324.333	9087.667	0.025	0.014	0.026	Dormant	Dormant
Forest	672.833	413.333	0.077	0.058	0.026	Active	Active
Bare land	383.333	2761.000	0.091	0.149	0.026	Active	Active
Water	363.667	744.000	0.056	0.085	0.026	Active	Active
Category level Intensity Analysis for interval: 2009 - 2015							
Built-up	4960.500	24568.667	0.013	0.049	0.030	Dormant	Active
Agricultural land	24489.333	5217.833	0.037	0.010	0.030	Active	Dormant
Forest	322.167	1319.333	0.045	0.100	0.030	Active	Active
Bare land	2182.333	858.000	0.118	0.081	0.030	Active	Active
Water	473.167	463.667	0.054	0.053	0.030	Active	Active
Category level Intensity Analysis for interval: 2015 - 2021							
Built-up	7627.833	28252.833	0.015	0.045	0.036	Dormant	Active
Agricultural land	28586.000	6423.833	0.053	0.016	0.036	Active	Dormant
Forest	1092.000	1162.167	0.083	0.086	0.036	Active	Active
Bare land	1156.167	2963.333	0.110	0.139	0.036	Active	Active
Water	421.833	81.667	0.049	0.012	0.036	Active	Dormant

APPENDIX B: LULC intensity analysis / Category level metrics in Bobo-Dioulasso

	Gross Loss	**Gross Gain**	**Loss Intensity**	**Gain Intensity**	**Uniform Category Intensity**	**Loss Behaviour**	**Gain Behaviour**
Category level Intensity Analysis for interval: 2003 - 2009							
Built-up	1019.667	4618.000	0.013	0.045	0.022	Dormant	Active
Agricultural land	20813.333	21650.000	0.013	0.014	0.022	Dormant	Dormant
Forest	20545.000	16155.667	0.067	0.057	0.022	Active	Active
Bare land	252.167	206.000	0.117	0.110	0.022	Active	Active
Water	0.000	0.500	0.000	0.000	0.022	Dormant	Dormant
Category level Intensity Analysis for interval: 2009 - 2015							
Built-up	1470.333	5340.167	0.014	0.042	0.022	Dormant	Active
Agricultural land	13042.500	29981.333	0.008	0.018	0.022	Dormant	Dormant
Forest	27153.000	8278.000	0.097	0.049	0.022	Active	Active
Bare land	204.333	118.500	0.109	0.087	0.022	Active	Active
Water	1939.833	92.000	0.158	0.080	0.022	Active	Active
Category level Intensity Analysis for interval: 2015 - 2021							
Built-up	930.500	12441.167	0.007	0.064	0.022	Dormant	Active
Agricultural land	28049.500	13891.000	0.017	0.009	0.022	Dormant	Dormant
Forest	13000.833	15238.167	0.077	0.084	0.022	Active	Active
Bare land	25.667	436.167	0.019	0.114	0.022	Dormant	Active
Water	0.000	0.000	0.000	0.000	0.022	Dormant	Dormant